PRECISION NEUTRON FLUX MEASUREMENT AND ADVANCEMENT USING THE ALPHA GAMMA TECHNIQUE

Eamon S. Anderson

Submitted to the faculty of the University Graduate School

in partial fulfillment of the requirements

for the degree

Doctor of Philosophy

in the Department of Physics,

Indiana University

August, 2017

Accepted by the Graduate Faculty, Indiana University, in partial fulfillment of the requirements for the degree of Doctor of Philosophy.

Doctoral Committee

W. Michael Snow, PhD

Chen-Yu Liu, PhD

Adam P. Szczepaniak, PhD

Micheal S. Berger, PhD

M. Scott Dewey, PhD

August 7^{th}, 2017

Acknowledgments

Like all stories of any merit, how it begins and ends is hardly as interesting and compelling as how we got there. And though this is curtain call on just a part of my own, I'm glad to have this chance for all the wonderful performers to take a bow. I couldn't have done this without you. To everyone who helped me in any way, thank you.

I'd like to begin by thanking my advisor, Dr. W. Mike Snow. His unflinching dedication to scientific inquiry, his entertainment of some of my most hare-brained ideas, and the assertion, in the event that they fail spectacularly, that we can't graduate unless we break a sufficient amount of equipment was and will continue to be some of my best armor against my own insecurity. I always felt like a colleague during our discussions, and never like a subordinate. I never felt like I had a 'boss' that I had to placate. He paid me anyway, which is great because I still have to eat.

Thank you to my whole defense committee. Dr. Chen-Yu Liu, Dr. M. Scott Dewey, Dr. Adam P. Szczepaniak, and Dr. Micheal S. Berger. Dr. Chen-Yu Liu and the UCNτ experiment, though I did not participate in the research, was what first got me interested in the neutron lifetime. She also taught me subatomic particle physics, or put another way, how to do my research. Dr. M. Scott Dewey has been my friend and colleague since I began research at NIST. He participated in many of the 'archaeological' investigations associated with working on an experiment that's almost 40 years old, which kept me both productive and, to some measure, sane. Special thanks to Dr. Adam Szczepaniak and Dr. Micheal Berger, who joined my committee when it was suddenly time for me to make a hasty exit.

And thanks to both Dr. Alan Kostelecky and Dr. Hermann Nann, who, for various reasons, could no longer participate in full.

Doing research within the NIST scientific community is a gift. To all the staff with whom I had the pleasure to interact, thank you. Dr. Jeff Nico with whom I shared both scientific discourse and gardening tips (not to mention a special dislike of squirrels). Dr. David Gilliam, who, along with Dr. Dewey, collaborated on the NBS-1 recalibration experiment (and handled the worst of it). Dr. Pieter Mumm, for taking up the Alpha-Gamma experiment as I leave. Dr. Daniel Hussey, who showed me how neutron scattering is much more interesting than I had given it credit for. Thanks to Eli Baltic and Rob Shankle, who managed to parse the lousy shop drawings I so frequently sent and create what I needed, even when it wasn't what I had thought I wanted. Dr. Mike Huber, who fully supported my ancillary pursuit: home-brewed beer. And to everyone else who in countless ways made this work possible: Dr. David Jacobson, Dr. Alan Thompson, Dr. Shannon F. Hoogerheide, Dr. Dmitry Pushin, and too many others.

Dr. Andrew Yue taught me most of what I know about our experiment. I can attribute all the progress I've made to him in one way or another. I know this would have been orders of magnitude more challenging without his guidance. For him as much as for myself, I hope that I've made something that will last.

The Indiana University physics staff are invaluable to the program. I would like to thank Walt Fox for teaching me how to use CAD software to design parts. Philip Childress for teaching me how to design the parts I actually want, and Gary Wood for teaching me how to make those parts. Thanks also to John Vanderwerp for the constant tutelage on the minutiae of experiment operation.

To my friends in the Indiana University graduate physics program. To everyone, most of all Dr. Daniel Salvat and (soon to be) Dr. Evan Weisman despite, or most likely in

part because of, the strange humours that late-night physics assignments so often evoke. To Caito Scherr, Andrew Fair, Brian Wermcrantz, Matthew Montemore, and Jillian Goetz from Grinnell College. Though many miles have separated us for so long since college, I still feel just as close. To my friends from high school, who continue to be dear, and who have always felt the same for me throughout our occasionally complicated friendships: Garrett Rabinak, John Gibson, Jose Dieck, Ian Reid, Brian Falbo, Matt Cherry, Jake Chen, Jason Miller, Uday Pisipati, and Anran Wang. Thank you to my high school physics teacher Mike Kennedy. His passion for the field and, perhaps more importantly, primary education, will do more for physics than nearly anything else.

My parents have always had my best interest in mind, even if it didn't feel like it at the time. They've always been dedicated to my success. To my siblings who rarely care for me implicitly. To the rest of my family, especially Uncle Bob who supported my education both emotionally and financially.

Brandi Emerick, Heather Kramer, and Jack Salt Moon. You each carry my whole heart.

Eamon S. Anderson

PRECISION NEUTRON FLUX MEASUREMENT AND ADVANCEMENT USING THE ALPHA GAMMA TECHNIQUE

Absolute neutron flux detection is important for many scientific applications and critical for the measurement of the free neutron lifetime in a beam of cold neutrons [1]. The neutron lifetime is a critical input for Big Bang nucleosynthesis and tests of unitarity of the Cabbibo-Kobayashi-Maskawa (CKM) matrix [2, 3] as well as the measurement of standard neutron cross sections and branching ratios of neutron interactions for a variety of isotopes.

This thesis discusses the results of a new method to measure neutron flux called the Alpha-Gamma (AG) technique. A transfer calibration technique allows the detection efficiency of a pair of HPGe gamma detectors to be coupled to the measured absolute decay rate of a ^{239}Pu source. A thick ^{10}B target is then used to measure the absolute flux of neutrons in the beam. Using this technique we show that it is possible to determine the detection efficiency of the Flux Monitor (FM) used in the in-beam neutron lifetime experiment to an absolute accuracy of better than 0.1%. We present the results and systematic error analysis for the calibration of the neutron monitors now in use in the new neutron lifetime measurement at the National Institute of Standards and Technology (NIST) Center for Neutron Research (NCNR) [4].

Contents

Glossary

AFM Atomic Force Microscopy. 118

AG Alpha-Gamma - Either the transfer calibration technique, or the apparatus used to measure absolute flux consisting of a pair of HPGe gamma detectors and an alpha detector. vii

BBN Big Bang nucleosynthesis. 1, 9–11

CEEM Center for the Exploration of Energy and Matter - an Indiana University research institution with a dedicated low-energy neutron source. 118

CF ConFlat - a type of vacuum flange which uses a "knife edge" and a copper gasket to make a seal. 49, 70, 75

CKM Cabbibo-Kobayashi-Maskawa Matrix - A unitary matrix describing quark mixing. 7

FM Flux Monitor. vii, 48, 50

HPGe HPGe detector - a solid state gamma detector. 19, 20, 22–25, 47, 48, 59, 63–65, 77–79, 81, 88, 94, 106–109, 111, 124, 125

IDA Isotope Dilution Analysis - The isotope dilution step of IDMS, and a term used interchangeably with IDMS in some of the literature due to the frequency with which IDA is employed using a mass spectrometer. 34

IDMS Isotope Dilution Mass Spectrometry - A process by which a well-measured quantity of different isotopic composition is added to an unknown sample in order to determine the precise isotopic composition of the sample. 31, 33, 34, 36–38, 40, 41, 130

IRMM Institute for Reference Materials and Measurements. 30, 117, 119

LENS Low Energy Neutron Source - a pulsed neutron source produced by a 13 MeV proton beam incident upon a beryllium target. 118

NCNR NIST Center for Neutron Research. 12, 18, 28, 51, 52, 82, 111, 125, 130, 133

NIST National Institute of Standards and Technology. vii, 2, 4, 12, 16, 18, 28, 34, 36, 39, 42, 48, 82, 86, 110, 124, 131

PIPS passivated implanted planar silicon - Canberra trade name for a doped silicon diode charged particle detector. 59, 60, 63, 68

RFO Research Facility Operations. 28

SANS Small Angle Neutron Scattering. 52, 118

SCA Single channel analyzer. 96

SEM Scanning Electron Microscopy. 118

SRM standard reference material - a well characterized quantity of material maintained by one of several standards laboratories around the world. 36–39

Chapter 1

The Neutron Lifetime

Neutron beta decay is the simplest weak decay of a system of three quarks. The slight excess of mass energy of the neutron (quark composition udd) relative to that of the decay products (939.565 MeV for the neutron, and 938.272 MeV + 0.510998 MeV for the proton (quark composition uud) and electron respectively, with a negligible neutrino mass) means that the neutron can decay into a proton, electron, and electron antineutrino releasing $\Delta_E = 0.782$ MeV of energy in the process. This proceeds by the emission of a W^- boson from one of the d quarks in the neutron. This decay transforms the d quark into a u quark, and the W^- subsequently decays into an electron and an electron antineutrino. Since no other possible decays are known to exist due to lepton and baryon number conservation, the free neutron has a relatively long lifetime of $\tau_{\rm n} \simeq 880$ seconds. This reflects both the small amplitude for electroweak processes and the small phase space available to this particular decay. Neutrons bound within nuclei can be stable against β decays due to the combined effects of the Pauli exclusion principle and the conservation laws.

Measurement of the neutron lifetime is important for astrophysics, cosmology and Big Bang nucleosynthesis (BBN), elementary particle physics, violations of fundamental symmetries, and other Standard Model physics issues [5] [6]. The neutron lifetime has been measured using two qualitatively different techniques: storage of ultracold neutrons using material [7] [8] and magnetic traps [9] [10] [11], and in-beam neutron decays, with the sole

high precision result at the moment coming from the NIST in-beam neutron lifetime experiment using a Penning trap [1] [4]. Despite many measurements, the values of τ_n used in the Particle Data Group (PDG) best average [12] suffer from a spread that is much larger than expected based on statistics. The immediate conclusion is that at least some of the reported results have additional sources of systematic errors.

The neutron beam and bottle lifetime experiments were in agreement before 2005. A new result reported by Serebrov et al in 2005 [7] was 7 σ below the previous world average and produced a disturbing amount of turmoil over the next decade. An analysis by Pichlmaier a few years later [8] on a decade-old experiment agreed with the 2005 result by Serebrov, and later reanalyses of two earlier results (one from the 1989 Mampe data by Steyerl [13] and another of the 2000 Arzumanov result [14]) retroactively changed their final reported values and found themselves in agreement with the new lower value. These analyses considered new sources of systematic errors and new physics models of the ultracold neutron interactions on the Fomblin-coated surface of the trap walls which were used in all of these experiments. The result by Nesvizhevskii was completely retracted [15]. The current PDG average neutron lifetime, noting the disagreement between the two methods, is 880 ± 1.0 s.

This disturbing sequence of events clearly demonstrated that systematic errors had been seriously underestimated in many past neutron lifetime measurements using material traps and strongly motivated other groups to pursue independent measurements using different techniques. Very recently a new result using magnetically-trapped ultracold neutrons has appeared which also agrees with the cluster of material bottle measurements around 877 seconds [16]. All of these new results for the neutron lifetime come from measurements using ultracold neutrons.

A different value for the neutron lifetime values comes from an in-beam method using a Penning trap to trap and count decay protons along with simultaneous measurement of

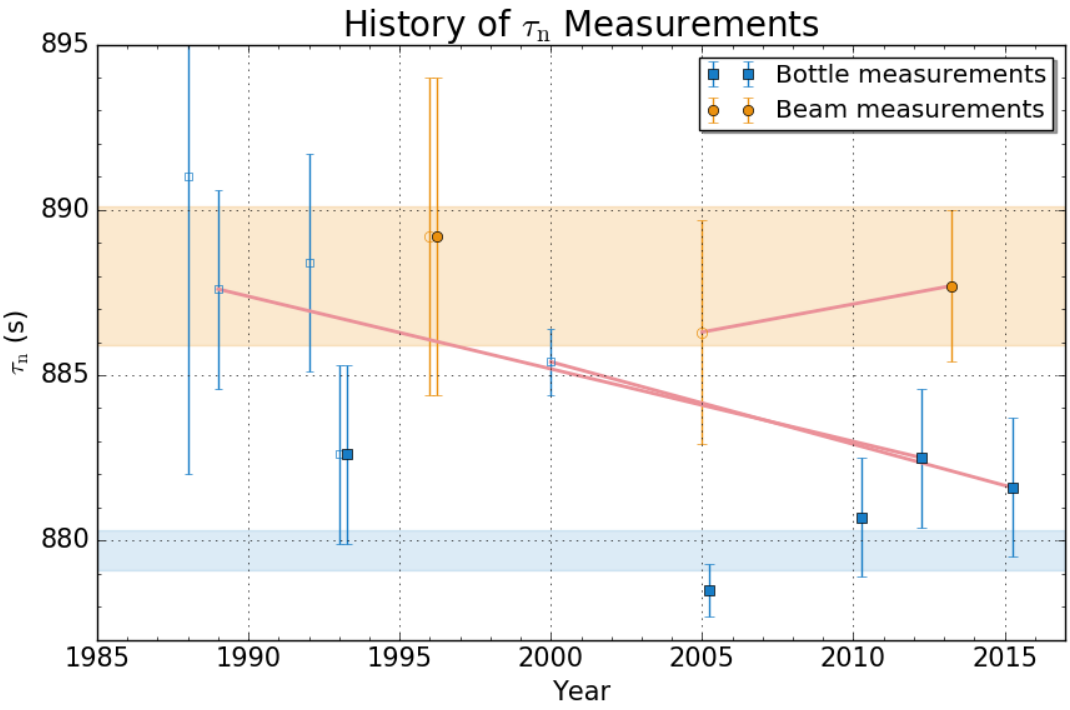

Figure 1.1: A plot of the results and stated errors for several neutron lifetime measurements conducted since 1985. The two in-beam measurements used in the PDG average, are shown in orange. The data currently contributing to the PDG average are shown as the filled-in shapes. The red line shows the trajectory of reanalyses (in the case of the bottle experiments), or further measurements (the in-beam experiment) which changed previously reported results. The shaded regions show the in-beam (orange) and bottle (blue) individual neutron lifetime averages. A slight offset in year is applied to show the data sets that have remained unchanged but are still used.

the neutron density in the trap. Resolution of this discrepancy requires the measurement of the in-beam neutron lifetime to higher precision. The most significant source of error in the 2005 in-beam neutron lifetime result came from the Flux Monitor (FM) used to measure the absolute flux of neutrons. For several years the systematic error on this measurement set a fundamental limit to the possible accuracy for the neutron lifetime using this technique. A long-term project to improve the accuracy of absolute neutron flux using an Alpha-Gamma technique described in this thesis achieved a breakthrough in the improvement of the measurement accuracy a few years ago by a factor of 5 [4]. This improvement was applied retroactively to the 2005 Penning trap neutron lifetime experiment to enable the group to report a revised value for τ_{n} in 2013 with a slightly smaller uncertainty. This revision made essentially no change in the central value, but the breakthrough in absolute neutron flux measurement was great enough to justify a remeasurement of the neutron lifetime using this technique with the original apparatus. With the 2013 improvements to the neutron flux determination via measurement of the absolute efficiency of the flux monitor ϵ_0, counting statistics remained as the most significant source of uncertainty.

A new in-beam neutron lifetime experiment is currently taking data at the National Institute of Standards and Technology (NIST) Center for Neutron Research (NCNR). In order to achieve $< 0.1\%$ uncertainty, the measurement of the efficiency of the flux monitor must be further improved, and its experimental procedures refined. This thesis will discuss the current status and the progress to date toward this goal. In particular, we will report the absolute efficiencies for the neutron flux monitors now in use in the new ongoing Penning trap experiment at NIST that we have measured and quantified the systematic errors for. The accuracy of this method of measuring the free neutron lifetime can be further improved in the future based on our experience with this new neutron flux measurement method using the Alpha-Gamma technique.

1.1 Neutron Beta Decay

In the Standard Model of Physics, nuclear beta decay proceeds via the electroweak interaction. The interaction was first introduced as a four-fermion vector interaction [17]. Gamow and Teller extended Fermi's Hamiltonian to include all Lorentz-invariant forms: scalar (S), pseudoscalar (P), tensor(T), vector(V), and axial vector(A) interactions [18]. The P terms are highly suppressed in non-relativistic decays such as neutron beta decay. Under the assumption that the weak interaction violates parity maximally, the allowed interactions correspond to those which do not carry orbital angular momentum in the final state of the leptons. This means that S, V type interactions produce leptons in a singlet state $\Delta J = 0$ (Fermi selection rule), and T, A produce leptons in a triplet state $\Delta J = 0, \pm 1$ (Gamow-Teller selection rule), where $\Delta J = J_i - J_f$, and J_i, J_f are the spin of the initial and final state respectively. Gamow-Teller interactions may not follow transitions which have $J_i = J_f = 0$. Both Fermi and Gamow-Teller cases have been observed, but there has been no evidence of S or T interactions. Since the energy released through nuclear beta decay is so low as compared to the mass of the Standard Model boson W^-, the quark-level details are not important to this discussion of beta decay. The Hamiltonian is then expressed using the Fermi-Gamow-Teller formulation as:

$$\mathcal{M} = \left[G_V \bar{p}\gamma_\mu n - G_A \bar{p}\gamma_5\gamma_\mu n\right]\left[\bar{e}\gamma_\mu\left(1-\gamma_5\right)\nu\right] \tag{1.1}$$

where $\bar{p}, n, \bar{e}$ and ν are the spinors for the proton, neutron, electron, and antineutrino. At the quark level, the coupling strength of G_A and G_V are equal, but strong interaction effects within the nucleon can alter the observed strength. By conservation of the vector current, G_V is unchanged. With no such mechanism for G_A, coupling coefficients are introduced

which permit these terms to differ:

$$\begin{aligned} G_V &= G_F V_{ud} C_V \\ G_A &= G_F V_{ud} C_A \end{aligned} \tag{1.2}$$

where $G_F = 1.1663787(6) \times 10^{-5}$ GeV^{-2} is the Fermi weak coupling constant, and C_V, C_A are the constants introduced in the weak Hamiltonian described by Jackson, Trieman, and Wyld [19]. The neutron lifetime τ_{n} is the inverse of the neutron decay probability per unit time, which is calculated from the Hamiltonian:

$$dW = (2\pi)^{-5}\, \delta\left(E_e + E_\nu - \Delta\right) \frac{1}{2E_e} \frac{1}{2E_\nu} d^3\mathbf{p}_e d^3\mathbf{p}_\nu \left|\mathcal{M}\right|^2 \tag{1.3}$$

where $E_e, E_\nu, \mathbf{p}_e, \mathbf{p}_\nu$ are the electron and antineutrino total energy and momentum, and $\Delta = 1.29333205(48)$ MeV is the neutron-proton mass difference. Integrate over the antineutrino momentum and electron solid angle to get an expression for the beta energy spectrum from neutron decay:

$$\frac{dW}{dE_e} = \frac{G_V^2 + 3G_A^2}{2\pi^3} E_e \left|\mathbf{p}_e\right| \left(\Delta - E_e\right)^2 \tag{1.4}$$

Integrating over the electron energy yields:

$$W = \frac{G_V^2 + 3G_A^2}{2\pi^3} f_R \tag{1.5}$$

where f_R is the value of the integral over the Fermi energy spectrum including corrections for Coulomb interactions, recoil order, and radiative corrections. W being the exponential decay constant, the lifetime is then the inverse of W:

$$\tau_{\mathrm{n}} = \frac{2\pi^3}{\left(G_V^2 + 3G_A^2\right) f_R} \tag{1.6}$$

Therefore measurement of the neutron lifetime constitutes measurement of the weak coupling constants G_V and G_A.

1.1.1 CKM Unitarity

The CKM matrix describes the mixing between the quark mass eigenstates via the weak eigenstates [2,20]. The CKM matrix is required to be unitary as it corresponds to a quantum mechanical change of basis states; otherwise there must be some form of extra dynamics. The top row is given as:

$$|V_u|^2 \equiv |V_{ud}|^2 + |V_{us}|^2 + |V_{ub}|^2 = 1 + \Delta_{CKM} \tag{1.7}$$

where Δ_{CKM} should be exactly 0. $|V_{ud}|^2$ constitutes the majority of the sum and is therefore of great importance for testing unitarity. The most precise measurements of $|V_{ud}|^2$ come from superallowed $0^+ \rightarrow 0^+$ decays, which are purely vector weak decays due to the initial and final angular momentum state ($J_i = J_f = 0$) [21]. This proceeds from a calculation of $\mathcal{F}t$ values, which are computed from the half-life of measured superallowed $0^+ \rightarrow 0^+$ decays (t) and a parameter f that depends on the decay energy and dynamics of each individual decay:

$$\mathcal{F}t \equiv ft\left(1+\delta_R\prime\right)\left(1+\delta_{NS}-\delta_C\right) = \frac{K}{2G_V^2\left(1+\Delta_R^V\right)} \tag{1.8}$$

where $K = 8120.2276(9) \times 10^{-10}\text{GeV}^{-4}$, G_V is the coupling constant for semileptonic weak interactions (such as neutron beta decay), and $\Delta_R^V, \delta_R\prime, \delta_{NS}$, and δ_C are for radiative corrections and the isospin-symmetry-breaking correction. $|V_{ud}|$ is calculated from Eqn. (1.2), and with measured values of G_F we get:

$$|V_{ud}|^2 = \frac{K}{2G_F^2\left(1+\Delta_R^V\right)\bar{\mathcal{F}}t} = \frac{2915.64 \pm 1.08}{\bar{\mathcal{F}}t} \tag{1.9}$$

where $\bar{\mathcal{F}}t$ is the average of all measured values of $\mathcal{F}t$ [21]. From this, $|V_{ud}| = 0.97417(21)$.

The neutron lifetime $\tau_{\rm n}$ can also be used to calculate the matrix element $|V_{ud}|$ via the quark-level description of the beta decay matrix element in Eqn. (1.1) [22] to be:

$$\tau_{\rm n} = \frac{4908.7 \pm 1.9{\rm s}}{|V_{ud}|^2 (1 + 3\lambda^2)}$$

$$|V_{ud}|^2 = \frac{4908.7 \pm 1.9{\rm s}}{\tau_{\rm n} (1 + 3\lambda^2)} \tag{1.10}$$

where $\lambda = G_A/G_V$. From the neutron lifetime, we get $|V_{ud}| = 0.97520(140)$ [23]. With a current uncertainty of $\delta\tau_{\rm n} = 1$ second, the measurement is limited by the precision of the neutron lifetime $\tau_{\rm n}$ and λ. The most precise measurements of λ come from the beta asymmetry in neutron decay [24, 25], but there exists the possibility of measuring λ via the neutron β decay electron-antineutrino angular correlation [26]. The current best value is $\lambda = G_A/G_V = -1.2723(23)$. In order for a calculation of $|V_{ud}|$ to be competitive with the superallowed $0^+ \rightarrow 0^+$ results, the uncertainty on $\tau_{\rm n}$ would have to approach $\delta\tau_{\rm n} = 0.1$ second, and $\delta\lambda$ would have to reach ~ 0.0002.

1.1.2 Big Bang Nucleosynthesis

In the moments following the Big Bang, the energy density of the universe was so great that the Standard Model is inadequate to describe the dynamics. After a short period of time, quarks are bound into nucleons, and later, protons and neutrons are bound into the light elements ^{2}H, ^{3}He, ^{4}He, and ^{7}Li along with the remaining protons (H) in a process called Big Bang nucleosynthesis. The neutron lifetime $\tau_{\rm n}$ plays a critical role by controlling the number of neutrons left at the end of this long series of nuclear processes.

In the early universe, once quarks are bound into nucleons at about time $t =\sim 30\mu$s, and temperature $T =\sim 150$ MeV, protons and neutrons are in thermal equilibrium via coupling

to weak neutrino interactions and neutron decay:

$$\mathrm{n} + e^+ \leftrightarrow p + \bar{\nu}_e \qquad\qquad \mathrm{n} + \nu_e \leftrightarrow p + e^- \tag{1.11}$$

$$\mathrm{n} \rightarrow p + e^- + \bar{\nu}_e \tag{1.12}$$

The neutron to proton ratio n/p is given by Boltzmann's law during this period: $\mathrm{n}/p = \exp(-\Delta m/kT)$, where $\Delta m = |m_p - m_\mathrm{n}| = 1.293$ MeV is the n/p mass difference. As the universe continues to expand and cool, charged-current weak interactions (Eqn (1.11)) become too slow to maintain thermal equilibrium and "freeze out" at $t = t_f =\sim 2$ seconds, $T = T_f =\sim 0.7$MeV and only neutron decay remains [5, 27]. At this time, $\mathrm{n}/p \sim 1/6$. This evolves via neutron beta decay until the universe cools to a temperature at which deuterium can form at $t_d =\sim 150$ seconds, $T = T_d =\sim 100$ keV. While this is well below the deuterium binding energy of $B_D \simeq 2.2$ MeV, there exists a high enough density of photons of sufficient energy to cause photo-dissociation due to the small baryon to photon ratio $\eta_B \simeq 10^{-9}$. Finally, neutrons are rapidly absorbed to form deuterium, which is condensed almost entirely into ^{4}He [5]. With the neutron number n at $t = t_f$, and n$'$ at $t = t_d$, $\mathrm{n}' \simeq \mathrm{n} \times \exp(-t_d/\tau_\mathrm{n})$ (neglecting the 2 second difference between t_d and $(t_d - t_f)$). The ^{4}He mass fraction Y_p is therefore an excellent observable for tests of BBN models. Since half of the mass of ^{4}He is neutrons, the ^{4}He mass fraction is about twice the neutron mass fraction (ignoring the ^{4}He binding energy):

$$Y_p = \frac{^4\mathrm{He\ mass}}{\mathrm{total\ mass}} \simeq \frac{2\mathrm{n}'}{n' + p'} = \frac{2}{1 + p'/\mathrm{n}'} \tag{1.13}$$

where p' is the proton number at $t = t_d$. Using in $\mathrm{n}/p = \exp(-\Delta m/kT)$ and $\mathrm{n}' \simeq \mathrm{n} \times$

$\exp(-t_d/\tau_{\rm n})$ we get:

$$Y_p \simeq \frac{2\exp(-t_d/\tau_{\rm n})}{1+\exp(\Delta m/kT_f)} \tag{1.14}$$

We see that the uncertainty on this expression of the ^{4}He mass fraction is driven by the freeze-out temperature T_f of the charged-current weak interaction, the baryon-to-photon ratio η_B (which affects t_d), and the neutron lifetime $\tau_{\rm n}$. The precisions on the mass difference Δm and Boltzmann's constant k are much higher than these parameters. Measurements of the ^{4}He mass fraction and other light elements in the early universe are therefore constraining η_B (as in Fig. 1.2), while $\tau_{\rm n}$ is constrained by direct measurement as discussed throughout this thesis. Iocco et al [27] report the sensitivity of Y_p to the neutron lifetime goes as:

$$\Delta Y_p/Y_p = +0.72\Delta\tau_{\rm n}/\tau_{\rm n} \tag{1.15}$$

which is mainly due to the dependence of the neutrino cross section on $\tau_{\rm n}$, but also free neutron decay until $t = t_d$. Dubbers and Schmidt show [5] that a change in the accepted value of $\tau_{\rm n}$ from 885 seconds to 878 seconds results in a change in the Iocco [27] calculated value from WMAP of $Y_p = 0.2480\,(0.0003)$ by $\Delta Y_p = -0.0015$. Iocco used the best value for the neutron lifetime in 2010 of $\tau_{\rm n} = 885.7(8)$ seconds, which has since been revised to $\tau_{\rm n} = 880(1)$ seconds as discussed at the beginning of this chapter.

Models of BBN are therefore highly dependent on the precision achievable in measurements of the neutron lifetime $\tau_{\rm n}$ and it is especially important to resolve the current discrepancy between measurement techniques. While the neutron lifetime does not significantly constrain measured values of Y_p, once the uncertainty associated with Y_p is understood, it will be necessary to have a robust measurement of $\tau_{\rm n}$

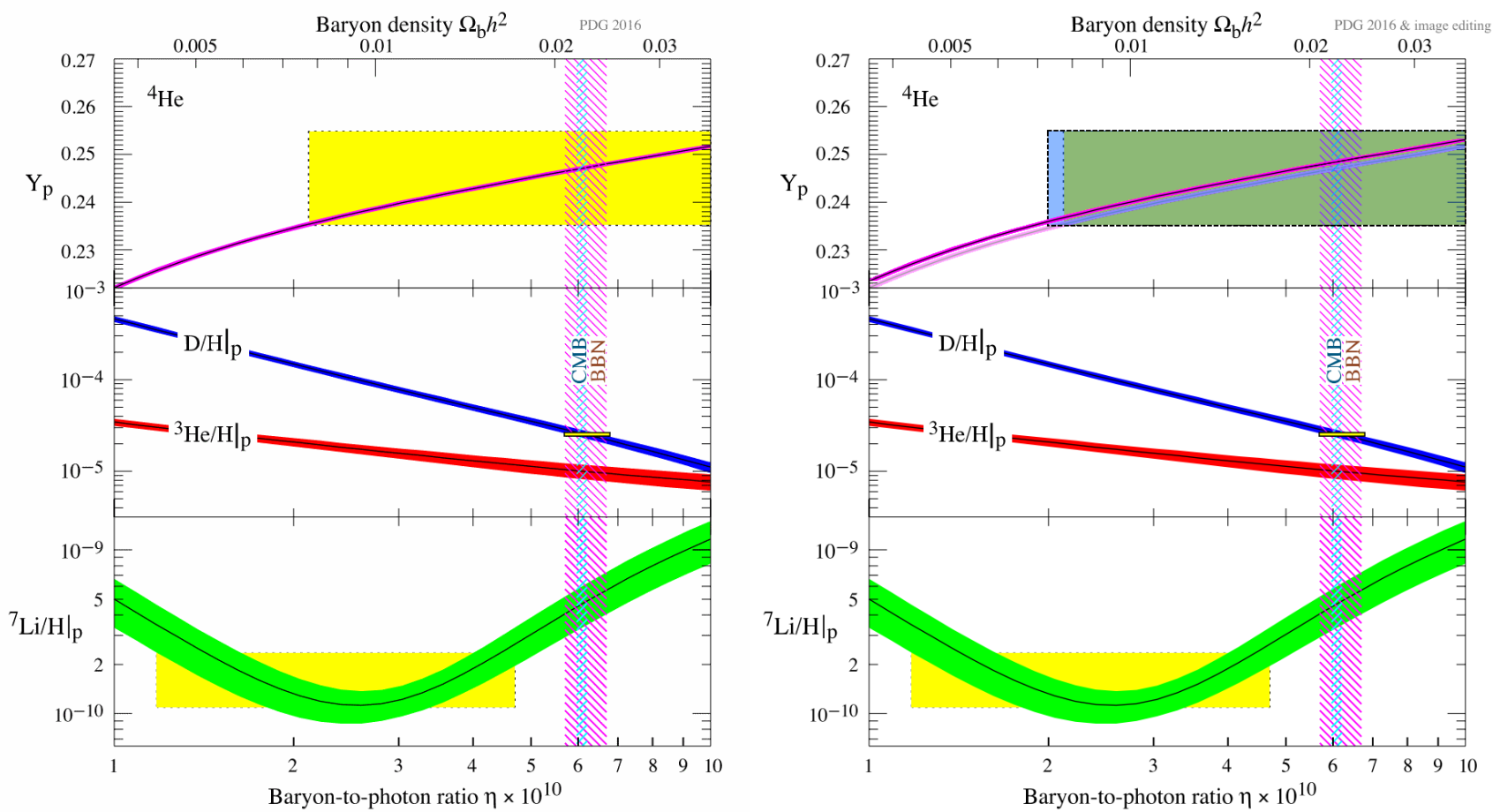

Figure 1.2: Left: A plot of the primordial mass fractions of light nuclei as a function of the baryon to photon ratio η_B (from [28] via [29]). The horizontal curves are the calculated values with error shown to 95% confidence level of Y_p. The yellow rectangles are the experimentally measured values. The narrow hashed band indicates the CMB measure of the cosmic baryon density (top axis). The wider hashed band indicates the BBN concordance range, which is primarily driven by the deuterium mass fraction measurements. Right: The same plot with a shift in the neutron lifetime from 880 seconds to ∼888 seconds. The new Y_p curve is not a real calculation since it was edited in place using image manipulation rather than computed. It is for illustrative purposes only.

1.2 The In-Beam Neutron Lifetime Experiment

The NIST In-Beam Neutron Lifetime experiment (see Fig. 1.3) uses a pseudo-Penning trap (the "proton trap") to trap the decay proton from a free neutron in a cold neutron beam (previously on the NIST Center for Neutron Research (NCNR) beamline NG-6, and currently NG-C) [1]. A nominally unpolarized neutron beam passes through the upstream side of the pseudo-Penning trap composed of 16 electrodes with potential barriers held at +800 V. Between this and the downstream +800 V potential well is a region held at ground. Protons from neutron decay have a maximum kinetic energy of 751 eV and are trapped axially by this potential barrier. A superconducting magnetic field held at 4.6 T contains the protons radially. Neutrons which do not decay continue downstream to the Flux Monitor, which measures the charged particles produced from neutron absorption on ^{6}Li to detect neutrons at a low but precisely-determined absolute efficiency. The electric potential barrier on the upstream-side of the proton trap is lowered at regular intervals and protons are guided out by a ramp potential. A bend in the 4.6 T magnetic field steers the protons to a solid-state silicon charged particle detector held at −30 kV. The high voltage is required to accelerate the decay protons to a kinetic energy high enough to be detectable above noise.

Since the neutrons are in-flight, the number of neutrons within the fiducial trapping volume is continuously renewed. At a flux of roughly 10^8 neutrons/s, the loss of neutrons from decay is an insignificant perturbation to the measurement of the neutron flux, and is well below the statistical fluctuations in the number of neutrons in the trap. The fiducial volume in effect contains a constant average number of neutrons proportional to the neutron flux. With the average number of neutrons in the trap at any given time as $\bar{N}_{\mathrm{n}}$, and the number of detected decay protons (equal to the number of neutron decays) as $\dot{N}_{\mathrm{n}}$, the

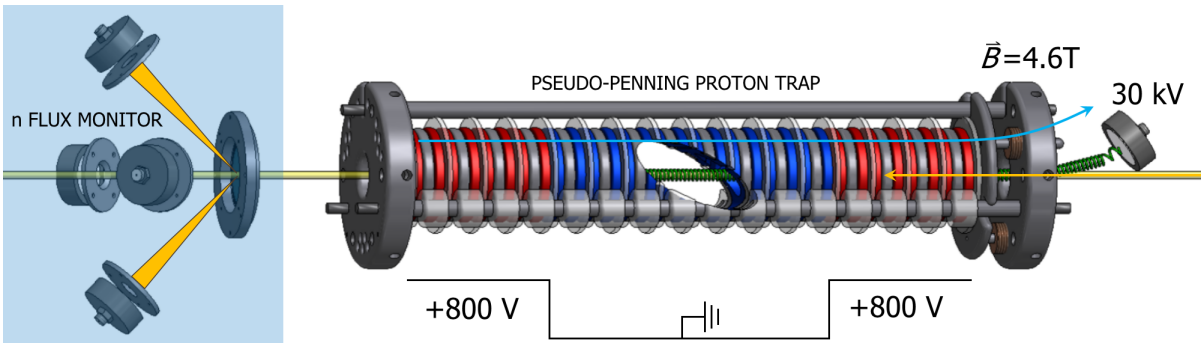

Figure 1.3: The core of the in-beam neutron lifetime experiment is the combination of the proton counting and neutron flux counting apparatus. Neutrons enter from the right. A set of 16 electrodes maintain a trapping volume with +800 V walls. If a neutron decays, the proton is trapped by the magnetic and electric fields. The downstream flux monitor measures the neutron flux in the thermal neutron beam with high absolute accuracy.

neutron lifetime is written most simply as:

$$\tau_{\mathrm{n}} = -\bar{N}_{\mathrm{n}}/\dot{N}_{\mathrm{n}} \tag{1.16}$$

where N_{n}, the instantaneous number of neutrons in the beam, is a function of the velocity-dependent intensity of the beam $I(v)$ and the fiducial trapping volume L, while the real proton rate $\dot{N}_p^{real}$ is a function of N_{n} and the neutron lifetime τ_{n}:

$$N_{\mathrm{n}} = L \int_A \int I(v) \frac{1}{v} dadv \tag{1.17}$$

$$\dot{N}_p^{real} = \frac{\dot{N}_p}{\epsilon_p} = \tau_{\mathrm{n}}^{-1} N_{\mathrm{n}} = -\dot{N}_{\mathrm{n}} \tag{1.18}$$

where $\dot{N}_p$ is the measured proton rate, and ϵ_p is the detector efficiency for decay protons. Combining Eqns. (1.16)- (1.18) yields:

$$\dot{N}_p = \tau_{\mathrm{n}}^{-1} \epsilon_p L \int_A \int I(v) \frac{1}{v} dadv \tag{1.19}$$

The dependence of the neutron lifetime $\dot{N}_p$ on $I(v)$ can be problematic. A monochro-

matic neutron beam has a well-defined $I(v)$ but a very low neutron flux, rendering such a beam unsuitable for the measurement. Polychromatic beams have sufficient flux, but the measurement of the velocity dependence is difficult to perform precisely and can change arbitrarily in time depending on the conditions of the neutron source and moderator. The low-absorption Flux Monitor, which uses a thin deposit of ^{6}Li on a silicon substrate to detect neutrons via the $^6\mathrm{Li}(\mathrm{n},t)\,\alpha$ reaction, solves this problem neatly.

For all neutron absorption cross sections in nuclei without low energy resonances, the reaction rate at low energies (typically near thermal, or ~ 25 meV) increases as $1/v$. For a large body of isotopes (most notably those popular for nuclear energy applications), the presence of resonances at higher energies and the long tail of the Maxwell-Boltzmann distribution, which is typical of the energy of a polychromatic flux of neutrons, leads to deviations from the $1/v$ behavior and requires a correction described by the Westcott g-factor in order to describe a reaction rate using the mean neutron energy [30]. ^{6}Li is free of resonances except at very high energies (~ 225 keV), making it an ideal candidate for the exploitation of the "$1/v$ law" of neutron cross sections for our purpose.

A thermal neutron incident upon ^{6}Li possesses a cross section of $\sigma_0 = 938.5$ b for the $^6\mathrm{Li}(\mathrm{n},t)^4\mathrm{He}$. Since ^{6}Li produces only charged particles in this reaction, and the neutron kinetic energy is very small compared to the Q-value of the reaction, the triton and alpha are emitted with characteristic energies $E_\alpha = 2.056$ MeV and $E_t = 2.727$ MeV. The angular distribution is isotropic. By using a very thin deposit of ^{6}LiF (supported by a silicon substrate) as the reaction target in the Flux Monitor, there is very little attenuation or loss of energy as the charged particles escape the material. The Lambert-Beer law of attenuation describes the neutron intensity I through the material and its subsequent attenuation (about 1%) over a length z as [31]:

$$\begin{aligned} I(v) &= I_0 e^{-\rho\sigma(v)z} \\ \frac{\mathrm{d}I(v)}{\mathrm{d}z} &= -\rho\sigma(v) I(v) \end{aligned} \tag{1.20}$$

Since the attenuation results from neutron absorption in the ^{6}Li(n, t)^{4}He reaction, integration over the beam velocity and area yields the reaction rate (and therefore the charged particle production rate into 4π):

$$\dot{N}_{\alpha+t}^{real} = \int_A \int I(v) (\rho\sigma(v)) \, dadv \tag{1.21}$$

The Flux Monitor detects charged particles via the four solid-state Si detectors and their respective stainless steel apertures. The apertures define a small but precisely-measured solid angle with respect to the ^{6}Li target center. The velocity-dependent efficiency $\epsilon(v)$ is then a function proportional to $\rho\sigma$, and the detected charged particle fraction $\dot{N}_{\alpha+t}$ is:

$$\dot{N}_{\alpha+t} = \int_A \int I(v) \epsilon(v) \, dadv \tag{1.22}$$

By the 1/v law, the efficiency of the FM for a polychromatic thermal neutron beam can be written in terms of its efficiency and the neutron velocity at a reference thermal energy:

$$\epsilon(v) = \frac{\epsilon_0 v_0}{v} \tag{1.23}$$

Combining Eqns. (1.22) and (1.23),

$$\dot{N}_{\alpha+t} = \epsilon_0 v_0 \int_A \int I(v) \frac{1}{v} dadv \tag{1.24}$$

Equations (1.19) and (1.24) are then used to solve for the neutron lifetime τ_{n}:

$$\tau_{\mathrm{n}} = \frac{L}{\dot{N}_p} \frac{\dot{N}_{\alpha+t}}{\epsilon_0} \frac{\epsilon_p}{v_0} \tag{1.25}$$

Note the significance of the independence of the neutron lifetime expression to both velocity-dependent terms $I(v)$ and $\frac{1}{v}$. Since the ^{6}Li cross-section $\sigma(v)$ increases with $1/v$, and the dwell time of neutrons within the fiducial trapping volume increases by the same proportion, a neutron which spends half as long in the trapping volume is half as likely to be detected in the Flux Monitor. This clever feature of the in-beam neutron lifetime experimental design was first used successfully by Christensen [32].

The previous determination of the FM efficiency ϵ_0 at NIST was done by precise characterization of the ^{6}Li targets and by measuring the solid angle subtended by the apertures for the FM target center (see Sec. 2.7). Contributions to the uncertainty budget of the previous in-beam neutron lifetime measurement at NIST were dominated by terms associated with the determination of ϵ_0 by these methods (see Table 1.1). The work reported in this thesis seeks to overcome this limitation.

This thesis will describe the efforts to date to utilize the capabilities of the Alpha-Gamma experiment to calibrate the neutron Flux Monitors. It will also discuss our efforts to use the Flux Monitors and Alpha-Gamma for other nuclear physics applications such as neutron detector calibration, neutron cross section measurement, and neutron source activity measurement. In order to provide full and complete documentation in a single location for future scientists to reproduce these experiments, I will go into significant detail in many places.

I have worked on all aspects of the experiment since 2014. This includes primary data taking using Alpha-Gamma, measurements of the ^{239}Pu source, redetermination of most systematics based on new data and new or corrected methodology, and the expansion of

Table 1.1: The corrections and uncertainty budget for the 2005 result by Nico et. al. [1]. Highlighted are the corrections which depend only on characteristics of the Flux Monitor. Note that these uncertainties dominate the error budget. By improving the absolute accuracy with which the efficiency ϵ_0 of the FM is determined, the in-beam neutron lifetime experiment can achieve higher precision.

Source of correction	Correction (s)	Uncertainty (s)
^{6}LiF deposit areal density		2.2
^{6}Li cross section		1.2
Neutron detector solid angle		1.0
Absorption of neutrons by ^{6}Li	+5.2	0.8
Neutron beam profile and detector solid angle	+1.3	0.1
Neutron beam profile and ^{6}Li deposit shape	-1.7	0.1
Neutron beam halo	-1.0	0.1
Absorption of neutrons by Si substrate	+1.2	0.1
Scattering of neutrons by Si substrate	-0.2	0.5
Trap nonlinearity	-5.3	0.8
Proton backscatter calculation		0.4
Neutron counting dead time	+0.1	0.1
Proton counting statistics		1.2
Neutron counting statistics		0.1
Total	-0.4	3.4

the scope of Alpha-Gamma to include new measurements and goals beyond the in-beam neutron lifetime Flux Monitor calibrations. I designed new components for the experiments as needed, and recommissioned the Flux Monitor used in the 2005 in-beam neutron lifetime, which had been compromised. I also designed components of the in-beam neutron lifetime experiment and participated in its commissioning during this time, but that is outside of the scope of this thesis.

Data prior to 2014, which includes much of the data used to calculate corrections, were collected by Andrew Yue. I performed an independent analysis of the corrections.

Chapter 2

Alpha-Gamma Experimental Overview

The Alpha-Gamma apparatus is designed to measure the absolute flux of neutrons in the NG-6m monochromatic beamline operating at the NCNR to high precision. The original goal of the apparatus was to measure the absolute efficiency ϵ_0 of the NIST in-beam neutron lifetime flux monitor to sub-0.1% absolute precision in order to reduce the magnitude of the uncertainty associated with neutron counting [4]. This is essentially done by directly measuring the neutron beam flux with a totally-absorbing detector that is calibrated to high absolute accuracy.

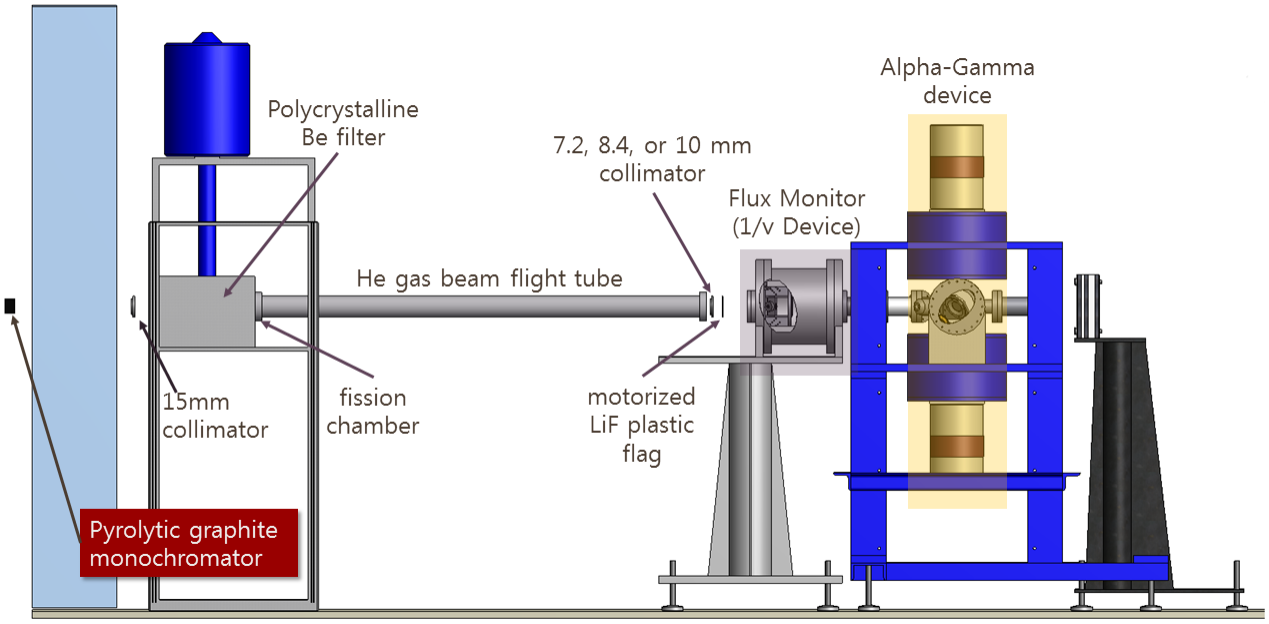

Neutrons from the monochromatic neutron beam NG-6m are absorbed on a totally-

absorbing disc of $^{10}B_4C$. The products from the n+^{10}B reaction include an alpha particle and a ^{7}Li ion. 93.7% of the time, the ^{7}Li nucleus is produced in an excited state which rapidly decays with a 73 fs half-life, emitting a 478 (477.612) keV gamma ray [33] [34]. These gammas are detected in a pair of high-purity germanium (HPGe) gamma detectors, while the emitted alpha particles are detected in a well-calibrated solid-state silicon charged particle detector (Si detector). This process has a Q-value of $Q_{\mathrm{m}} = 2.7900$ MeV [35]. The kinetic energy of the charged particles resultant from both decay modes can be calculated by energy and momentum conservation. When the ^{7}Li is emitted in the ground state (decay mode α_0), the kinetic energy of the emitted alpha is $E_\alpha = 1.776$ MeV, and the ^{7}Li is $E_{^7\mathrm{Li}} = 1.014$ MeV. When the excited state of ^{7}Li is populated (α_1), $E_\alpha = 1.472$ MeV, and $E_{^7\mathrm{Li}} = 0.840$ MeV. If the Si detector can be used to calibrate the HPGe detectors to high precision, the neutron flux can be determined using only the gamma detector rates. With the absolute flux determined, a low-absorption neutron detector can be placed upstream and, with a small number of apparatus-dependent corrections, the efficiency of that device can be determined to the same high precision for a particular neutron velocity v.

2.1 Theory of Measurement

The full measurement can be thought of as a "transfer calibration procedure," wherein a high-precision measurement of the absolute α-activity of a ^{239}Pu source is used to calibrate the Alpha-Gamma Si charged particle detector, which in turn is used to calibrate the HPGe detectors. The Alpha-Gamma kinematic target mounting system enables the ^{239}Pu source to be exchanged for a thin $25\mu g/cm^2$ deposit of ^{10}B on a silicon backing (the 'thin target') without losing position with respect to the target center. The thin target is thin enough that the alpha particles from the neutron interaction can escape with no significant attenuation in either yield or energy. Neutrons with a wavelength of $\sim$ 0.5nm from NG-

6m incident upon the thin target are used to calibrate the HPGe detectors. During this phase of the calibration, both the Si detector and the HPGe detectors witness the same neutron events. The total number of events are known because the Si detector has been calibrated. Therefore, the ratio of the number of gammas per alpha counted is equivalent to a measurement of the number of gammas per neutron event. The thick target is necessary to absorb the entire neutron beam. It is too thick for the majority of alpha particles to escape, but thin enough that there is only $\sim 0.5\%$ gamma attenuation. Since the HPGe detectors are calibrated, the absolute measurement of the neutron flux ultimately proceeds as a measurement of the gamma count rate.

2.2 Absolute Activity of the ^{239}Pu Alpha Source

Alpha particles from the ^{239}Pu source are emitted isotropically into 4π. By precisely defining the solid angle subtended by a Si detector detector for the deposit, the absolute activity can be determined (Fig. 2.1). This is done using a stack of precision, scatter-suppressing spacers and a diamond-turned copper aperture as described in Sec. 4.4. The real alpha source activity is written as R_{Pu}. At E> 4MeV [36], the emitted particles have essentially unit efficiency for detection by the Si detector. The number of detected particles $r_{Pu}(stack)$ depends on the solid angle $\Omega(stack)$:

$$R_{Pu}\Omega(stack) = r_{Pu}(stack) \tag{2.1}$$

where, $\Omega(stack)$ is the fractional solid angle relative to the full sphere 4π. It is then trivial to solve for the absolute activity in terms of measurable quantities:

$$R_{Pu} = r_{Pu}(stack)/\Omega(stack) \tag{2.2}$$

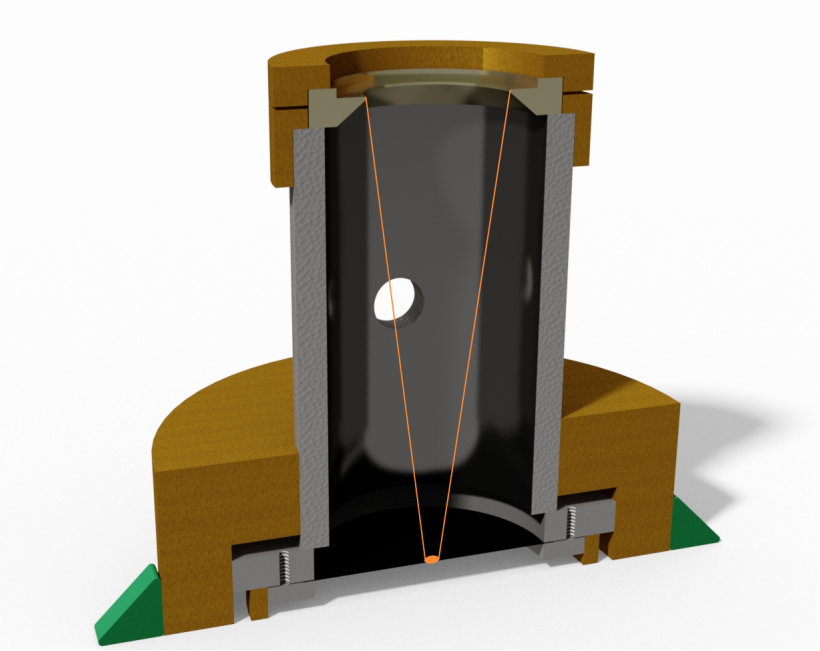

Figure 2.1: A rendering of the low solid angle counting stack used to measure the absolute activity of the ^{239}Pu source. The orange lines indicate the dimensions of the precisely measured solid angle. The orange spot is an approximation for illustrative purposes. This series of images are inspired by A. Yue's renderings of the same apparatus.

2.3 Alpha-Gamma Si detector calibration

In order for the calibration of the Alpha-Gamma Si detector to be meaningful, it is necessary to determine the fractional solid angle Ω_{AG} subtended by the detector for the neutron beam target region. This is done by placing the ^{239}Pu deposit in the Alpha-Gamma apparatus using kinematic target mount and counting the emitted alpha particles in the AG Si detector:

$$\begin{aligned} r_{Pu}(AG) &= R_{Pu}\Omega_{AG} \\ r_{Pu}(AG)/R_{Pu} &= \Omega_{AG} \end{aligned} \tag{2.3}$$

where $r_{Pu}(AG)$ is the measured rate of alpha particles emitted from the ^{239}Pu source. Since the target holder position and orientation will not change when the alpha source is exchanged for either the thick or thin ^{10}B target, the measurement of Ω_{AG} can be applied to data collected with these targets as well (with a correction for the difference in spot size

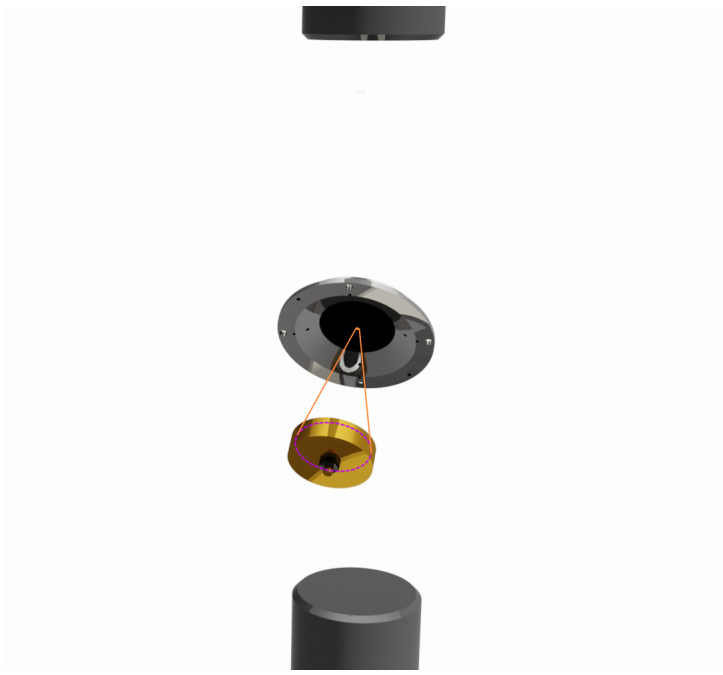

Figure 2.2: A rendering of the ^{239}Pu source calibration of the solid angle of the Alpha-Gamma alpha detector. The orange dot is the ^{239}Pu spot. The lines show the solid angle subtended by the Si detector for the ^{239}Pu spot.

between the source and the beam).

2.4 Alpha-Gamma HPGe Detector Calibration

The thin target is used in combination with the NG-6m 0.496 nm monochromatic neutron beam to calibrate the HPGe detectors. Neutrons are absorbed in the thin ^{10}B deposit at a rate $r_n(thin)$ which is given to first order as:

$$r_n(thin) = R_n \sigma \rho_N \Omega_{AG} \tag{2.4}$$

where R_n is the total neutron rate , ρ_N the areal number density of ^{10}B in the target, and σ is the $^{10}\mathrm{B}(n,\alpha)^7\mathrm{Li}$ cross-section at the energy of neutrons in the NG-6m beam. Recall that 93.7% of the time, the ^{7}Li ion is produced in the first excited nuclear state, which rapidly ($\tau = 73$ fs [37]) decays emitting a 478 keV gamma ray [33].

Charged particles and gamma rays are emitted isotropically and simultaneously detected in both the Si and the HPGe detectors producing detection rates given as $r_\alpha(thin)$ and $r_\gamma(thin)$ respectively. The neutron absorption rate $r_n(thin)$ is directly detected via

$$r_n(thin) = r_\alpha(thin)/\Omega_{AG} \tag{2.5}$$

while the detection rate of emitted gamma particles in HPGe detectors is given by

$$\epsilon_\gamma r_n(thin) b_{\alpha\gamma} = r_\gamma(thin) \tag{2.6}$$

where ϵ_γ is the gamma detection efficiency of the HPGe detectors and $b_{\alpha\gamma}$ is the branching ratio for the $^{10}\mathrm{B}(n,\alpha)^7\mathrm{Li}$ absorption channel to emit a 478 keV gamma ray (Fig. 2.3). Combining Eqns. (2.5) and (2.6), ϵ_γ can be written purely in terms of measurable quantities and the branching ratio $b_{\alpha\gamma}$:

$$\epsilon_\gamma = \frac{1}{b_{\alpha\gamma}} \frac{r_\gamma(thin)}{r_n(thin)} = \frac{1}{b_{\alpha\gamma}} \frac{r_\gamma(thin)}{r_\alpha(thin)} \Omega_{AG} \tag{2.7}$$

2.5 Alpha-Gamma Absolute Flux Measurement

With the HPGe gamma detection efficiency ϵ_γ determined, the thick target can be placed in the Alpha-Gamma target holder and used to absorb the entire beam (Fig. 2.4). The neutron rate R_n is measured in terms of the detected gamma rate:

$$r_\gamma(thick) = R_n b_{\alpha\gamma} \epsilon_\gamma \tag{2.8}$$

Plugging in Eqn. (2.7) for ϵ_γ, we find that the two factors of the branching ratio $b_{\alpha\gamma}$ cancel in the expression for the absolute flux:

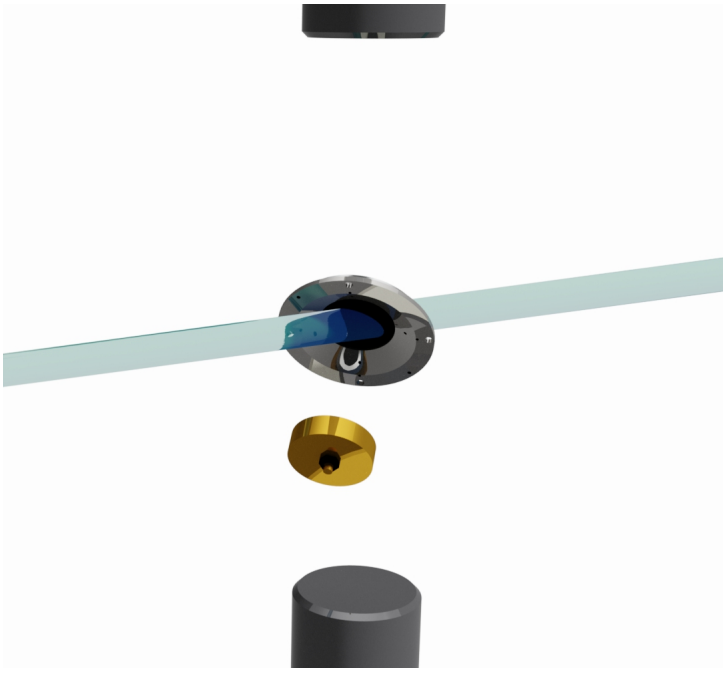

Figure 2.3: A rendering of the HPGe detector calibration phase. The thin ^{10}B target is used to measure the rate of 478 keV gamma rays per detected alpha particle from the $^{10}\mathrm{B}(\mathrm{n},\alpha)^{7}\mathrm{Li}$ reaction.

$$R_n = \frac{r_\gamma(thick)}{b_{\alpha\gamma}\epsilon_\gamma} = r_\gamma(thick)\frac{r_\alpha(thin)}{r_\gamma(thin)}\frac{1}{\Omega_{AG}} \tag{2.9}$$

2.6 Flux Monitor Efficiency Measurement

Now that the absolute flux can be measured purely in terms of observable quantities, Alpha-Gamma is prepared to measure the efficiency of a low-absorption neutron detector upstream of the apparatus such as the in-beam neutron lifetime Flux Monitor (Fig. 2.5). This measurement follows the same procedure, and the measured rate in the Flux Monitor is given as

$$r_{FM} = \epsilon R_n \tag{2.10}$$

Replacing R_n using Eqn. (2.9) and solving for the efficiency ϵ,

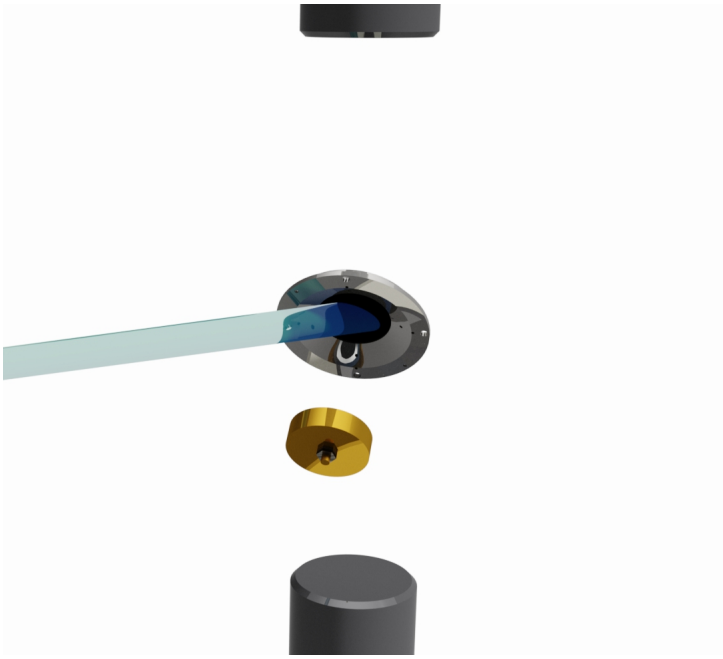

Figure 2.4: A rendering of the absolute flux measurement using the thick target in Alpha-Gamma. The thick $^{10}B_4C$ target absorbs the full beam, and the calibrated HPGe detectors measure the absolute flux.

$$\epsilon = \frac{r_{FM}}{r_\gamma(thick)} \frac{r_\gamma(thin)}{r_\alpha(thin)} \Omega_{AG} \tag{2.11}$$

The Flux Monitor detects neutrons using a thin deposit of ^{6}LiF upon a silicon backing. There exist ^{6}LiF deposits with areal densities of $\sim 20, \sim 30,$ or $\sim 40 \mu g/\text{cm}^2$ by weight in ^{6}Li. Neutrons are absorbed via the $^6\text{Li}\,(n,t)\,\alpha$ channel which, like many materials used for neutron detection, has a high thermal neutron cross section (σ = 940b) and a high Q value (Q= 4.7829 MeV) [37]. Reaction products are emitted into 4π and detected in four Si detectors viewing the deposit at regular intervals around the transverse directions with an incident angle of 45° from normal. Four precision-ground stainless steel masks precisely define the geometry of the detectors with respect to the target holder center.

For neutron energies below 10^4 eV, the neutron cross section for the $^6\text{Li}(n,t)^4\text{He}$ reaction channel increases as the inverse of the velocity (1/v) to high accuracy. Since the detection efficiency depends directly on the reaction rate as seen in Eqn. (2.5), this allows

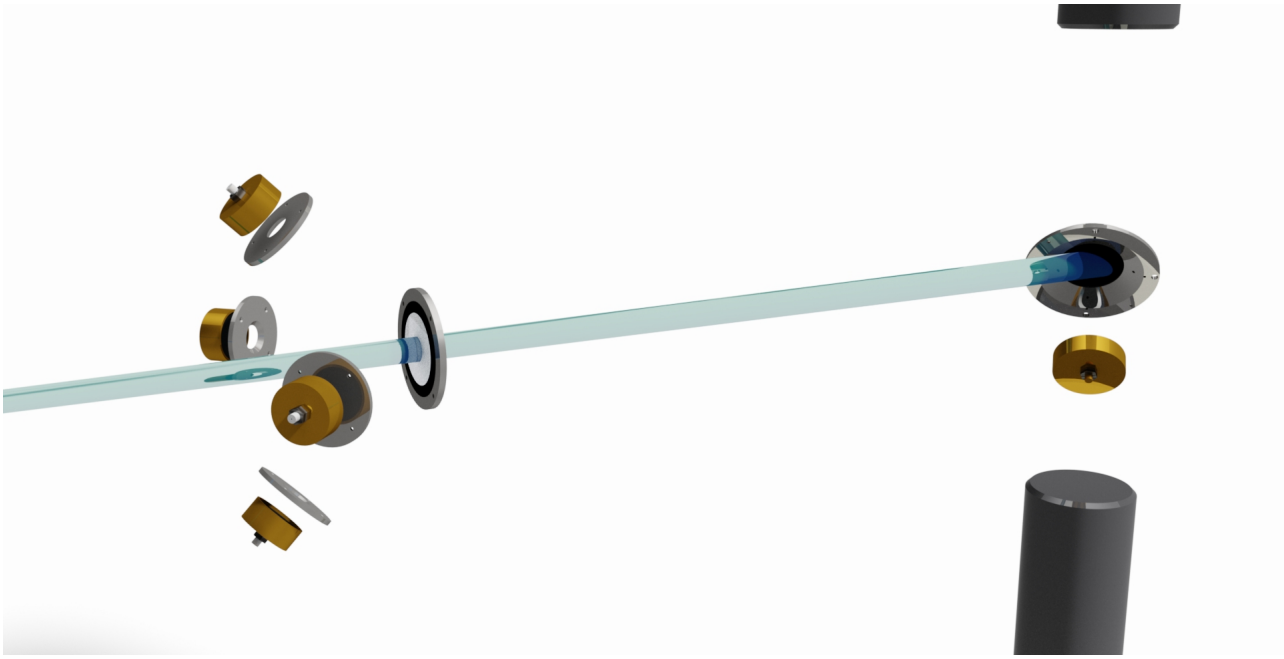

Figure 2.5: A rendering of the quintessential Flux Monitor calibration during the thick target measurement.

the determined flux monitor efficiency ϵ to be extrapolated to the full energy range of most thermal neutron beams. The expression comes from straightforward algebra. Since the neutron cross section increases as 1/v, the product of the cross section at any neutron energy in this region and the velocity at that energy are a constant, and:

$$\sigma_0 v_0 = \sigma v \tag{2.12}$$

where σ_0 is defined as the neutron cross section at thermal ($v_0 = 2200$m/s) velocity. This is what makes the neutron monitor devices portable between neutron beamlines of different energy profiles. The efficiency is rewritten in terms of the efficiency for neutrons at thermal energies:

$$\sigma_0 = \frac{\sigma_{NG-6m} v_{NG-6m}}{v_0} \tag{2.13}$$

where σ_{NG-6m} is the $^6\mathrm{Li}(n,t)^4 He$ neutron cross section for $\lambda = 0.496$ nm neutrons in the

monochromatic neutron beam NG-6m, and v_{NG-6m} is the mean velocity of the NG-6m neutrons. In order to use the flux monitor on a different neutron beam, the full energy spectrum must be measured and the efficiency determined across the measured spectrum.

2.7 Previous Calculation of ϵ_0

In the previous method for the measurement of the Flux Monitor efficiency, ϵ was determined by careful measurements of the solid angle subtended by the masks for the target center combined with precise assay of the areal number densities of the ^{6}Li deposits [1] [38]:

$$\epsilon_0 = \frac{2N_A\sigma_0}{4\pi A}\iint \Omega(x,y)\,\rho(x,y)\,\phi(x,y)\,dxdy \tag{2.14}$$

where N_A is Avogadro's constant, σ_0 is for thermal neutrons as before, A is the atomic weight of ^{6}Li, $\Omega(x,y)$ is the solid angle subtended by the four Si detectors in the FM for the areal coordinates (x,y), $\rho(x,y)$ is the areal mass density distribution of ^{6}Li in the deposit, and $\phi(x,y)$ is the neutron beam intensity areal distribution on the target. Since the Flux Monitor may be operated on many different beamlines with different characteristics, its efficiency ϵ_{FM} is recorded in terms of an idealized neutron beam incident upon the center of an idealized deposit. While the choice is arbitrary, the widespread use of thermal neutron velocity $v_{\rm n} = 2200$ m/s as a standard reference point defines v_0, and the simplest geometries are chosen. The "idealized beam" is an infinitely-narrow beam of thermal neutrons incident upon the center of the target deposit. The "idealized deposit" is an infinitely-thin deposit of ^{6}Li without target substrate. Eqn. (2.14) then becomes:

$$\epsilon_0 = \frac{2N_A\sigma_0}{4\pi A}\Omega(0,0)\,\rho(0,0) \tag{2.15}$$

The solid angle subtended by the precision apertures for the FM target center was

determined in two separate ways: by touch metrology on a coordinate measuring machine at NIST, and by charged particle counting using a ^{239}Pu source just as in the determination of Ω_{AG} in Alpha-Gamma [39]. Though the measurements were made several years apart, they agreed to better than 0.1%.

Touch metrology of the Rig 1 FM solid angle Ω_{FM} was performed by David Gilliam and Geoffrey L. Greene in 1989 at the National Institute of Standards and Technology. Stainless steel solid angle defining apertures situated between each Si detector of the FM and the target center were machined with a conical bevel facing away from the detector (Fig. 2.6). This allowed for a precision steel ball to rest in contact with the edge of the feature which defines the solid angle. Touch metrology determines both the plane of intersection that describes the circular edge, and the position of the center of the steel bearing above that plane. Since the radius of the steel bearing and its sphericity are known to high precision due to stringent manufacturing standards and requirements of these widely-used mechanical components, the precise diameter of the aperture can be determined. By then locating the target center and the orientation of each aperture with respect to that center, the solid angle Ω_{FM} can be calculated.

A second round of touch metrology was performed by NCNR Research Facility Operations (RFO) staff member Dan Adler using a specialized FaroArm coordinate measuring machine. The FaroArm tracks the position of a highly precise probe using a set of encoders and servos. The bevel on the stainless steel apertures does not come to a sharp point; instead, there is a small (0.0508 mm) cylindrical section between the bevel and the plane. The FaroArm is precise enough to measure the radius of that cylinder. Using the radius of the cylinder and the Si detector-facing plane (the same plane as earlier), the precise shape and position of the aperture is quickly determined. The FaroArm has the added advantage of measuring the circularity of the aperture edge.

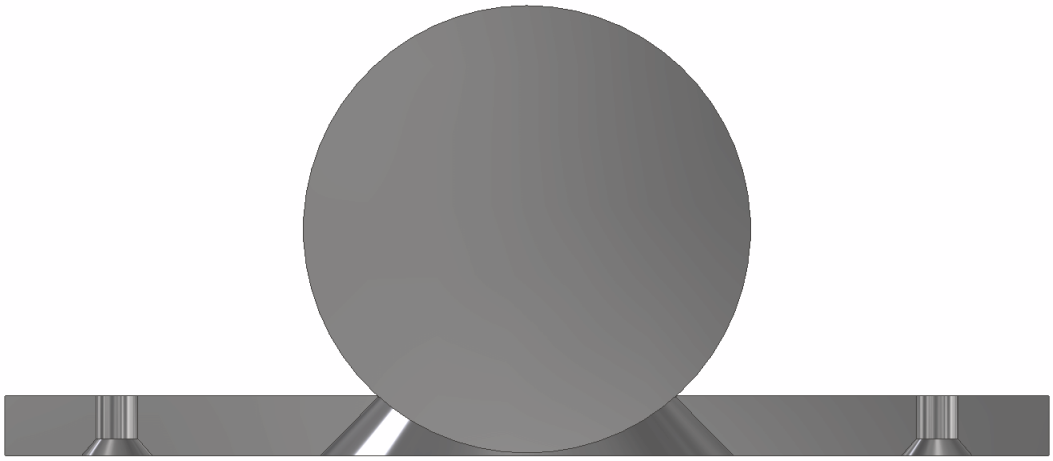

Figure 2.6: The cross-section the steel bearing resting on the solid angle defining aperture. By knowing the precise radius of the bearing and the position of the plane of intersection, the diameter of the circle describing the solid angle can be determined.

The diameter measurements of the three campaigns (ball touch metrology by Gilliam 1989, coordinate measurement using CMM M48 by Stoup 2012, and FARO device by Adler 2017) disaagree slightly (see Table 2.1). The FARO measurement apparatus is certified only for volumetric uncertainty which makes the extrapolation to a linear uncertainty less reliable. Nevertheless, the new data suggests that no dramatic changes are likely to have occurred due to handling, mishandling, or mishap.

In conjunction with the FARO measurements, a set of alignment corner cube fixtures were attached to the Rig #1 flange on the atmosphere side. With the corner cubes, alignment can be performed using the FARO laser tracker without exposing the volume to atmosphere or removing the target. This requires sighting of the NG-6m beam using FARO technology in order to place beamline artifact corner cubes. Rapid exchange of the Flux Monitor Rigs with the in-beam neutron lifetime experiment would then be possible. The alignment achievable with this system even with the differences in measurement precision is superior to anything achievable via theodolite alignment determination.

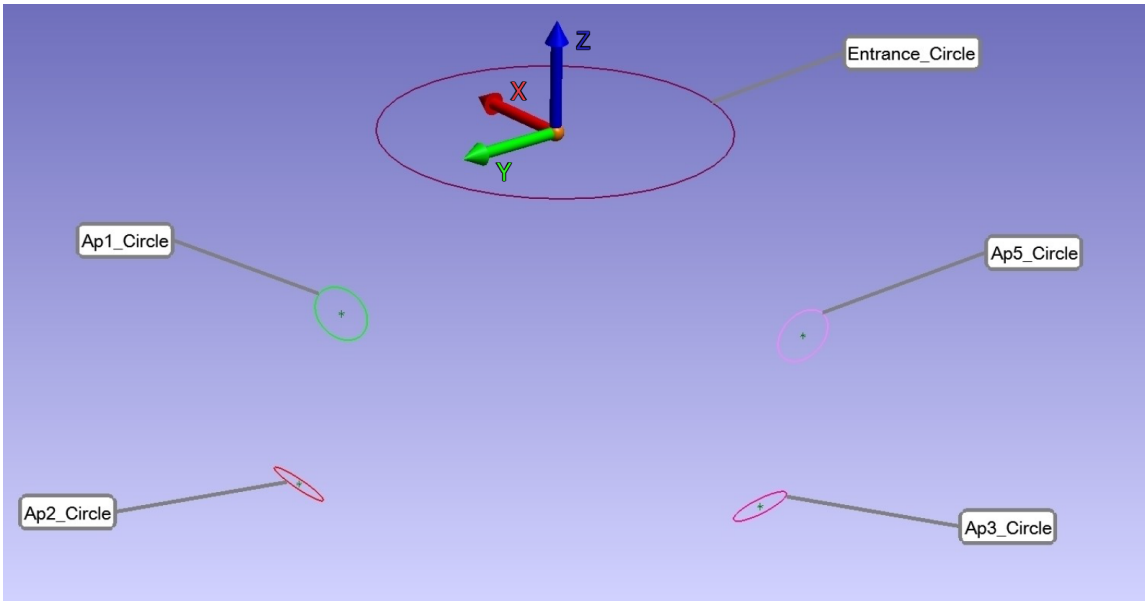

Figure 2.7: Output from the FARO measurements. In the Alpha-Gamma experiment, neutrons would enter from the $-$Z direction and interact with the target at Z=$\sim$ +6.35 mm. The circles indicate where the aperture bore meets the flat detector-facing side of the aperture.

Target deposits (both ^{6}Li and ^{10}B) were manufactured at the Institute for Reference Materials and Measurements (IRMM) in Geel, Belgium in two separate campaigns [38, 40]. All deposits used in this work and the in-beam neutron lifetime experiment come exclusively from the second campaign for reasons discussed below. Target materials were deposited by evaporation onto perfect crystal silicon wafers masked with precision-ground apertures mounted in a holder which performed both orbital and planetary rotation to ensure the deposit layers were as flat and as identical as possible. While the deposits produced exhibit excellent equivalence between each other, there is a slight curve to the density profile which must be characterized, giving rise to a position-dependent term $\rho(x, y)$ in the expression for the efficiency. This variation combined with the change in the effective solid angle for a non-pointlike neutron beam necessitates a measurement of the neutron beam profile $\phi(x, y)$ as well to characterize the efficiency.

For each set of target deposits, two deposits upon stainless steel substrates were created

Table 2.1: Metrology results of Apertures for Rigs (in mm)

Aperture #	Gilliam & Greene (1989)	Stoup[2](2012)	Adler (2017)
1[1]	12.680	12.69146	12.715
2[1]	12.695	12.70274	12.708
3	12.692	12.70196	12.710
4	12.682	–	–
5[1]	12.692	12.70224	12.708
6	12.703	–	–
7	12.703	–	–
8	12.697	–	–
9	12.700	–	–
10	12.700	–	–
Uncertainty	±.005	±.00041	±.005

[1] These apertures are used on Rig 1 of the Flux Monitors.
[2] The average of the two measurements at two different places on the aperture edge is used

in addition to the deposits upon silicon substrates. The deposits on stainless steel were used during the effort to characterize the amount of ^{6}Li in the target deposits via a destructive process called Isotope Dilution Mass Spectrometry (IDMS), which is described later in this text. IDMS accurately measures the total number of ^{6}Li atoms in a sample (the term A for the target deposits). By first measuring the thermal-neutron-induced charged particle reaction rate of the deposits to be destroyed in IDMS, the mass of target material deposited upon each silicon-backed target can be determined using the same apparatus by relative charged-particle count rate comparison [41] [42].

The precision accessible via this technique was limited by the accuracy of the IDMS measurement (and thereby the areal number density) of ^{6}Li in the deposit, and the absolute knowledge of the thermal neutron cross section for the reaction channel exploited. As a direct measurement, the technique described for new measurements of ϵ using the Alpha-Gamma device is first-order independent of the cross section and areal number density of ^{6}Li. In addition, the determination of the solid angle presented by the apertures in the FM

to the target center is demoted to a correction to the final expression for ϵ.

Chapter 3

^{6}Li and ^{10}B Target Deposit Characterization

The ^{6}Li and ^{10}B deposits used in the Alpha-Gamma experiment were prepared in a second production run of well-characterized thin-film neutron absorbers for the neutron lifetime experiment [38] [42]. An earlier campaign [40] [41] produced a set of deposits as well, but these went unused in the final experiment due to characterization difficulties.

Careful preparation of the ^{6}Li and ^{10}B deposits is critical to our ability to characterize the systematic contributions to uncertainty in the experiment. The mean areal density of each deposit influences corrections due to neutron and charged particle transmission through the targets as well as absorption of backscattered neutrons off of the silicon substrate. The incident neutron beam profile combines with the target number density profile across the deposit to calculate corrections which describe the efficiency in terms of an infinitely narrow beam upon an infinitely thin deposit. This parameterization of the efficiency is required in order to calculate the Flux Monitor efficiency when used with other beamlines.

Once the target deposits have been created, the areal density of the active isotope within the deposits must be measured absolutely. This requires not only a determination of the *shape* of the deposit ($\rho_{\text{LiF molecules or B atoms}}(x, y)$), but also the total mass of the active isotope (^{6}Li rather than natural Li, for instance). The uniformity is determined by visible light interferometry and the dimensional characterization by traveling microscope and Talistep measurement. The isotopic analysis is determined via IDMS [43], which is

sometimes called Isotope Dilution Analysis (IDA) in the literature. Since this is a destructive process, a relative comparison must be made between a target assayed by IDMS and targets which can be used in experiments. This is done by comparison of neutron-induced charged particle rates of the surviving deposits to the measured rate of the targets which were later destroyed for analysis.

The thick $^{10}B_4C$ targets will also be discussed in this chapter.

3.1 ^{6}Li and ^{10}B Target Deposit Preparation

The manufacture of both the ^{6}Li and ^{10}B deposits occurred at the Institute for Reference Materials and Measurements (IRMM) in Geel, Belgium through a joint effort with NIST. By simultaneously creating multiple deposits in a carefully designed vacuum deposition apparatus, a subset of the targets could be destructively assayed using IDMS to determine the number density of target atoms on the remaining deposits. The challenge was then to control the evaporation and deposition in such a way that each deposit was identical. Six sets of ^{10}B deposits were created with nominal area densities of 10, 12.5, 15, 20, 25 and 30 μg ^{10}B/cm^2, and three sets of ^{6}Li deposits with densities of 20, 30, and 40 μg/cm^2. Two deposits per evaporation were produced on stainless steel substrates for isotopic analysis and radial deposit distribution determination.

A rotating multi-substrate holder (Fig. 3.1) used in the second target deposit campaign held seven substrates in vacuum above a crucible which could be filled with the target isotope and heated either by electron bombardment (for the ^{10}B) or a resistance-heated tantalum crucible (for the ^{6}Li) [38]. Each substrate is held at the same distance and at normal incidence to the incoming particle stream. Since there is no guarantee that the evaporated particle cone is isotropic, during deposition each substrate is rotated about its own axis ("planetary" or "daily" rotations) as well as about the central axis ('orbital' or

'yearly' rotations). The gear ratios of the coupled rotary motions are chosen so that the orbital-to-planetary rotation fraction is 27/14. The unusual rotation periods help to prevent the development of possible coherent periodic variations in the deposit density profile due to anisotropy in the particle stream by ensuring that each substrate rarely rotates back to its starting position and orientation during the deposition procedure.

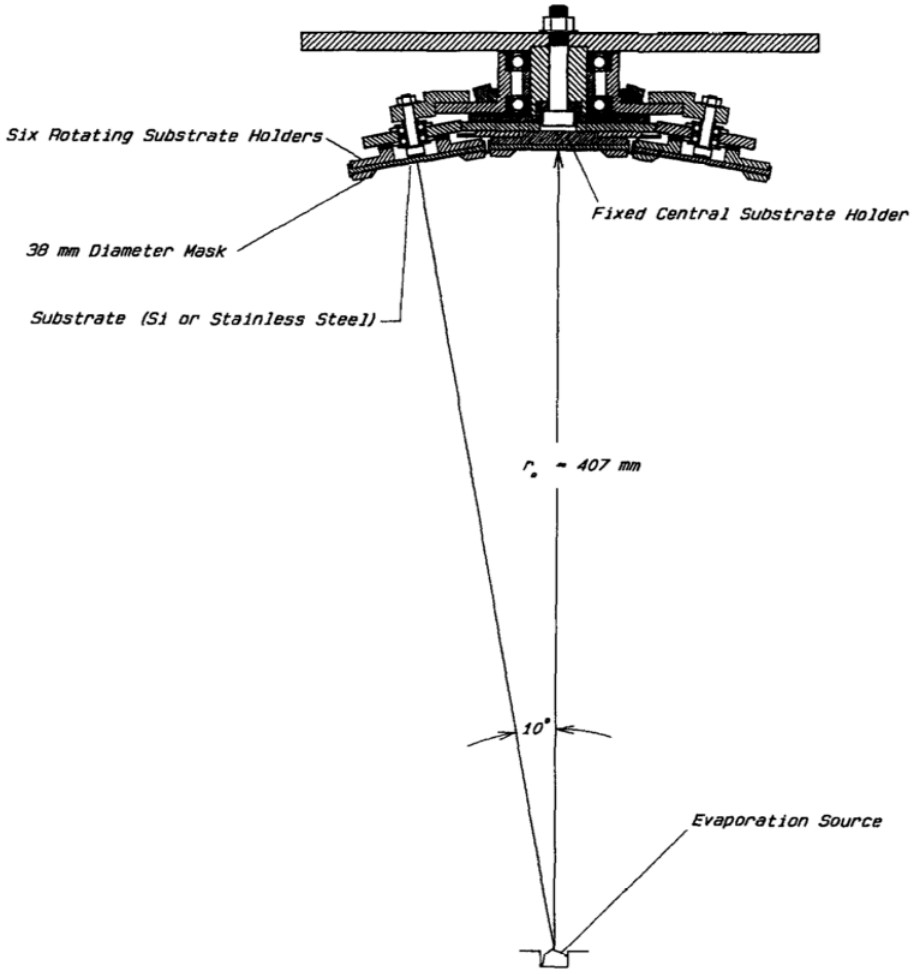

Figure 3.1: The rotating multi-substrate holder performs both planetary and orbital rotations for the six substrates held along the outside, and planetary rotation for the central substrate. The target substrate holder is at the top of the image, and the target isotope evaporation crucible is at the bottom. - Design and drawing by G.L. Greene.

Deposit thickness is determined by the particle fluence onto the substrate, which is a function of the duration of the evaporation procedure and the temperature of the crucible. The substrate holder during the original target deposit manufacturing campaign held the

orbiting substrates in the same plane as the central one (which faced normal to the particle flux). This was done to ensure that the deposits would be as flat as possible. Unfortunately this geometry introduced shadowing effects due to the mask at the deposit edges. The second campaign configuration introduced some variation in thickness over the profile, but maintains sharper deposit edges. However, inductive heating of the substrate masks reduces this sharpness for substrates of different coefficients of thermal expansion from the masks [38]. While this reduction in edge sharpness is not an issue if the neutron beam does not reach the edge of the deposit or if the edge remains sufficiently sharp, corrections must be applied to the data due to the slight parabolic shape of the profile across the surface (see Sec. 7.3.1, Sec. 7.5.1).

3.2 Isotope Dilution Mass Spectrometry

IDMS is a technique widely used to determine the quantity of a given isotope in a sample based on one or more standard reference materials(SRMs) [43]. IDMS excels at measuring the total mass of a sample in the sub-milligram regime relevant to our project. In the two-isotope version of this technique, a sample of imprecisely known isotopic composition and unknown mass is diluted with a precisely determined mass of reference material (a "spike") with a different isotopic ratio (usually chosen to be roughly the inverse of that of the sample) and the subsequent ratio of the blend is measured using a mass spectrometer. The mass measurement combined with the ratio measurements can be used to determine the atomic mass of the sample to high precision and therefore the number of nuclei of a given isotope in the sample.

In preparation for the NIST in-beam neutron lifetime experiment, IDMS was performed to determine the composition of the ^{6}Li and ^{10}B targets as part of the absolute neutron fluence determination. While Alpha-Gamma is capable of measuring the absolute efficiency

of the flux monitors independent of the target composition the IDMS measurement is an important component of one of the uncertainties and it is needed for any cross-section measurements of the target deposit material. We therefore describe the procedure in detail below.

3.2.1 IDMS technique

The IDMS measurement begins with the selection of sample materials: the unknown sample (subscript X), a dilution, or spike sample (subscript Y), and a calibration sample (subscript K). With any mass spectrometer measurement, there is an instrument-dependent correction which must be calibrated using an SRM with an atomic ratio

$$\left[\frac{N_2}{N_1}\right]_K = R'_K = KR_K \tag{3.1}$$

where R unprimed denotes the measured isotopic ratio, R' the true ratio, and N_2, N_1 the number of nuclei of the second and first isotope in the sample respectively. The correction factor K is calculated from the certified atomic ratio R'_K and Eqn. (3.1). Similarly, the isotopic ratios of the sample and spike are given by

$$\left[\frac{N_2}{N_1}\right]_X = R'_X = KR_X \tag{3.2}$$

$$\left[\frac{N_2}{N_1}\right]_Y = R'_Y = KR_Y \tag{3.3}$$

respectively where, in this case, R' is calculated using the measurement from mass spectrometry and the correction factor K. By careful analytical chemistry, the sample and spike can be dissolved and blended to form a fourth ratio:

$$\left[\frac{N_2}{N_1}\right]_B = \frac{[N_2]_X + [N_2]_Y}{[N_1]_X + [N_1]_Y} = R'_B = KR_B \tag{3.4}$$

Let the sum of the number of nucleons of both isotopes in the sample and spike be N_X, N_Y, respectively. Then,

$$\frac{N_X}{N_Y} = \frac{[N_1]_X + [N_2]_X}{[N_1]_Y + [N_2]_Y} = \frac{[N_1]_X}{[N_1]_Y} \cdot \frac{1 + KR_X}{1 + KR_Y} \tag{3.5}$$

Combining equations (3.2), (3.3), and (3.5),

$$\frac{[N_1]_X}{[N_1]_Y} = \frac{R_Y - R_B}{R_B - R_X} \tag{3.6}$$

and with (3.5), we get the defining equation of the IDMS measurement:

$$N_X = N_Y \frac{R_Y - R_B}{R_B - R_X} \cdot \frac{1 + KR_X}{1 + KR_Y} \tag{3.7}$$

Note that the determination of the number of nucleons in the sample X depends not only on the measured ratios R_X, R_Y and R_B, but also on K, which relies on the absolute accuracy of the SRM certification. Any change in the known properties of the SRM will propagate to the measurement of N_X. Similarly, any change in the purity or mass fraction of the isotope in question of N_Y will change the results of the IDMS experiment.

Target deposits used in the in-beam neutron lifetime experiment are reported in terms of their mean areal density $\bar{\rho}$ in μg. The conversion from the number of nucleons N to the mass of the isotope ^{6}Li or ^{10}B is calculated using

$$[N_2]_X = N_X f_X \tag{3.8}$$

where $f_X = \frac{R_X}{R_X+1}$. The mass of the isotope, which is used to calculate $\bar{\rho}$, is simply

$$[M_2]_X = N_X M_2 f_X \tag{3.9}$$

where M_2 is the atomic mass of the isotope in question (^{6}Li or ^{10}B in Alpha-Gamma).

3.2.2 ^{6}Li Standard Reference Materials

While the measurement of the efficiency of the flux monitor is independent of the areal mass density of ^{6}Li, and the dependent corrections are computed iteratively to reduce sensitivity, measurements of the $^6\mathrm{Li}\,(n,t)^4\,\mathrm{He}$ cross section require absolute knowledge of the areal density. The measurement of this cross section is important as it is a standard reaction used in slow neutron detection. Unfortunately, the pedigree of the ^{6}Li used to produce the deposits is somewhat confounding.

The mass of the spike (Y) can be measured to very high relative precision. Since the measurement of the isotopic ratio R_Y is dependent on K, the critical parameters are the atomic masses of the isotopes ^{6}Li and ^{7}Li, and R_K the certified isotopic ratio of the reference material K. The molar fraction of lithium in the spike may also be relevant, entering as a change in N_Y. Whether or not the molar fraction of lithium is relevant depends on the method used to determine the quantity of spike added to the sample. The atomic masses are known to high precision leaving changes in R_K as the only relevant parameter. This means that if the SRM used to measure the correction factor K is recertified with a different isotopic ratio at some later date, all measurements for which the SRM was used to measure K must be recalculated with the new certification.

The spike material used was NBS-SRM 924 (NIST SRM 924) [40], which is distinct from NIST SRM 924a. It is likely that the Li spike material cited in [44] is in error, since the isotopic ratio of IRMM-615 is very close to the expected sample ratio, which results in high error values [43]. K determination was done using IRMM 016, which is the same material as NBS-SRM 8545 [45].

NIST no longer has any NIST SRM 924. Its Certificate of Analysis states that “no actual

determination of the lithium content was made." However, since it was used as the spike solution for the certification of IRMM-615, changes in the knowledge of IRMM-615 can be used to estimate any changes to SRM 924 that should be made. It is important to note that IRMM-016 was used as the reference material K in the certification of IRMM-615 [46], which induces all of the covariances that are discussed in the previous paragraph.

At the time of preparation of the target deposits, there existed a discrepancy between the certified isotopic ratios of IRMM-016 ($n\left(^6\mathrm{Li}\right)/n\left(^7\mathrm{Li}\right) = 0.08137 \pm 0.00034$ [47]) and SRM 8545 ($n\left(^6\mathrm{Li}\right)/n\left(^7\mathrm{Li}\right) = 0.0832 \pm 0.0002$ [48]). These materials come from the same batch, so they should be identical. In order to resolve the discrepancy, Qi et al remeasured the isotopic ratio in an extended campaign which was independent of calibration SRMs [45] [49]. The calibration was instead performed by preparing 10 samples of different $R = n\left(^6\mathrm{Li}\right)/n\left(^7\mathrm{Li}\right)$ between $\sim 0.025 - 14.4$ using mixtures of highly enriched samples of ^{6}Li and ^{7}Li. The resulting absolute ratio R was 0.08212 ± 0.00028.

These 10 calibration solutions were later used in a full redetermination of the isotopic ratios and abundances of all SRMs used in the preparation of the targets, save SRM 924 [50]. Most notably, IRMM-615 did not change within uncertainty; this suggests that the measured isotopic ratio of SRM 924 was correct, since it was used in the preparation of IRMM-615.

In order to use the density of ^{6}Li on the targets in calculations of ^{6}Li neutron cross sections, the total mass of one of the surviving target deposits must be remeasured by IDMS. This is due to the dependence of the previous ρ determination on IRMM-016, whose isotopic ratio has been found discrepant since the year when targets were made. While it may seem sufficient to apply the retroactive correction, the variation in the measured quantity of ^{6}Li by IDMS makes this a less reliable solution. The measured target masses are not published.

3.3 Neutron Induced Charge Particle Counting

Prior to IDMS analysis of several of the target deposits, a quantity proportional to the areal density must be measured for all targets in order to infer the areal density of the remaining targets [41] [42]. Each target was placed in a target holder with 5 symmetrically-oriented detectors and a highly reproducible target mounting location (similar to the Flux Monitor). The target holder was operated at the Belgian Nuclear Research Centre on reactor BR1. Two types of proportional beam monitors measured the flux: a ^{235}U fission chamber, and a ^{10}B proportional gas chamber. By measuring the reaction rate with respect to the beam monitors for all of the targets (^{6}Li and ^{10}B separately), the relative areal density of each target can be determined.

Target profile uniformity is measured using interferometry. Accurate dimensional characterization is performed via traveling microscope and Talistep measurements [38]. With these measurements and the relative reaction rates determined by neutron induced charged particle counting, the total mass of one of the deposits can be assayed by IDMS to determine the areal density of the others.

3.4 Thick $^{10}B_4C$ Target Characteristics

The thick targets are self-supporting targets of boron carbide $^{10}B_4C$ at 90% enrichment. Two targets of different thicknesses exist: a ∼0.56 mm "thicker" thick target, and a ∼0.31 mm "thinner" thick target. The diameter of these targets is larger than the thin target substrates. They require a different backing bracket to use in Alpha-Gamma, but since they are nominally flat and totally absorbing they do not require precise positioning the way the thin targets do. Both targets are sufficiently thick to attenuate a beam of cold neutrons to $< 0.0001\%$.

Chapter 4

The Alpha-Gamma Apparatus

The Alpha-Gamma apparatus has been used on a monochromatic neutron beam to successfully remeasure the efficiency of the neutron flux monitor to be used in the NIST in-beam neutron lifetime measurement now in progress. We conducted this measurement to higher precision than the result previously reported by Yue [51]. The uncertainty of our new measurement is low enough that the absolute accuracy of the new Penning trap in-beam neutron lifetime experiment can approach 0.1% with sufficient counting statistics and evaluation of systematic errors associated with proton counting and detection.. The success of this calibration also enables future applications to precise absolute neutron flux and cross section measurements as Alpha-Gamma's capabilities are further developed.

4.1 Alpha-Gamma Hardware and Design

The Alpha-Gamma apparatus consists of a pair of HPGe γ detectors, an ion implanted silicon charged particle (or simply α) detector (passivated implanted planar silicon (PIPS)® by Canberra or Ultra by Ortec), and an interchangeable ^{10}B target. Both the ^{10}B target and the α detector are contained within a chamber which shares a vacuum with the flux monitor during its calibration. Two ^{10}B targets are used during each three phase measurement of the absolute flux: a thick $^{10}B_4C$ disk, and a thin film of ^{10}B deposited on a single-crystal silicon wafer. A kinematic mounting system enforces repeatable positioning with respect to

the neutron beam.

The detector arrangement is chosen to minimize contributions to systematic corrections and uncertainty. In a 3-dimensional coordinate system where the (0,0,1) vector points towards the beam source, (0,1,0) points away from the direction of gravity, and (0,0,1) is chosen such that the coordinate system remains right-handed (this happens to be away from the kinematic mounting system vacuum flange), the alpha detector is positioned along the (1,-1,1) vector and the gamma detectors are axial along (0,1,0) and (0,-1,0) (Fig. 4.1). The target deposit is positioned to face normal to the alpha detector in order to minimize

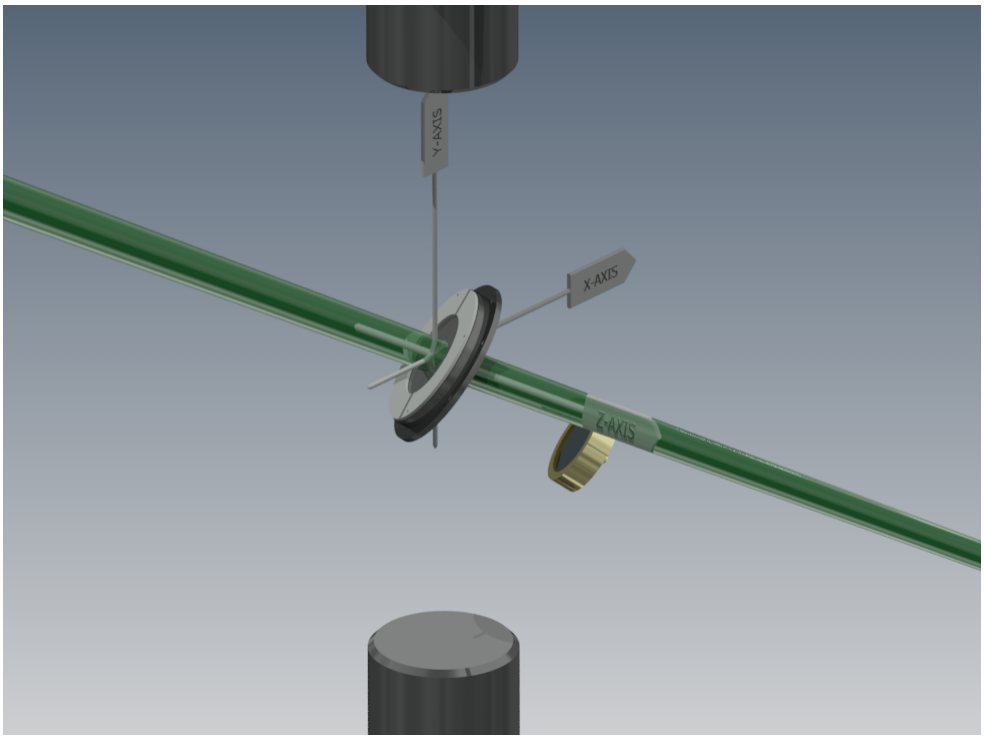

Figure 4.1: Coordinate axis for the Alpha-Gamma apparatus showing the relative positions of the alpha detector and both gamma detectors to the target holder. The Z-Axis points upstream along the neutron beam.

attenuation of the charged particle signal from neutron interaction with ^{10}B. Since 478 keV gammas are not significantly attenuated by the materials present in the experiment, there is less concern with the specific orientation of the samples; a measurable correction is sufficient to account for the presence of the silicon substrate or the bulk of $^{10}B_4C$.

It is important that the position of the detectors with respect to the target does not change over the course of a measurement during which the different boron targets must be physically exchanged. Several components of the target mounting apparatus work in concert to achieve the necessary reproducibility. The target holder is assembled in two parts (Fig. 4.2). The first component, the target backing bracket, is either one of several thin stainless steel disks with a 0.254 mm deep groove whose radius is sized to admit either the ^{10}B or ^{239}(Pu) targets which are 50.8mm in diameter, or the thick $^{10}B_4C$ target both of which are 55.25 mm in diameter. In both cases, the depth of the groove is shallower than the target. This forces the contacting surface (the polished side of the silicon wafer substrate, or the smooth face of the $^{10}B_4C$) to maintain the same orientation when pressed against the polished steel of the second component, the target mount. A set of four socket cap screws, each with four Belleville washers (conical spring washers), maintain roughly equal pressure between the target and the two components in order to distribute the force equally and limit bowing. This is achieved by tightening the screws only as much as is necessary for the target to remain fixed against the target mount. The target mount is a single piece of stainless steel machined with a conical groove 32° in from the surface on the upstream side to admit the neutron beam while tilted at its angle of operation. It is fixed to an aluminum mounting arm using four #8-32 ANSI standard socket cap screws that are 9/32" long.

The second major contributor to the position reproducibility comes from the kinematic mounting vacuum flange upon which the aforementioned aluminum mounting arm is attached (Fig. 4.3). The kinematic mounting flange is an 8" vacuum flange which seals with an o-ring cut to a custom diameter. Four bolts are loosely fixed such that the vacuum pressure, rather than the bolts, seals the flange to the rest of the vacuum system. Three grooves evenly spaced around the edge of the flange. Fixed into each groove is a pair of

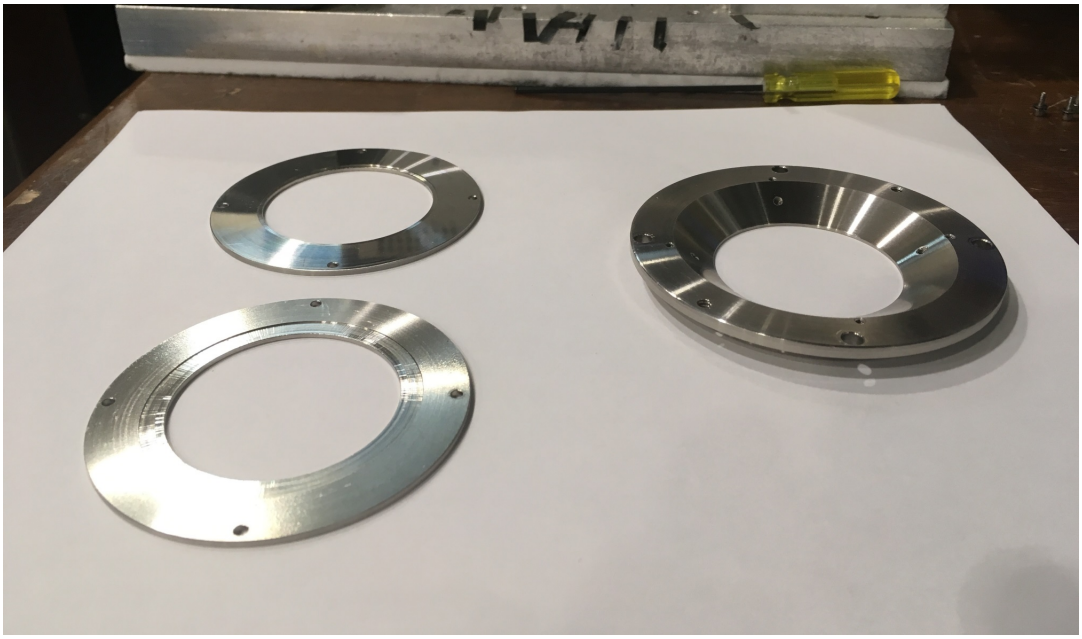

Figure 4.2: The target holder and its component parts. Left: the target backing brackets. Different groove diameters accommodate either the thick target (wider), or the silicon-backed ^{10}Bor ^{239}Pu deposits (narrower). Right: The stainless steel target mount. Targets are mounted facing away from the page.

hardened steel rods. When the flange is under force, either from the pressure difference between atmosphere and the vacuum or from the operator, the tooling rods mate against three evenly-spaced hardened stainless steel balls which are attached to the Alpha-Gamma vacuum chamber. Each stainless steel ball mates against two tooling rods. These six points of contact are sufficient to kinematically constrain the position of the flange in much the same way that traditional cone, V, and flat kinematic mount components would. The cross-sectional width of the custom o-ring is chosen such that the flange seals correctly while properly mating to the kinematic features. A thicker width o-ring would prevent the steel bearings from mounting correctly.

The stability and reproducibility of this setup was tested in two ways. A wire is wound around the small bolts of the target holder to form a set of cross-hairs which cross at the center of the surface of the target (care must be taken to wrap it along the correct path around each bolt, or the crossing point will be off-center). Replacing the flanges at

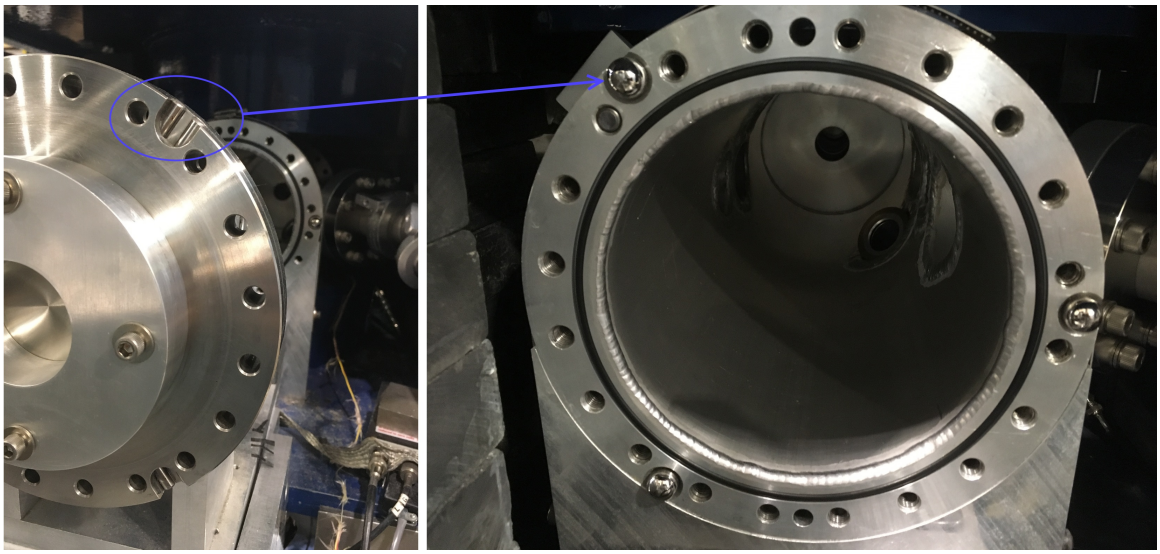

Figure 4.3: Left: The recessions and the hardened steel kinematic mounts are seen around the circumference of the flange. The target mounting flange is facing away from the apparatus in order to display both mating surfaces simultaneously. Right: The hardened steel spheres which mate against the kinematic mounts are visible. The indicated region in blue shows the kinematic mount and its paired steel ball.

either end of the vacuum system along the beam with viewing vacuum flanges, a theodolite was used to measure the position of the cross-hairs. It is not strictly necessary that the cross-hairs be centered with respect to the beam during this step, and the coincidence of the center point with the beam will be tested later in two separate ways. The vacuum system is then repeatedly vented and evacuated in order to measure any movement with respect to the cross-hairs' initial position. By reporting the distance (2.5m) and measured angle from the theodolite to the cross-hairs over several oscillations, it was determined that the center position of the target surface only varied by about 10μm. We also check the reproducibility of the geometry using the ^{239}Pu data; this technique has the simultaneous advantage of testing the stability of the alpha detector (with the caveat that it cannot distinguish between instability in either device).

Along the (1,-1,1) direction is a Microdot (#10-32 connector) electronics vacuum feedthrough into which the alpha detector is mounted. A precision aluminum aperture with a diameter of $D_{AG} = (27.598 \pm 0.006)$ mm is affixed to the detector in order to define its solid angle

for charged particles such that all particles will fall within the detector's active area; it also strictly defines that area. The detector itself is a 900 mm^2 passivated silicon charged particle detector manufactured by either Ortec or Canberra (both have been used) with a resolution of 33 or 27 keV FWHM, respectively. A bias voltage of 75V is applied to achieve sufficient resolution for the α-detector in the Alpha-Gamma apparatus.

Two Ortec liquid nitrogen cooled high-purity germanium γ-detectors are located on opposite sides of the deposit along the (0,1,0) axis. Since the detection efficiency of the γ-detectors for the 478-keV gamma rays from the ^{10}B(n, α)^{7}Li reaction is measured using the α-detector, there is no special collimation necessary to constrain the allowed trajectories. Each detector houses a unique crystal which operates best at a factory-determined bias voltage (in this case, that is 3300 kV for the top detector, 4000 kV for the bottom detector). Application of the bias voltage increases the thickness of the electron depletion layer in the crystal which inhibits the likelihood of any thermal noise to push a charge carrier in to the conduction band. Cooling with liquid nitrogen suppresses thermal noise by effectively increasing the width of the band-gap; this reduces both the leakage current, which protects against voltage breakdown, and the background rate [52].

An Ortec 785 Auto Fill Controller refills both HPGe detectors with liquid nitrogen at regular intervals which can be changed by the operator. The HPGe detectors' liquid nitrogen dewar vacuum jacket and the Ge crystal volume share a common vacuum. If either the liquid nitrogen hold time begins to wane, or the signal from the HPGe crystal shows the effects of vacuum degradation, both volumes must be pumped and carefully baked at no more than the factory recommended 58 °C (137 °F). Sufficient common vacuum is achieved at approx. 2e-5 torr at a reasonable bake, resulting in a hold time of 13 h.

The neutron beam is stopped by a beam dump immediately downstream of Alpha-Gamma. An initial layer of enriched ^{6}LiF plastic is used in order to keep the gamma

background from the beam dump the same between the beam-on and beam-off states. A layer of Boraflex absorbs any neutrons which happen to pass through the 2mm thick ^{6}Li plastic (<0.3% of incident neutrons). Stainless steel plate 12.7 mm thick followed by several cm of polyethylene moderate any fast neutrons (there should be very few), which are finally absorbed by a second sheet of Boraflex.

Any gammas incident from outside of the apparatus, either from the beam dump or from other locations, are attenuated by lead bricks stacked behind a sandwich of steel plate around Boraflex (Fig. 4.4). Since the HPGe detectors are most sensitive to this background, there is an annulus providing 10 cm of lead shielding surrounding the detection region. This annulus extends $\sim$ 95 mm above and below the SS plates which support each detector. The experiment is most sensitive to incident gammas depositing energy inside of the energy range corresponding to the 478 keV gamma from neutron capture on ^{10}B. While the lead is more than sufficient for attenuating gammas of that energy, incident higher-energy gammas can deposit only part of their energy in the crystal via Compton scattering, necessitating as much shielding as possible for a precision experiment such as Alpha Gamma. A copper sheath lining the innermost section of the annulus shields the HPGe detectors from low-energy gammas emitted from the lead itself. Finally, additional pieces of Boraflex laid across the top and inside of the structure absorb neutrons from any direction of incidence besides below the experiment. Though these latter absorptions produce the same gamma rays upon which the experiment relies, the substantial amount of lead shielding makes this a non-issue.

Upstream of the Alpha Gamma device resides the Flux Monitor FM (also called the Fluence Monitor, or $1/v$ device in other texts) which is calibrated for use in other experiments such as the NIST in-beam neutron lifetime experiment. During operation, both devices share a common vacuum and are connected via a flexible bellows (for alignment),

Figure 4.4: Alpha-Gamma shielding. Seen are a steel-Boraflex-steel neutron absorber and a stack of lead bricks. Together, these attenuate the background rate from external neutrons and gamma rays.

and a ceramic voltage isolation flange (for electronic noise suppression). Within are four Si charged particle detectors which are biased at 50V. Stainless steel masks define the solid angle presented to a wafer holder which holds one of several target deposits (Fig. 4.5). Touch metrology was performed to determine the precise solid angle presented to the detectors by the wafer-holder center. Subsequent ^{239}Pu measurements support this determination.

The FM stand supports not just the FM, but also the wavelength measurement equipment, half of the beam flight tube alignment apparatus, and the lithium flag (which is used to modulate the beam-on/off status during data taking). The FM support is a pair of aluminum C-shaped supports called the "collar" or "yoke" which nest with the 13.25" ConFlat (CF) flanges that make up the FM vacuum chamber. Band straps provide stability of the FM, while tape along the inside contact surface allows some amount of position reproducibility and electrical isolation. This is discussed in more detail in Sec. 5.1. The

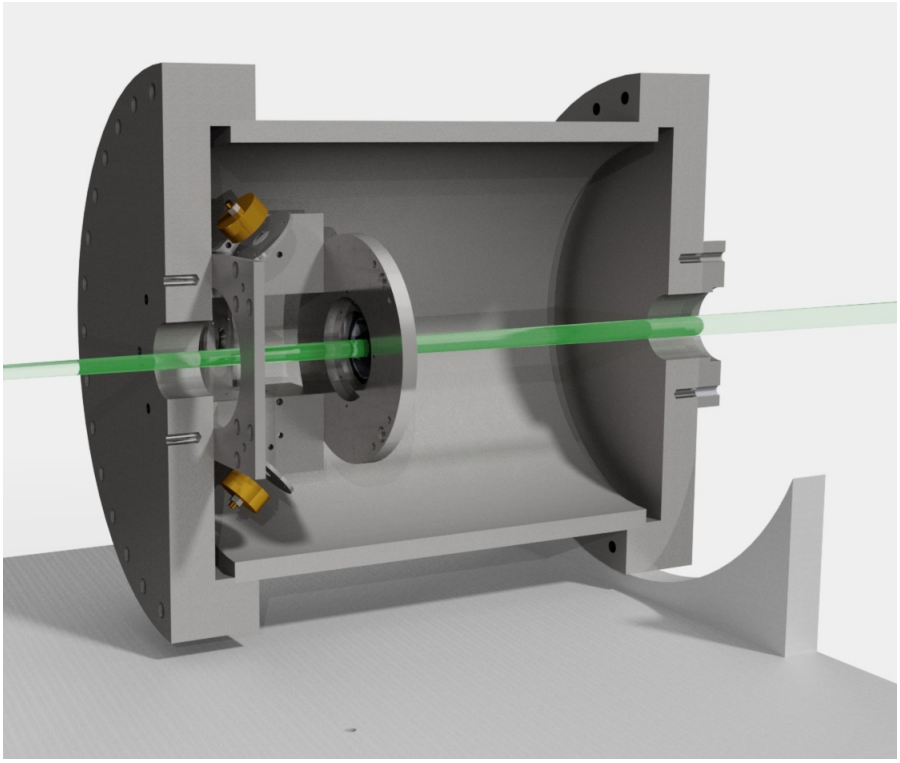

Figure 4.5: The Flux Monitor is calibrated for use in various absolute neutron flux-dependent experiments. Visible are several detectors and the target deposit. Together they measure the absolute flux of neutrons to sub-0.1% precision.

lithium flag is attached to a worm screw which communicates with the DAQ via an RS-232 interface Input Gate / Output Register (IGOR) module (see Chapter 6). The neutron beam flight tube is supported by a V-block whose position can be adjusted in the vertical and horizontal directions using a pair of micrometers. The wavelength measurement apparatus will be discussed in detail in Sec. 4.2. FM alignment is discussed in Chapter 5.

Two components are supported on an 80/20® aluminum frame (Fig. 4.6) close to the NG-6 neutron shield wall and NG-6m beam shutter: the upstream-side of the helium-filled aluminum flight tube, and the beryllium filter cryostat. The flight tube conducts the NG-6m neutron beam to the apparatus with minimal scattering. Any scattered neutrons are absorbed by a Boraflex sheath to maintain a low neutron background. Helium gas flows through the tube at a constant, low rate to keep air out of the neutron beam flight path

and ensure the (lower) attenuation of the neutron intensity from scattering on helium is constant during measurements. A ^{235}U fission chamber acts as a beam monitor between the flight tube and the filter cryostat. The cryostat itself sets closest to the NG-6 shield wall and beam shutter. Since liquid nitrogen cooled polycrystalline beryllium filters out the $\lambda/2$ component of the beam diffracted by the pyrolytic graphite monochromator by scattering out the shorter wavelength neutrons [53], ample Boraflex shielding is necessary to lower neutron backgrounds. More detail is given below in Sec. 4.2.

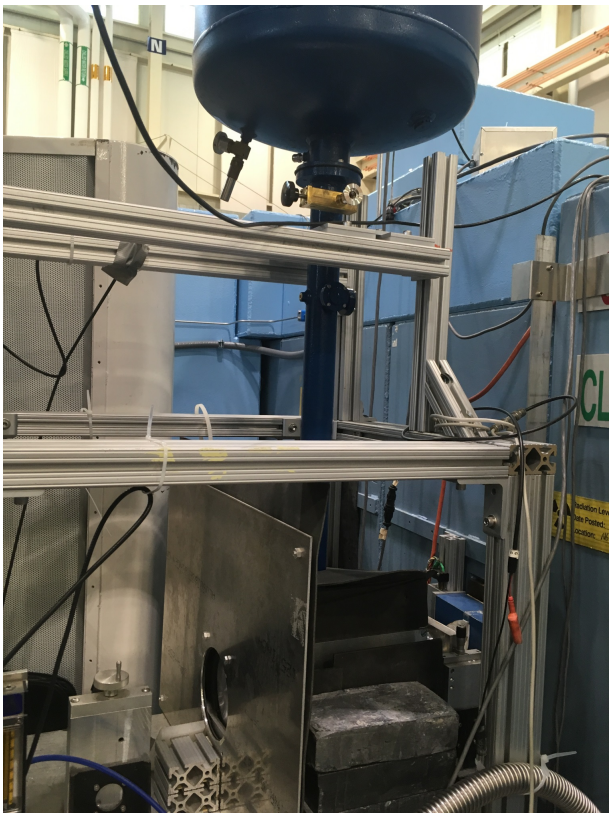

Figure 4.6: The NG-6m beryllium filter cryostat and neutron beam waveguide deliver a monochromatic (.496 nm wavelength) neutron beam to the Alpha Gamma experiment. Boraflex and stacked lead shielding around the cryostat absorbs scattered neutrons and subsequent absorption gammas. This helps to control background.

4.2 The NG-6m Beamline

The NCNR houses a 20 MW research reactor serving 19 separate neutron beamlines at thermal and cold energies. Beamlines are split using reflectometry or Bragg diffraction off of crystal monochromators to create more than 25 instrument stations which are used to conduct experiments using neutron scattering, activation analysis, imaging, interferometry, and fundamental physics with neutrons. The NG-6m beamline at NCNR is a monochromatic neutron beamline of wavelength $\lambda = 0.496$ nm. A monochromatic beam allows us to measure the absolute efficiency at a single neutron energy and extrapolate to other beam energies. Beamline NG-6m is created by Bragg diffraction off of the (0002) plane of a pyrolytic graphite crystal. Pyrolytic graphite has slightly irregular alignment between the graphite crystallites which allows for broader wavelength acceptance for Bragg reflection and minimizes extinction effects. The degree of desired acceptance is an optimization between beam intensity and monochromaticity.

Both $\lambda = 0.496$ nm and $\lambda/2 = 0.248$ nm neutrons satisfy the Bragg condition from the (0002) lattice planes ($n\lambda = 2d\sin\theta$, where $d = 0.6708/2$ nm and $\theta = 47.72°$). The $\lambda/2$ component is undesirable due to the difference in neutron cross section σ between the two wavelengths, and the greater intensity of the λ component in the main beamline NG-6. The LN_2 cooled beryllium polycrystal filter suppresses the $\lambda/2$ component by preferentially scattering it out of the beam (see Fig. 4.8). This occurs because neutrons with energies above the Bragg cut-off (BCO in the figure) have a wavelength that satisfies the Bragg condition for some beryllium crystal orientation and the polycrystalline nature of the beryllium filter ensures that many such regions exist along any neutron trajectory. Even though the $\lambda/2$ component in the beam is suppressed, it is necessary to precisely measure the relative intensities of the two components. Phonon-induced neutron scattering is suppressed by cooling. This serves to increase the transmission of the λ component of the beam.

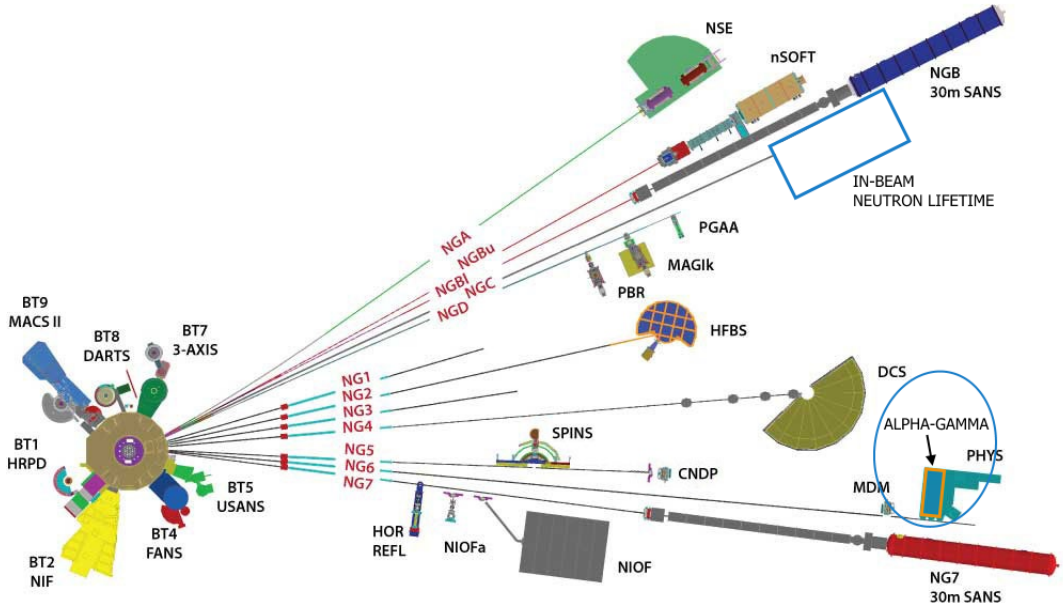

Figure 4.7: The layout of the two wings of the neutron guidehall at NCNR in 2015. Since then a new Small Angle Neutron Scattering (SANS) instrument is being developed on NG-3, and the Cold Neutron Imaging Station has been installed at the end of NG-6. NG-6m and NG-6u are monochromatic beamlines split off from the main beam by reflection from pyrolytic graphite.

4.2.1 Wavelength Measurement

Systematic corrections require precise measurement of the neutron wavelength. This is done by Bragg reflection off of an analyzer crystal. Our experiment uses Bragg diffraction off of the (1,1,1) plane of a flat, 4 mm thick rectangular piece perfect crystal silicon. By measuring the reflected neutron intensity as a function of the angle of incidence, the neutron wavelength can be determined. T-slotted 80/20 aluminum extrusions provide structural support for the measurement components Fig. 4.9. The analyzer crystal is held in an aluminum frame with felt padding to prevent damage. The frame is attached to a Kohzu SH03B-DM tilt stage. The tilt stage is necessary to ensure that the crystal lattice planes are normal to the beam at 0 rotation and not at some angle above or below. Attached to the tilt stage is a Faulhaber AM1524 miniature stepping motor with a 900:1 reduction gearhead. The relative position of the tilt stage is determined by counting stepper motor steps. Although the small stepper

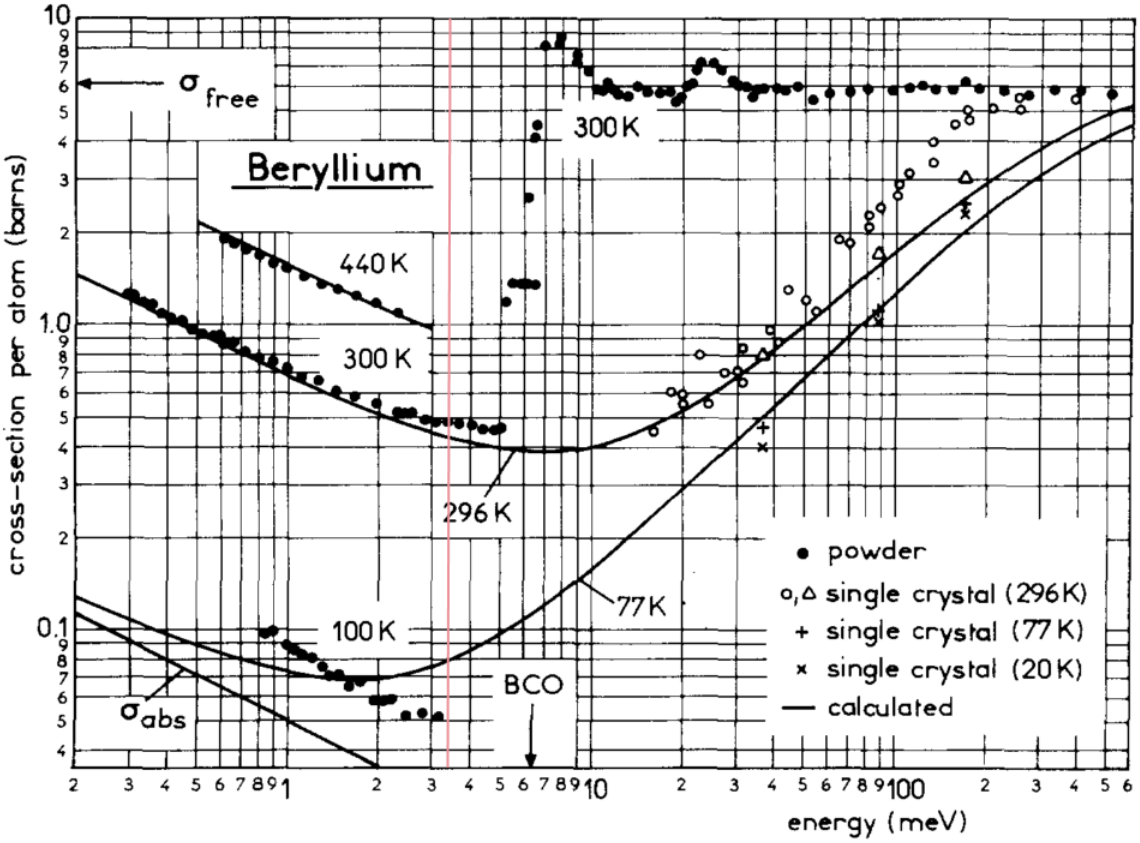

Figure 4.8: The total neutron cross section for beryllium as a polycrystal (powder), and as a single crystal at various temperatures as a function of energy [53]. The NG-6m beam energy is indicated as the pink vertical line at 3.3 meV. Note that suppression of the $\lambda/2$ component still occurs at room temperature, but the relative difference between the desired λ component and the $\lambda/2$ component will decrease. - This image borrowed from the referenced paper by Freund

motor may miss steps, the large reduction in gearing ratio greatly reduces the uncertainty introduced by this effect. The tilt stage is attached to a shaft which runs through the center of a Huber 408 rotation stage and into a Heidenhain RON 275 angle encoder. The shared drive shaft ensures that the encoder reads the same rotation produced by the rotation stage. A housing mounts to the encoder and the rotation stage, and a 2-axis tilt stage is attached between the housing and the T-slotted structure. The 2-axis tilt stage is necessary for ensuring that the drive shaft is perpendicular to the neutron beam. If it is not, rotations of the analyzer crystal using the drive shaft change the orientation of the crystal such that

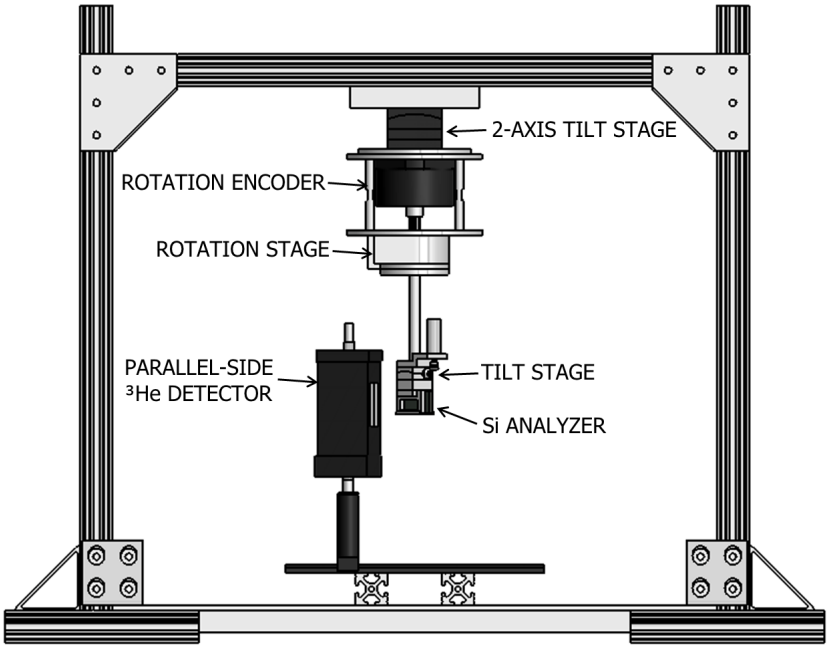

Figure 4.9: The wavelength measurement apparatus ([51]) including tilt and rotation stages, encoder, neutron detector, and silicon analyzer crystal. The analyzer crystal reflects the λ component of the monochromatic neutron beam at only two angles. By rotating it through these angles, the wavelength can be measured.

the beam is not reflected in the horizontal plane.

Neutrons are detected in a square profile ^{3}He proportional counter. Unpolarized ^{3}He has a large thermal neutron cross section. When a neutron is absorbed, a proton and a tritium nucleus are emitted with 0.764 MeV of energy, which ionizes the surrounding gas. The induced charge can be measured by applying a voltage. The signal is proportional to the incident flux. A ^{3}He counter is placed at the approximate location of the transmitted beam in Laue geometry. Since the neutron beam is not perfectly monochromatic, rotation of the analyzer crystal produces an intensity rocking curve in the ^{3}He detector with respect to angle instead of a delta function. The square profile of the detector ensures that the full intensity of the reflected beam is detected with the same efficiency. A rocking curve can then be recorded which relates the angle of incidence to the angle of reflection.

Alignment is performed using an aluminum block 64 mm $\times$ 27 mm *times* 4 mm thick. A 1 mm diameter conical bore at nearly the 3D center of the block (it is $\sim$ 13.15 mm

from the base rather than 13.5) enables alignment to the beam with a theodolite. When the bore remains centered under all rotation and tilt angles, the crystal center is aligned with both the beamline and the drive shaft center. The alignment is further tuned by measurement with the neutron beam. Both the parallel and antiparallel reflections are measured to determine at what encoder angle beam normal is (see). If the analyzer crystal is tilted up or down with respect to the beam, rotations project the beam into a different region of phase space. While the relative angle between the incident and diffracted beams will still be the same, the measured rotation angle necessary to achieve Bragg diffraction in the parallel and antiparallel direction will be greater (see Fig. 4.11). By minimizing the difference in measured angle between the parallel and antiparallel diffraction beams, we find the tilt angle necessary for the incident beam to be normal to the diffraction planes (see Fig. 4.12)

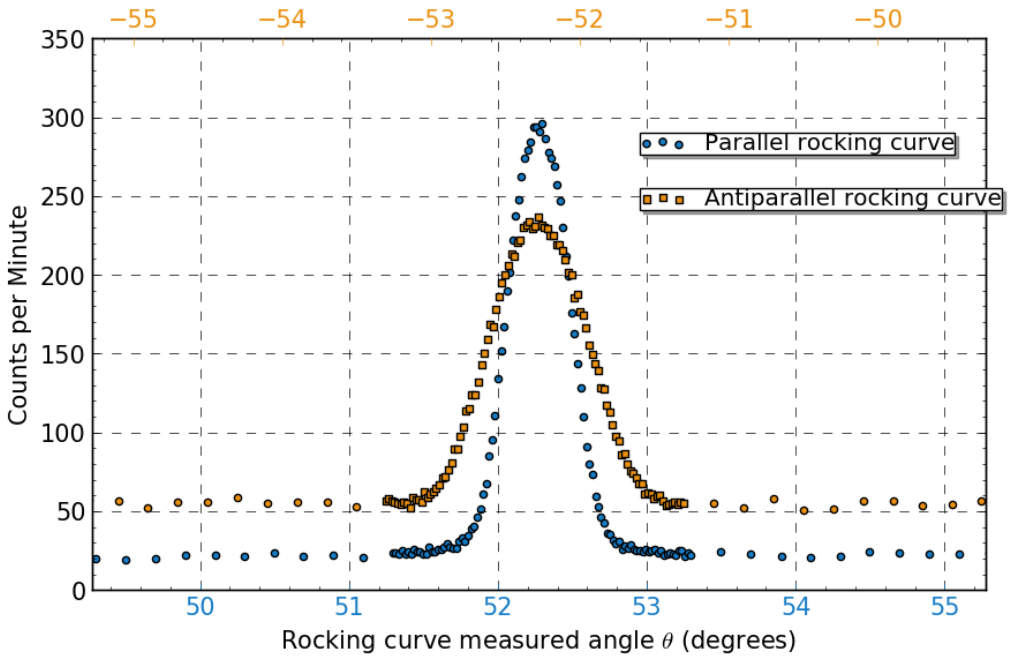

Figure 4.10: Counts per minute in the ^{3}He detector as a function of rocking curve angle for a typical measurement.

The wavelength is measured at the correct tilt angle determined earlier. It is the same

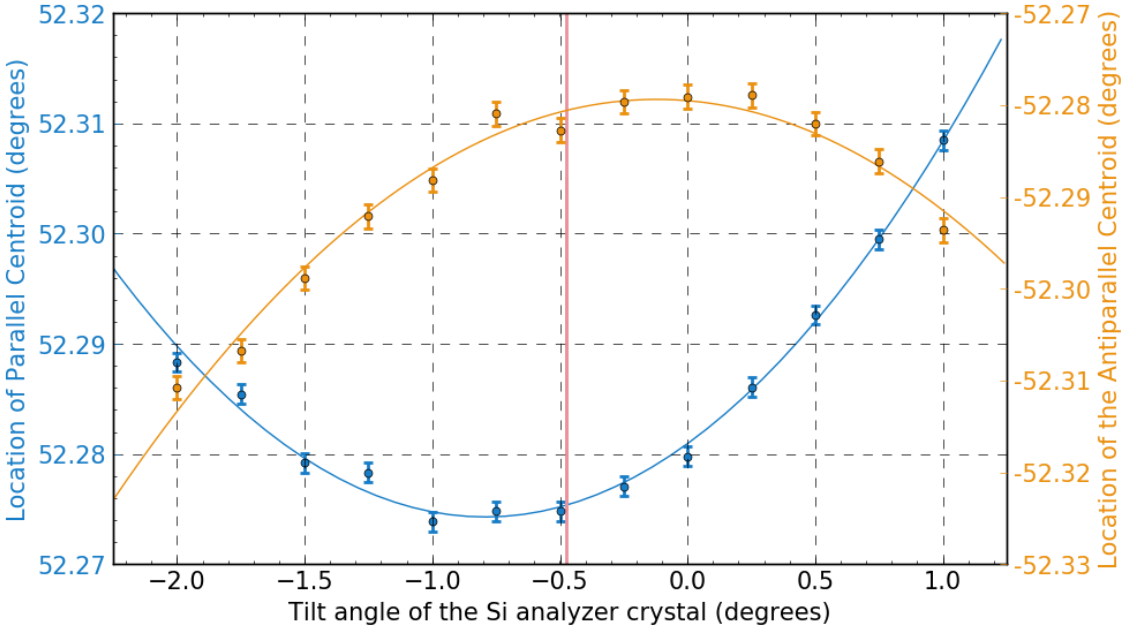

Figure 4.11: The centroid of counts per analyzer crystal rotation angle is plotted versus the analyzer crystal tilt angle. The pink line is the point at which the difference between the measured angles of the two beams is minimized.

centroid measurement used to find the proper tilt curve. There is additional broadening of the measured peak in the antiparallel beam. The Bragg angle θ_{Br} is found using both the parallel and antiparallel diffraction peaks. The measured angle should be the same. The average between the two is taken for many data sets in order to determine the wavelength. Since the calculation of the wavelength using the Bragg condition is nonlinear in θ_{Br} in our region of interest, the uncertainty should be calculated using the extreme values of $\theta_{Br} \pm \delta\theta_{Br}$. Inclusion of all measurements of the NG-6m wavelength dating back to 2009 yields $\theta_{Br} = 52.279 \pm 0.018°$, and $\lambda_{NG-6m} = 0.49605 \pm 0.00012$ nm. The uncertainty in this case is chosen to include measurements between June 2009 and Feb 2010 (of which there are four) which deviate significantly from the rest of the data. The most recent measurement has uncertainty typical of the technique: $\theta_{Br,\text{latest}} = 52.277 \pm 0.0002°$. If additional measurements can confirm that the wavelength shows no excursions, it is reasonable to conclude

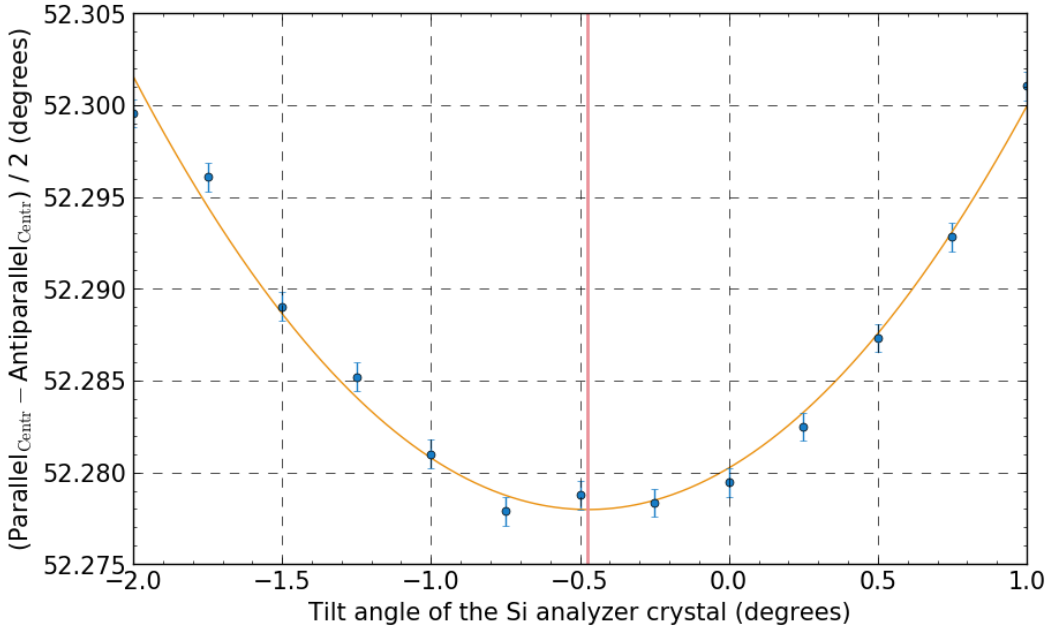

Figure 4.12: The difference in measured rotation angle of the centroid at various tilt curves. The pink line is the minimum, and at the same point as the pink line in Fig. 4.11.

that the 2009-2010 excursion is anomalous and can be discarded, reducing the uncertainty.

The presence of any neutrons with wavelength $\lambda/2 = \lambda\frac{1}{2}$ in the filtered beam is measured as a fraction of the λ component of the beam. Since the $\lambda\frac{1}{2}$ component of the filtered beam is very small with respect to background, the correct Bragg angle is found using the unfiltered beam (see Fig. 4.13). The contribution to the beam for each component is taken as the full integral under a fit to the rocking curves. The fractional contribution of the $\lambda\frac{1}{2}$ component is given as $\lambda\frac{1}{2}/\lambda = 0.0008 \pm 0.0001$. The correction due to this contribution is described in Sec. 7.5.3.

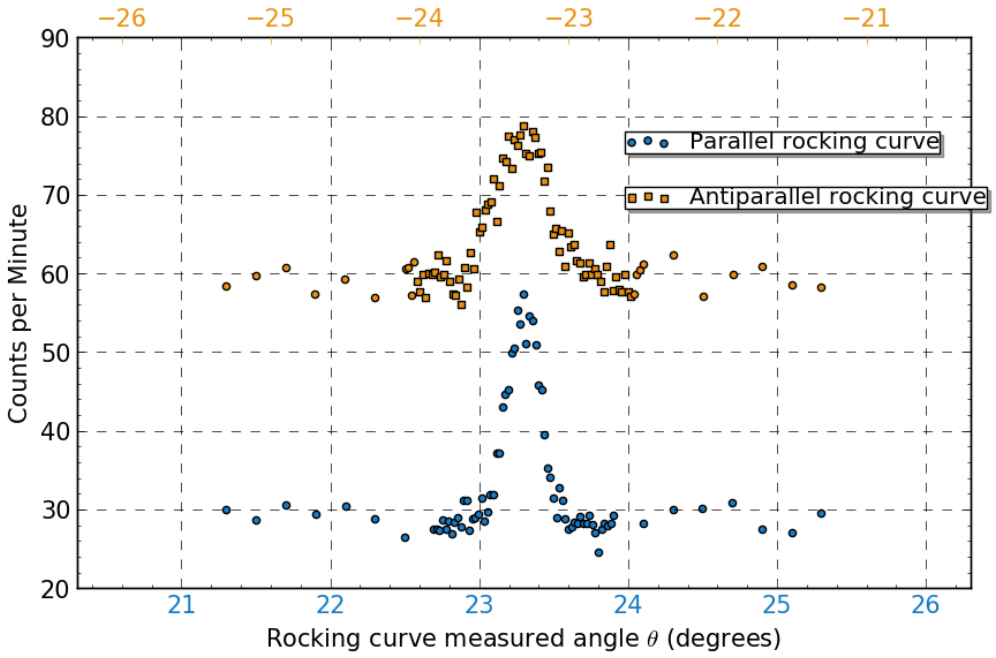

Figure 4.13: A rocking curve measurement of the $\lambda/2$ component in the unfiltered beam. The data presented are before background subtraction.

4.3 Electronics and Data Acquisition

Both the PIPS and HPGe detectors are solid-state devices which produce a characteristic output upon particle interaction. The detection volume is electrically a diode. Under voltage bias, very little current flows through the junction until it is struck with a particle. At that point the deposited energy raises electrons to the conduction band, allowing an amount of current to flow proportional to the incident particle energy. A preamplifier for each detector prepares the signal for a shaping amplifier which outputs a Gaussian pulse suitable for pulse-height determination by single channel analyzers (SCAs). The signal can be sampled by a multi-channel analyzer (MCA) (in this case, a Tracor Northern TN-7200) at the shaping amplifier without loss of signal. TTL pulses from the SCAs are counted in a set of Kinetic Systems CAMAC hex counters. Counts per data cycle are collected on the DAQ computer via a GPIB interface.

The BNC output for the AG alpha, the FMA alpha, and the bottom gamma detector

preamp signals are divided at the SCA inputs in order to integrate a secondary set of detection electronics, a PXIe multichannel analyzer unit manufactured by National Instruments. The PXIe provides diagnostic information much like the Tracor-Northern MCA but with much finer binning as well as individual spectra of each 20-minute data cycle. However, the difficult-to-quantify signal timing in an event-driven programming language like Labview makes it inappropriate for an absolute rate measurement as needed for the FM efficiency calibration.

4.3.1 Charged Particle Signal Detection

The Alpha-Gamma PIPS and the FM PIPS detectors operate the same way and are connected to the same electronics modules. Bias voltage for all 5 detectors is supplied by an ISEG NHS 6210p precision high voltage 6-channel power supply. It is set to 75 V for the Alpha-Gamma alpha detector and 50 V for the FM detectors. Noise fluctuations in the supplied voltage are rated at < 5 V. Leakage currents are typically $\sim 100\mu$A for the AG detector, and $\sim 150\mu$A for the FM detectors at 21 °C. These leakage currents increase by nearly a factor of 2 under a temperature change of only 5 °C. Incident particles deposit energy and cause a sharp ($\sim$50 ns) voltage spike which decays exponentially with a proportionally long tail forming a so-called "tail pulse" (see Fig. 4.14). A Canberra 2006 preamplifier prepares and drives the signal to a Tennelec TC241 shaping amplifier. Another particle arrival will cause a second, additive jump in voltage. The shaping amplifier therefore measures the change in voltage during the $\sim$ 50 ns rise to produce a 2.2 μs FWHM Gaussian pulse with a characteristic voltage height.

The range of output voltages runs from 0 to 10 V, but is typically about 1 V for the neutron reaction products. An Ortec 550 Single Channel Analyzer (SCA) set to Normal mode determines whether the voltage of the incident Gaussian pulse crosses a set of dis-

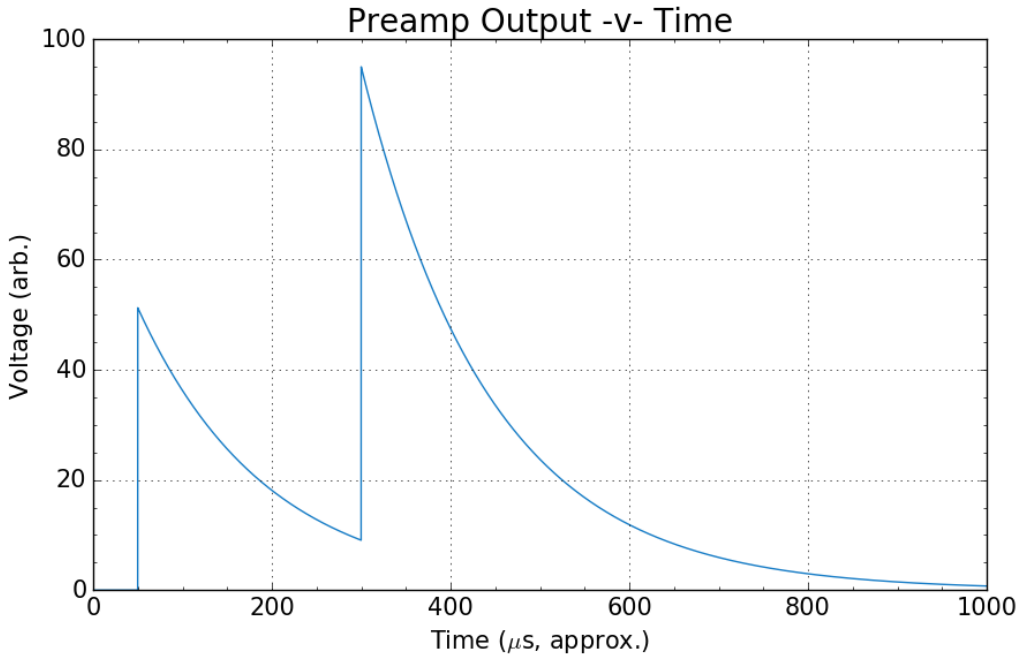

Figure 4.14: A cartoon example of incident charged particle signals from the preamp. Note the decay time can be much longer than the time between particle arrivals

criminators and outputs a 500 ns wide TTL logic pulse (see Fig. 4.15). The Lower Level (LL) discriminator is set slightly below the voltage produced for the relevant particles. The Upper Level (UL) discriminator is set between the α and triton energy levels in the FM. For the Alpha-Gamma device, since there is no beam-dependent noise nor interesting signals (excepting that a pulser measurement is not being performed), the UL is set sufficiently high to collect pileup pulses in addition to the singles pulses. Background measurement with the beam blocked by the lithium flag (called "beam-off") is sufficient to cancel any background counts in this regime.

The count rate measured (r) in the region of interest (between the LL and UL) is then determined by subtraction of the count rate in the UL from the count rate in the LL divided by the total time (t) over which the measurement was taken:

$$r = \left(d_{LL} - d_{UL}\right)/t \tag{4.1}$$

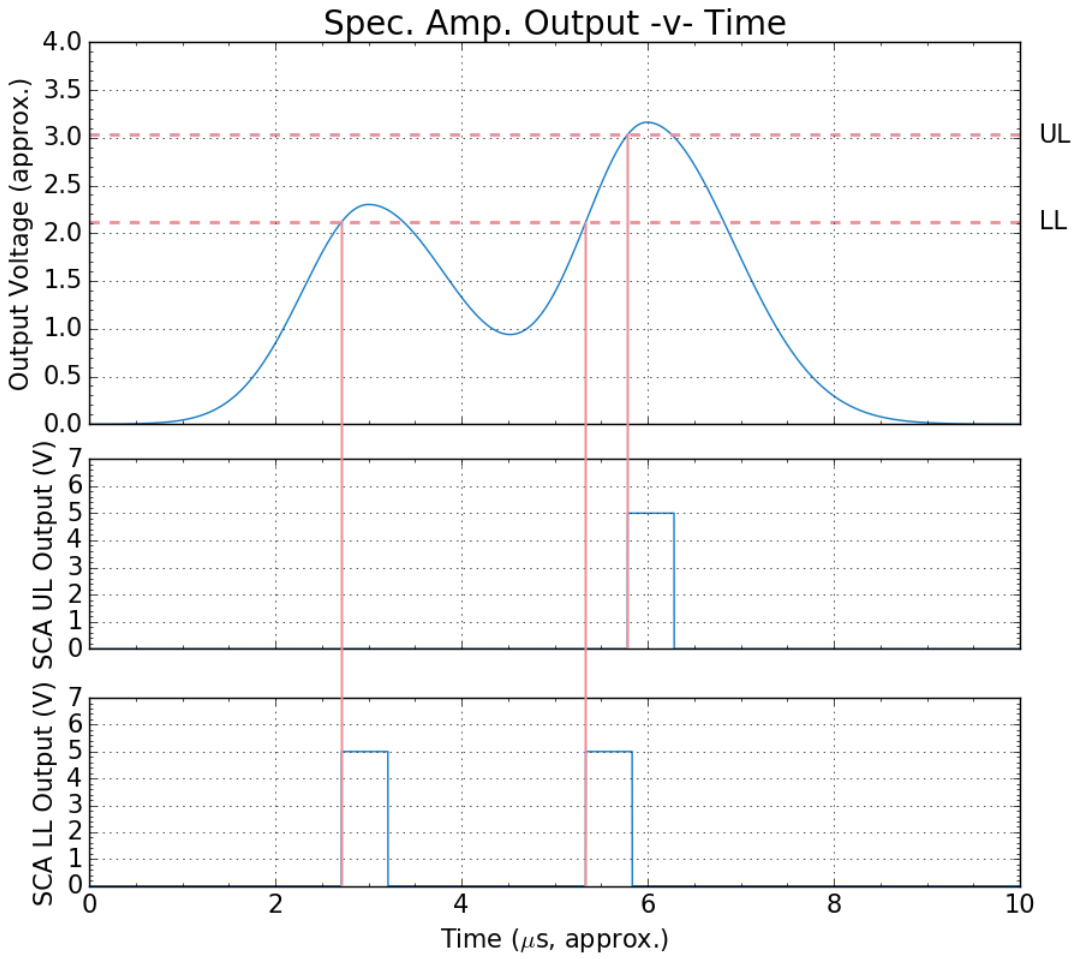

Figure 4.15: A descriptive example of how the LL and UL discriminators operate. Contrary to appearances, incoming particles with very little time separation rarely prevent the output signal voltage from dropping below the LL discriminator.

The signal from each PIPS detector in the FM is sent to two SCAs for a total of 4 levels of voltage discrimination per detector. Beam-off measurements and sufficiently low background permit the charged particle count rate to be measured as the sum of all pulses above the LL discriminator. The count rate in the UL should be approximately half that of the LL, and major deviations from this indicate some electronic error which must be diagnosed and corrected.

4.3.2 Photon Signal Detection

An Ortec 660 5kV dual power supply provides the bias voltage for both HPGe gamma detectors. Incident photons produce a sharp voltage spike just as in the case of the charged particle detectors. On the gamma detectors, the signal is prepared by an internal preamplifier before proceeding to an Ortec 673 Spectroscopy Amplifier and Gated Integrator. Gain is chosen to permit good energy resolution on the 478 keV gamma peak to separate it from the ubiquitous 511 keV photons from $e^{-}e^{+}$ annihilation, and to provide adequate dynamic range of the energy spectrum for any additional measurements that are performed, such as the measurement of the absolute cross section of certain $^{10}\mathrm{B}\,(n,\gamma)^{11}\,B$ reactions. There is sufficient resolution at the minimum gain setting to resolve the relevant features. The Gated Integration function as well as busy signals are not used in the experiment. Electronics dead-time measurement is discussed in a later section.

The signal leading in to the SCAs is read from the unipolar output. The front-facing output is used for MCA spectrum measurements via the Tracor Northern MCA, while the rear-facing output for each detector is connected to a pair of Ortec 551 Timing SCAs.

4.3.3 Counting and Timing

TTL pulses from the discriminators are counted in a bank of Kinetic Systems 3610 Hex Scaler modules for the CAMAC standard bus (similar to NIM). Pulses are counted for

approximately 60,000 ms before the sum total is passed to the DAQ computer. This time-frame is determined using the computer's internal clock. A Kinetic Systems 3655 Timing Generator module produces a 1 ms timing signal to correct for computer under- or over-determination of the acquisition time.

A precision 25 Hz pulser with a mercury-wetted relay is used to calibrate the energy level discrimination in all of the detectors (see Fig. 4.15). The MCA channel corresponding to the energy of the relevant particles is determined by collecting an energy spectrum of the neutron-induced reactions in ^{6}Li and ^{10}B which are subsequently fitted to Gaussian curves around the reaction product peaks. The pulser output is then fed into the test input of one of the detectors and, again using the MCA, the pulse height is set to correspond to the channel at which a discriminator level should be set. Typically this will be at the minimum between a signal peak and either the noise tail, or a lower-energy signal peak. The SCA thresholds are determined by collecting 1-second-long data points and tuning the voltage setting until the count rate above the threshold is 12.5 Hz above background. For the Si detectors that background is typically close to 0, whereas for the HPGe detectors it tends to be ~ 3 Hz.

This same pulser is used to correlate the timing differences between Alpha-Gamma and the ^{239}Pu absolute activity measurement apparatus (^{239}Pu Counting Stack). Since there is no guarantee that the timing signals produced for each measurement are equivalent, the pulser is required to act as a portable, highly regular timing signal to allow comparison of the two sets of numbers: the initial ^{239}Pu activity measurement and the ^{239}Pu AG alpha detector calibration. This is discussed in more detail in Chapter 7.

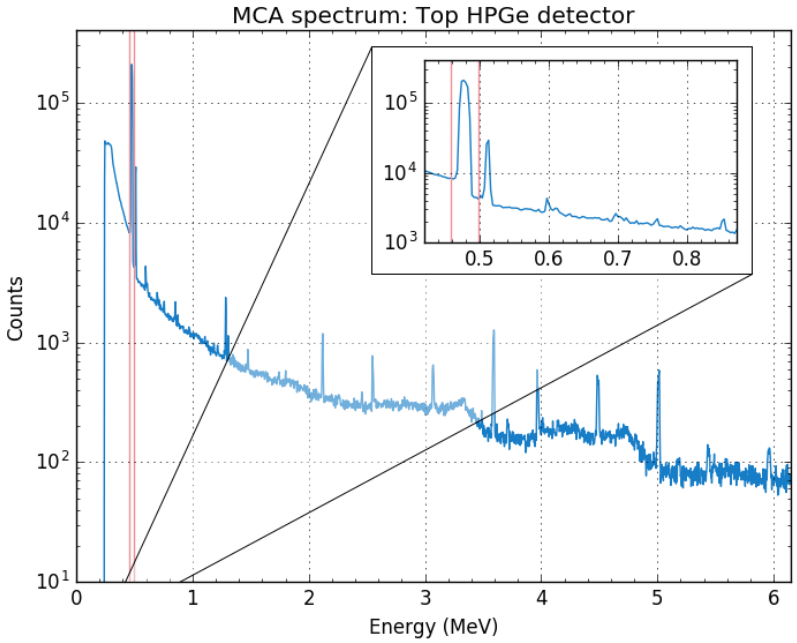
MCA spectrum: Top HPGe detector
Counts
Energy (MeV)

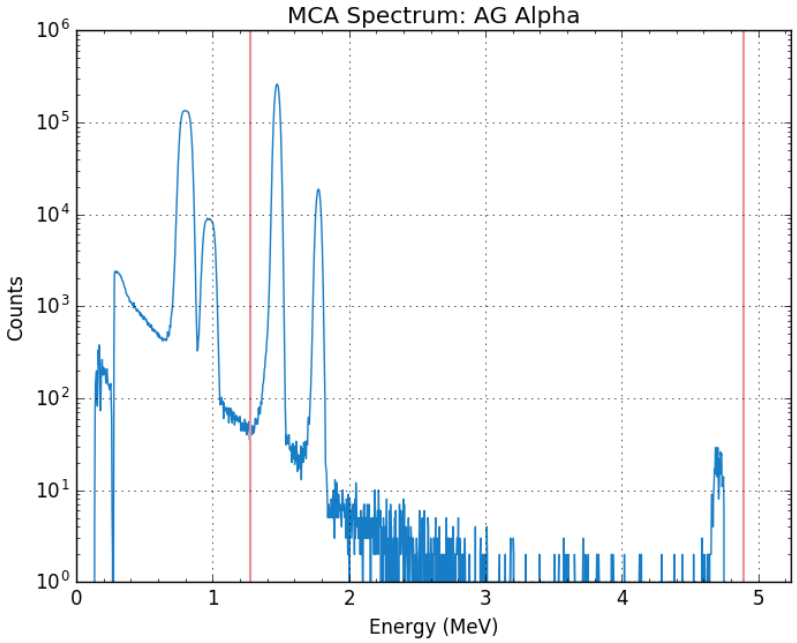
MCA Spectrum: AG Alpha
Counts
Energy (MeV)

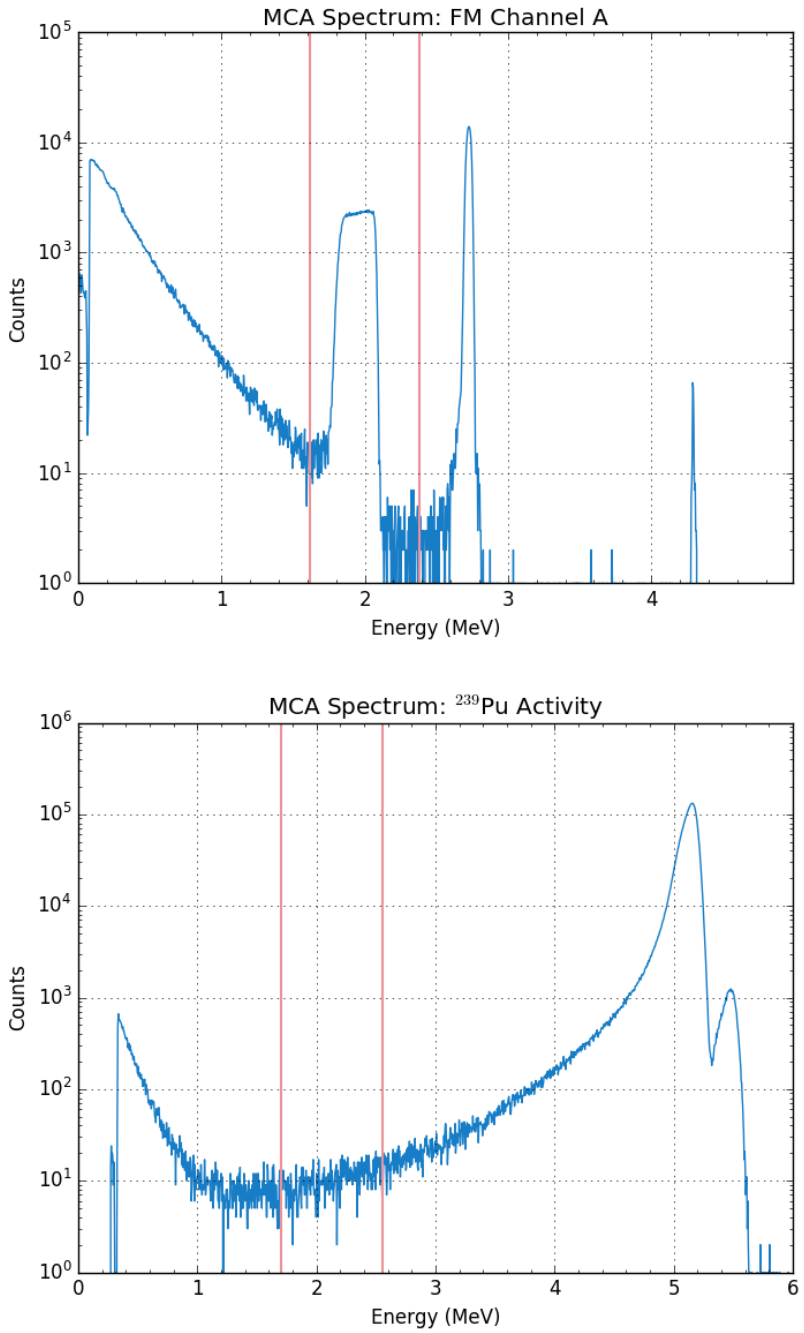

Figure 4.15: Plots of counts versus energy (corresponding to pulse-height) in the MCA. Typical locations for the SCA thresholds are given as the vertical red lines. First: the top HPGe detector with the thin ^{10}B target in place. Second: the AG Alpha detector with the thin ^{10}B target. The efficacy of the background subtraction technique enables the entire rate above the lower-level threshold to be counted. Third: Flux Monitor channel A. The entire rate above the LL threshold is counted here as well. Fourth: ^{239}Pu counting spectrum. The thresholds define the region which is used to assess the backscattered fraction and the charged particle proportion transmitted through the aperture mask. The upper level threshold is also used to measure the signal.

4.4 ^{239}Pu Counting Stack

The ^{239}Pu sources used in the Alpha-Gamma alpha detector calibration have been 23 kBq and 2.2 kBq alpha sources deposited upon a silicon backing with a thin graphite layer. This thin coating over the ^{239}Pu deposit is intended to permit the alpha products from radioactive decay to escape while suppressing sputtering fragments. This arrangement is referred to as a "semi-sealed" source. In practice, a thin polyimide film is suspended ~ 2 mm above the deposit to serve this function. Decay products are emitted into 4π. Using a diamond-turned precision aperture and a set of precision spacers, the solid angle subtended by the aperture for the Pu deposit can be measured to high accuracy. The detection rate of $\sim 4 - 5$MeV alpha particles then describes the total rate of decays of the deposit. This set of solid angle defining equipment is called the Counting Stack. The source used in the calibration of the two Flux Monitor configurations presented at the conclusion of this thesis is called 49-Si-1-4.

4.4.1 Counting Stack Apparatus

Measurement of the solid angle subtended by the detector aperture for a source mounted in the counting stack is performed with a Nikon MM-400SL metrology microscope. Combined with a Metronics Quadra-Chek digital readout, the microscope has an accuracy of $\pm 0.4\mu$m. Sensors connected to the alignment gears of the microscope sample surface and the eye piece determine the change in position. The vertical (Z) axis is aligned using a split-prism focusing aid, which projects two sets of grid lines which align when the Z-dimension is in focus. Since changing the focal point is controlled only by changing the height, the difference in the Z position δZ can be measured by bringing points at different heights into focus and recording the position.

All components are manufactured to maintain the flatness of the stack with respect

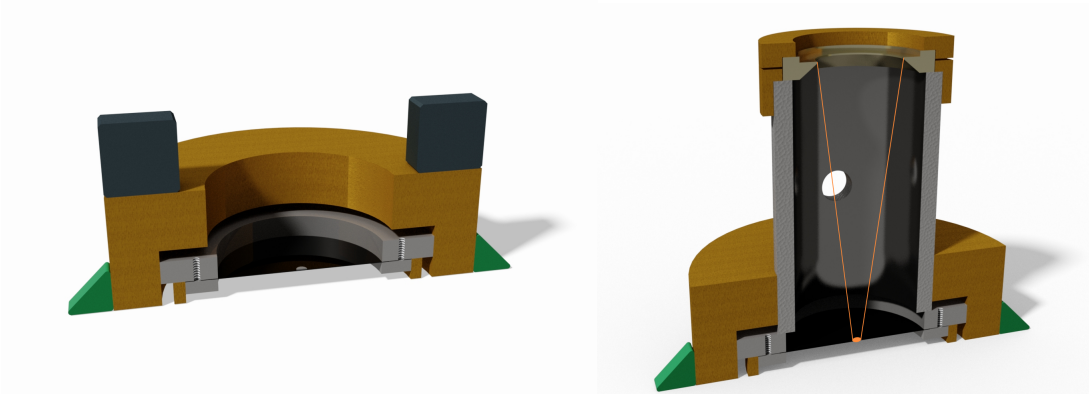

Figure 4.16: A rendering of the low solid angle counting stack used to measure the absolute activity of the ^{239}Pu source. Left: lead blocks used to weigh down the microscope sample table with the same force that the rest of the counting stack will produce. Right: the measurement of the aperture dimensions and height. The orange lines indicate the dimensions of the precisely measured solid angle.

to the surface upon which the Counting Stack (see Fig. 4.16) sits. A brass ring serves as the base for the Counting Stack. The Pu deposit is held by a deposit holder which fits snugly into the brass ring. A heavy brass cover aligns the counting stack with respect to an opening cut into its top while contributing weight to the stack. A precision spacer fits into the opening of the heavy brass cover. Grooves cut along the inside of the precision spacer are designed to suppress alpha scatter, and holes permit evacuation during the measurement. A brass alignment ring fits around the precision spacer and provides alignment for the diamond-turned copper aperture. Finally, a brass weight fits on top of the aperture to ensure that all components are compressed and settled.

The position and dimensions of the ^{239}Pu deposit are measured with only the brass ring and heavy brass cover in place. Since the rest of the equipment has weight which produces non-negligible deflection of the measurement surface, lead blocks of equivalent weight are placed on the brass cover during this measurement. Pieces of silicone putty are placed against the brass cover to stabilize the stack during the entire measurement. The aperture position and diameter are measured with the full stack in place (without the lead blocks). Systematic effects arising from the stack assembly procedure can be assessed by

disassembling and reassembling the stack several times.

With the measurement of the solid angle subtended by the precision aperture for the ^{239}Pu spot center in the counting stack determined, the stack can be placed inside a vacuum chamber and the activity of the Pu spot can be measured using a 900 mm^2 PIPS detector placed just above the aperture. This is done using the same techniques employed to measure the charged particles from ^{10}B using the Alpha-Gamma apparatus. The timing is done with an ORTEC 974A Quad Counter/Timer module. As mentioned earlier, since the veracity of the timing in the AG apparatus does not necessarily match that of the Counting Stack apparatus, the same 25 Hz precision pulser must be used to compare data collected between the two instruments. This technique is independent of the known activity of the ^{239}Pu source as well as its decay history.

Chapter 5

The Neutron Flux Monitor

The neutron Flux Monitor (FM) is a low-absorption, low-efficiency neutron detector which can be incorporated into many types of neutron beamline experiments. By determining the neutron detection efficiency ϵ_0 of the FM and defining it in terms of an idealized beam (line-like, monoenergetic 2200 m/s neutrons) incident upon an idealized target (infinitely-thin, isotropic areal density), the calibrated FM can be used on a diverse set of cold neutron beamlines with only a small number of beam-dependent corrections.

5.1 Flux Monitor Hardware and Design

The Flux Monitor efficiency can be quite low as long as it is known precisely. An important advantage of choosing the efficiency to be low is that its total neutron attenuation is also low. This enables measurement of the efficiency using an absolutely-calibrated apparatus downstream of the Flux Monitor. In our case this is done using the Alpha-Gamma apparatus. Once this measurement is completed, it also enables the calibration of other detectors downstream using the FM.

A rigid stainless steel structure positions a thin deposit of neutron-reactive material (to date, only evaporated ^6LiF has been used) on a silicon substrate. As neutrons pass through the device, a small number react with the deposit and emit detectable charged particles isotropically. Four 600 mm Si charged particle detectors face the target center at

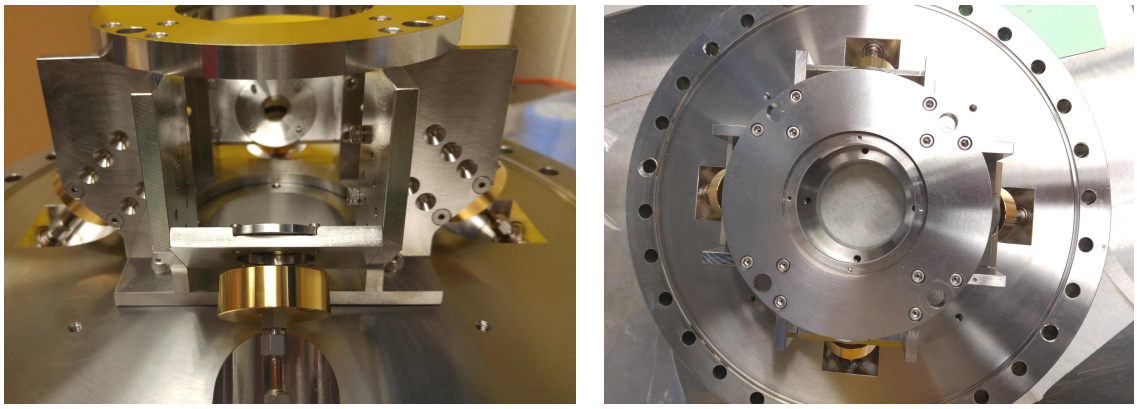

Figure 5.1: The specially-designed target Rigs rigidly and reproducibly orient the target deposits with respect to four stainless steel apertures which define a measurable solid angle. Detectors behind the apertures detect incident charged particles.

nearly 45 deg angles. Between the Si detectors and the target center are precision stainless steel apertures which rigidly define the solid angle Ω_{FM} subtended by the detectors for the target center. These are fixed in place by polished stainless steel hardware.

Each aperture is cut with a bore ∼12.7mm (0.5 in.) in diameter. In an effort to keep the apertures as identical as possible, the final grind of the inner diameter was made on pairs of apertures clamped together. This way, each aperture closely matches at least one other aperture, and any possible burring from the machining process is reduced along the critical inside edge. The metrology performed on these apertures is described in Sec. 2.7.

This collection of equipment has been called the "Rig," and the "Jungle Gym" (see Fig. 5.1). There exist two rigs; each one is attached to a 13.25" CF vacuum flange with a set of feedthroughs for the Si detectors. In operation a rig is attached to one of two vacuum cylinders ("vacuum can") which are then attached to the rest of a vacuum system. The measured efficiency ϵ_{FM}, and the calculated idealized efficiency ϵ_0 are determined for each individual rig-target combination.

The 45° angle at which the silicon detectors view the target center is chosen to minimize the change in the solid angle for different points on the target surface plane (Fig. 5.2). This is easily modeled using the expressions derived in Appendix C of Ref. [54], however it is only

true for the two-detector case (aligned along a single axis); for four detectors at identical viewing angles and distances, an angle of 34.8° from the target plane is preferred (Fig. 5.3). The most favorable angle differs depending on the solid angle subtended by the detector array for the beam spot center.

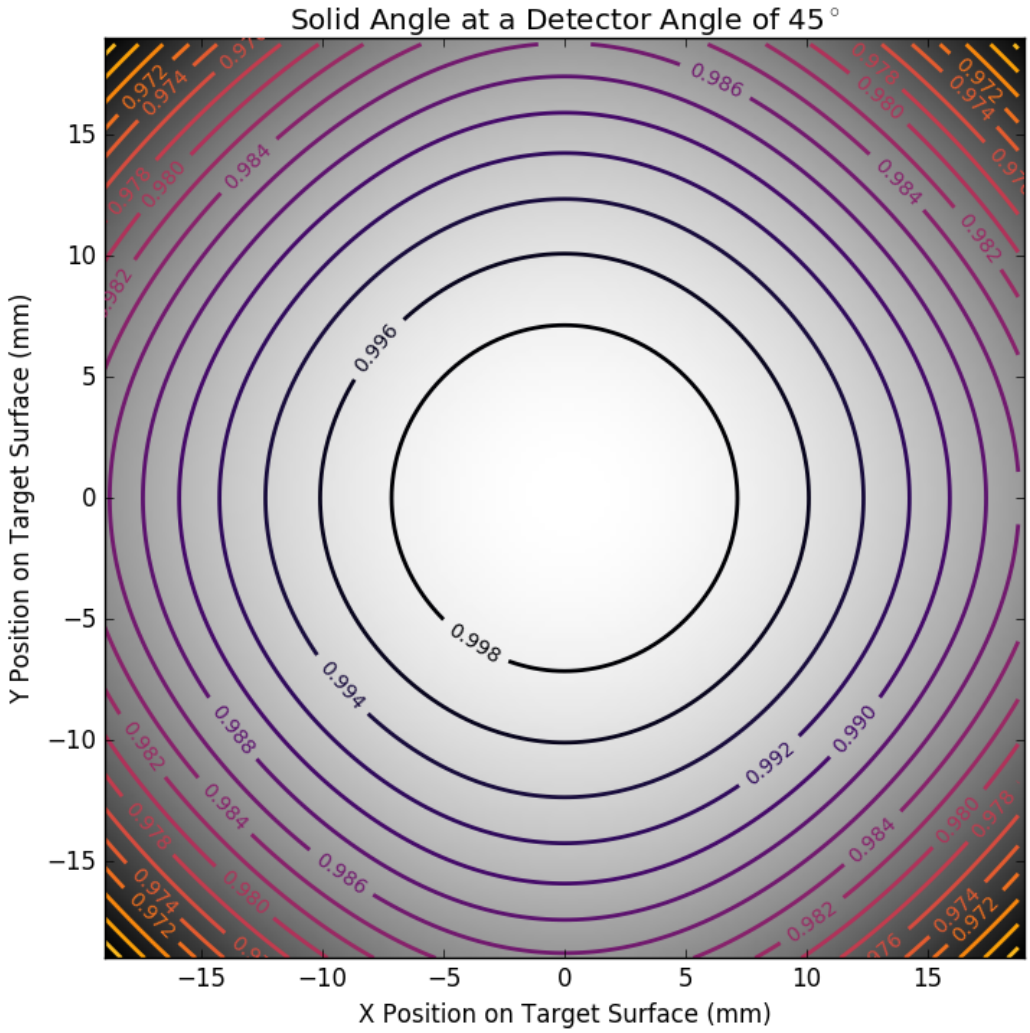

Figure 5.2: The solid angle subtended by the detectors for points on the target surface. The small deviation from circularity occurs as the coordinate point approaches one of the four detectors.

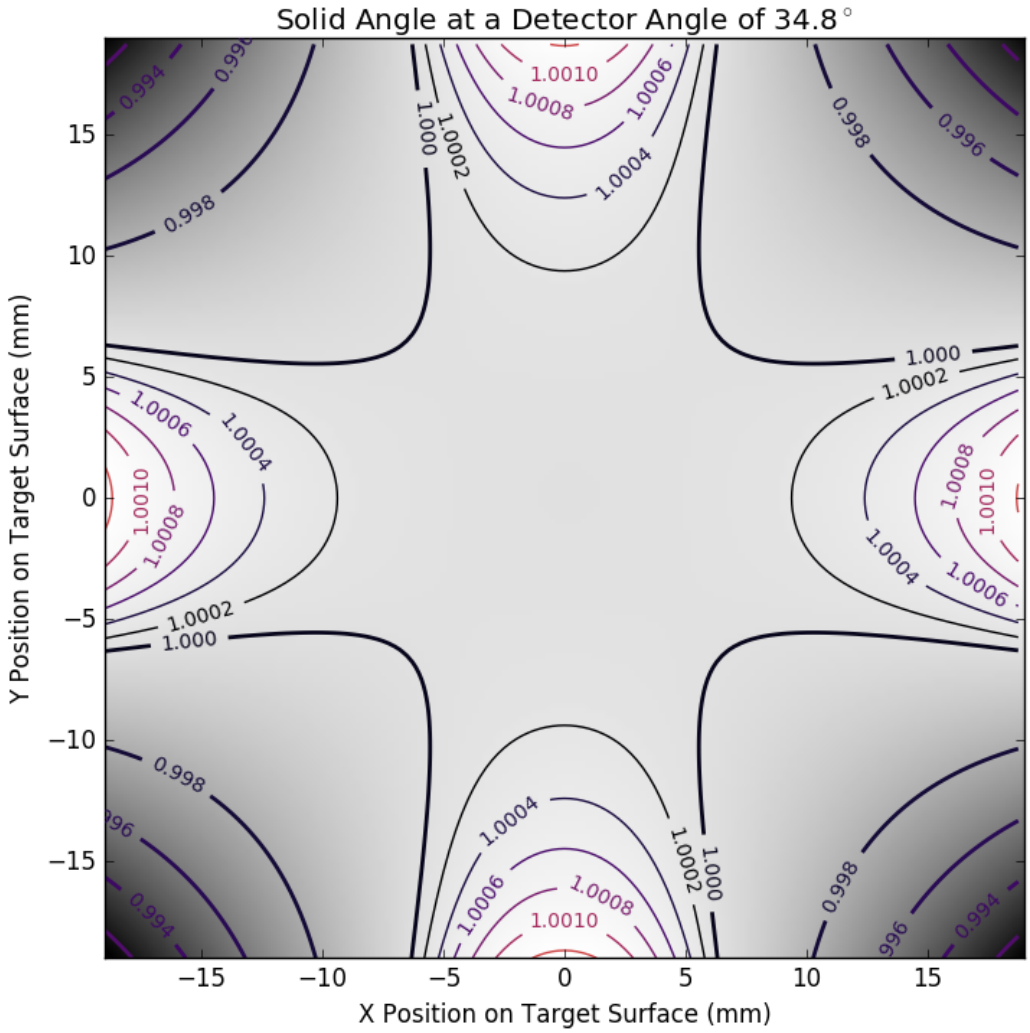

Figure 5.3: The hypothetical solid angle subtended by the detectors at 34.8° from the target plane. Notice that small changes in position induce a smaller change in the total solid angle as compared to the 45° case and, although the profile lacks circularity, the variation over the expected beam-spot size of ±7mm is very small. In this and the previous calculation, the solid angle is computed at each individual point across the target surface.

Targets are held in the FM by a target holder which is similar to the one used in the Alpha-Gamma apparatus except that, since the target is not held at an angle to the incident beam, there is no bevel cut along its inner diameter. The polished silicon surface still mates against a polished stainless steel surface as in the Alpha-Gamma holder, however there are several FM Target Mounts, each with slightly different thicknesses. Due to the way that the target holder is affixed to the Rig (in the direction of the detectors), the target mount thickness contributes to the distance between the target and the Si detectors, and must therefore be taken into account when applying corrections. They may also position the center of the target at slightly different locations. Notations on both components of the target mounting apparatus are kept so that appropriate geometric corrections can be made.

Current data were taken with a different alignment system than the new data will be. This is in part due to the fact that the previous alignment apparatus was a component of the in-beam neutron lifetime apparatus and needed to be returned. Using the previous alignment apparatus, the vacuum system rests on two hemispherical grooves cut in to aluminum plate ("yokes") (see Fig. 5.4). Alignment is performed using threaded alignment feet at the base of the FM/wavelength apparatus table. Improvements to this design include decoupling the FM alignment apparatus from the wavelength measurement setup and providing adaptable kinematic mounting.

Alignment of the FM proceeds in much the same way as it does for the rest of the apparatus, except that instead of using screws a special alignment cylinder which nests snugly into the target mounting location is used. At either end are four posts designed for threading cross-hairs such that they form an X at both the target center and a distance 4.5" upstream. A theodolite measures the adjustments that need to be made to align the target center to the beam-spot center, and the difference between the target center cross-hair and the upstream cross-hair measures the tilt. Adjustments to the target center position can

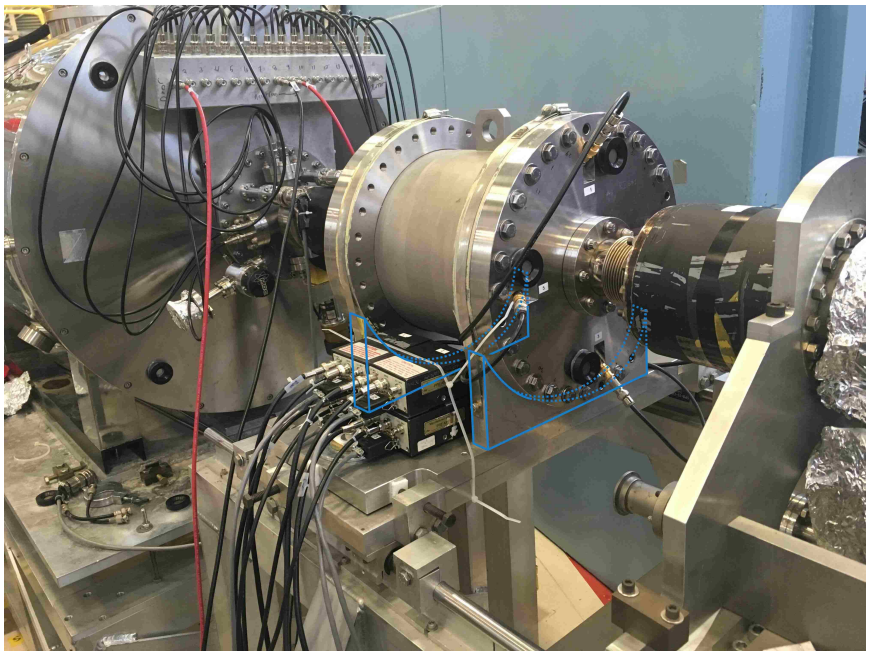

Figure 5.4: The previous alignment system is seen here in use on the in-beam neutron lifetime experiment. The yokes are outlined in blue. This is the alignment apparatus which was used to take data using the Flux Monitor until Spring 2017. The new alignment apparatus is described in Fig. 5.5.

be made by either shimming the FM yokes (or shimming the plate to which the yokes are attached), or by adjusting the feet of the stand upon which it sets (if the beam flight tube and collimation are going to be aligned later). The tilt of the FM with respect to the beam must be measured for systematic calculations; if it is tilted with respect to beam normal, neutrons passing through the target will encounter an increase in deposit thickness of $\mathcal{O}(\theta^2)$.

A newly-designed kinematic mounting system for the FM allows reliable, highly-precise alignment for future data taking. Three threaded ball stems rest on a steel cone, trough, and flat which are attached to a broad aluminum "pusher" plate. A V-shaped mounting block is positioned on the pusher plate using six set screws. The FM rests in the mounting block upon a second set of kinematic mounts. While the FM cannot be repositioned with respect to the V-block, the V-block itself can be translated along the aluminum pusher plate surface and the orientation of the pusher plate is easily controlled with the threaded stems. This setup is capable of aligning the apparatus to well under the measurement limits of the

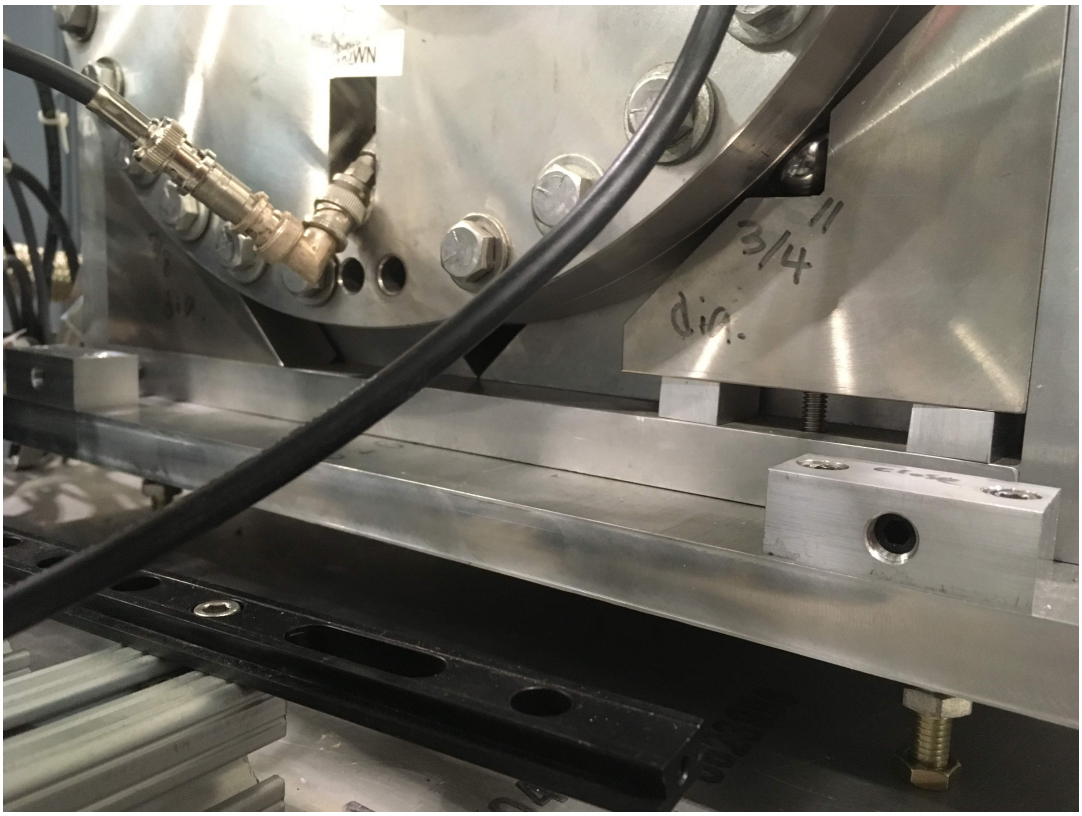

Figure 5.5: The new kinematic mounting system produces superior beam / Flux Monitor alignment. Steel kinematic bearings are seen underneath the CF flange, and ball-end threaded stems support the kinematic features between the plate and table.

theodolite. Data described in this thesis were taken using only the old alignment system.

5.2 Electronics

The 4 silicon charged particle detectors used in the Flux Monitor have the same energy resolution (33 or 27 keV FWHM) as the Alpha-Gamma Si detector. However, since the solid angle-defining apertures do not need to be disturbed to remove the detectors, they can be safely swapped out without losing information. This is only advantageous in the event of detector failure. 10-32 connector (also called Microdot) vacuum feedthroughs carry the bias voltage into and signal out from the detectors. Either the cabling or the Canberra 2006 preamp inputs must be customized to attach to the 10-32 connectors, since the Canberra devices only accept SHV as marketed, and SHV to non-SHV connectors are

not commercially available. In the case of Alpha-Gamma custom SHV-to-BNC connectors permit connection to 10-32 via the addition of a BNC-to-microdot adapter. The operation of the preamplifiers, amplifiers, and SCAs are identical to the AG alpha detector, as discussed in Sec. 4.3.1.

Chapter 6

Data Acquisition and Data Analysis

6.1 Methodology

As long as the background in the system remains constant between beam-on and beam-off states and the signal-to-noise ratio is adequate, large backgrounds do not affect the experiment. The 15 minute beam-on, 5 minute beam-off data period maximizes the signal-to-noise ratio for the data rate achieved during an FM calibration using typical collimation. By keeping the number of cycles per beam-state oscillation short ($15 + 5 = 20$m), the chance that the set of data is ruined by a change in background is reduced. The goal is therefore to minimize interactions between the data acquisition equipment and the environment. This is done mainly via appropriate electrical grounding and isolation.

Minimal processing is done to the main data streams before they are recorded. The data used in analysis are the threshold counting data for the two beam states, and the timing. The MCA spectra are used mainly for diagnostics or setup and are not used for the absolute counting. We do not rely on detailed models of the pulse processing electronics to calculate the dead-time. Dead-time is instead measured directly using the 25 Hz pulser (see Sec. 7.1).

6.1.1 Data Triplets

The efficiency of the HPGe gamma detectors drifts slowly in time. While to 1^{st} order this drift is linear, it is significant enough to affect the data over the course of a thin ^{10}B thick

^{10}B data set. Therefore data are acquired in a pattern of three data sets as follows:

1. the thin target is used to establish an alpha/gamma ratio (r_γ/r_α in Eqn. (2.11)), which calibrates the HPGe detector efficiency for neutron detection.

2. the thick target is used to measure the absolute flux simultaneously with the upstream FM.

3. the thin target is used a second time to establish an alpha/gamma ratio.

The value measured for r_γ/r_α in steps 1 and 3 is then used to extrapolate the effective r_γ/r_α ratio at the time of the absolute flux measurement in step 2 by simple linear interpolation (Fig. 6.1). The point in time used in the thick target calculation is just the average time of the viable data points taken during step 2. While both HPGe detector gains drift in time as seen in Fig. 6.2, the drift is linear over the timescales necessary for the 3-part data taking pattern. The average time of the thick target run is therefore a valid choice since, while the first half of the data set may be over-counting, the second half is under-counting by an equivalent amount. By book-ending the thick target runs with thin target runs, rather than oscillating between the two, statistical correlations between data sets are broken, which makes the data easier to interpret and analyze. The contribution to the statistical uncertainty from step 2 is about the same as the combined contributions from steps 1 and 3.

6.1.2 Calculating Ratios in Alpha-Gamma

The number used for absolute flux measurement during efficiency determination is the Gamma/Alpha ratio (see above, Sec. 6.1.1).This ratio is **not** calculated for each 20m data point from a data set. Instead, the total number of alphas and gammas counted are summed separately, and the ratio of those sums is used. This is done so that there is no difference

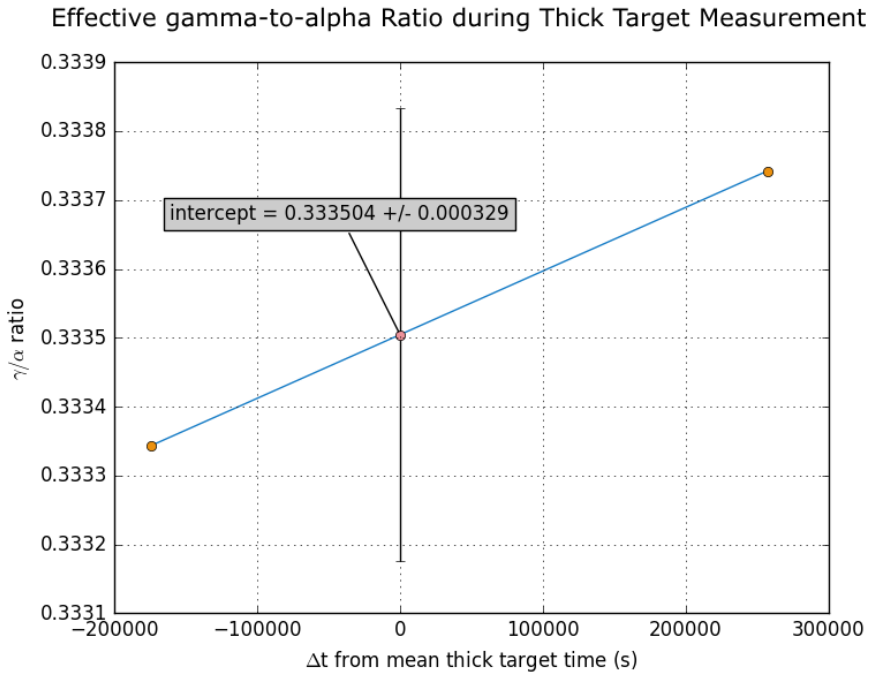

Figure 6.1: A plot of the gamma count rate divided by the alpha count rate in the Alpha-Gamma experiment for the first thin target run, the thick target run, and the second thin target run. The γ/α ratio varies linearly over the timescale of a triplet.

between using the ratio or using the data to calculate the number of particles counted (neutrons, charged particles in the FM or AG, gammas in the HPGe detectors).

When calculating a mean value $\bar{x}$ of a set of data x_i for $i = 1, ...n$, the goal is that, when the values x_i are replaced with $\bar{x}$, there is no change in a desired quantity of interest. Since Alpha-Gamma is primarily a particle counting experiment, the chosen constant is the total number of particles counted. The method used to determine the expression for each mean value is called the Chisini mean [55] [56]. Let the ratio $r_{\gamma i}/r_{\alpha i} = x_i$. Require the total number of α particles counted to be a constant under the replacement of each x_i with the average $\bar{x}$:

$$\begin{aligned} y(x_1, x_2, ..., x_n) &= \sum^{n} \frac{r_{\gamma i}}{x_i} = \sum^{n} r_{\alpha i} \\ y(x_1, x_2, ..., x_n) &= y(\bar{x}) \end{aligned} \tag{6.1}$$

By assuming an inverse equation $\Theta^{-1}(f)$ such that $\bar{x} = \Theta^{-1}(y(\bar{x}))$, an expression for

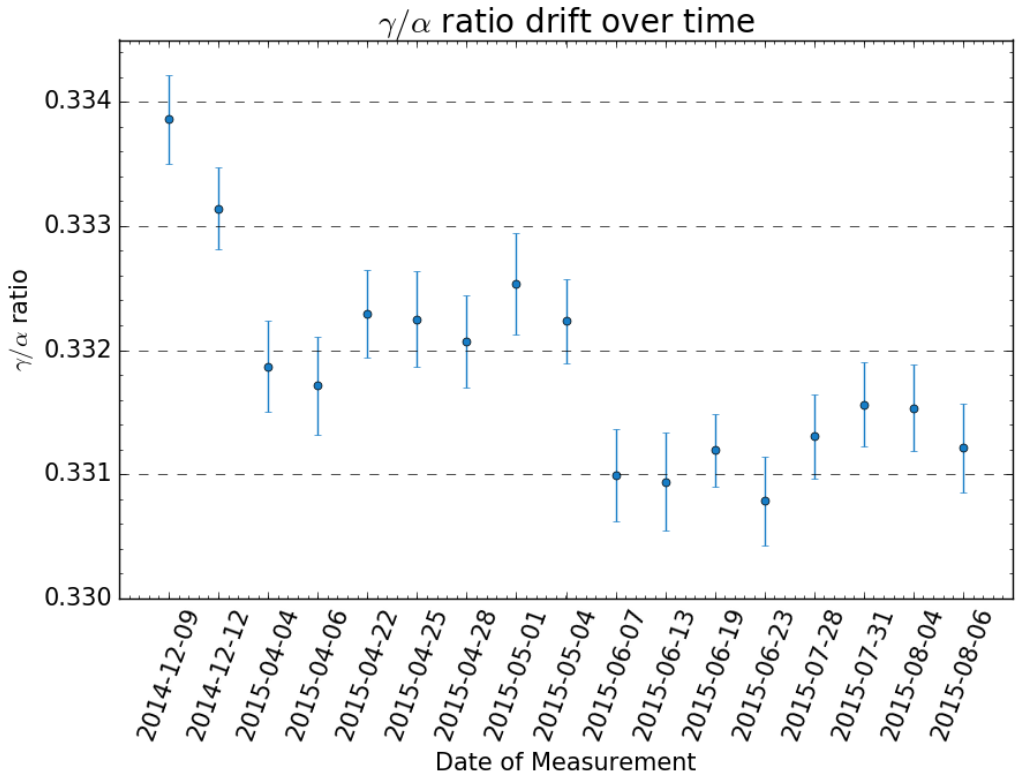

Figure 6.2: A plot of the γ/α determined for each triplet of the 30-H3 Rig #2 efficiency measurement. The γ/α ratio further varies over the course of a year, which more clearly demonstrates the motivation for the triplets.

the mean value $\bar{x}$ can be written in terms of $(x_1, x_2, ..., x_n)$:

$$\bar{x} = \Theta^{-1}\left(y\left(\bar{x}\right)\right) = \Theta^{-1}\left(\frac{1}{\bar{x}}\sum^{n} r_{\gamma i}\right) \tag{6.2}$$

Θ^{-1} is then comprised of the operations necessary to extract $\bar{x}$:

$$\begin{aligned} \bar{x} = \Theta^{-1}\left(y\left(\bar{x}\right)\right) = & \left(\frac{\frac{1}{\bar{x}}\sum^{n} r_{\gamma i}}{\sum^{n} r_{\gamma i}}\right)^{-1} \\ \Theta^{-1}\left(y\right) = & \left(\frac{y}{\sum^{n} r_{\gamma i}}\right)^{-1} \end{aligned} \tag{6.3}$$

and combining Eqn. (6.1) with (6.3):

$$\bar{x} = \Theta^{-1}\left(y\left(x_1, x_2, ..., x_n\right)\right) = \left(\frac{\sum\limits^{n} \frac{r_{\gamma i}}{x_i}}{\sum\limits^{n} r_{\gamma i}}\right)^{-1} = \frac{\sum\limits^{n} r_{\alpha i}}{\sum\limits^{n} r_{\gamma i}} \tag{6.4}$$

Since rates are taken simultaneously, and therefore the total time spent counting in the numerator and the denominator is the same, Eqn. (6.4) is equivalent to the ratio of the sums of particles in each channel.

The choice of the constant value expression $y\left(x_1, x_2, ..., x_n\right)$ is application- and measurement-specific and affects the calculation of uncertainty. This technique reproduces the various well-known mean value expressions (arithmetic, harmonic, geometric) with the proper choice of $y\left(x_1, x_2, ..., x_n\right)$, in addition to establishing an epistemological metric for using that mean. In this experiment, mean value methodology changes a given ratio by up to $\pm 0.01\%$. This is well below the uncertainty goal of the Penning trap in-beam neutron lifetime experiment now in progress, but proposed future follow-on experiments will need to take these issues into account.

6.1.3 Data Analysis

Data are collected into 20 minute sets of 15 minute beam-on / 5 minute beam-off groups. Beam-off data is used for background subtraction. Before combination of the data into the r_γ / r_α ratio, the counts from the top and bottom HPGe detectors must be combined. As seen in Eqn. (2.11), all data contributes multiplicatively to the result. It is therefore convenient if all of the corrections combine multiplicatively as well. In order to do this, top and bottom HPGe data are combined using the geometric mean:

$$r_{\gamma comb} = \sqrt{r_{\gamma B} \times r_{\gamma T}} \tag{6.5}$$

This form of the mean is necessary because, unlike the Flux Monitor data which also uses multiple detectors, the corrections to the gamma data are different for the top and bottom detectors.

The large number of covariances associated with the corrections makes direct analysis of the uncertainty difficult. Instead, both the data and the corrections are varied by their individual uncertainties under Poisson statistics, and the Flux Monitor efficiency is recalculated. By doing this multiple times with the same data, the distribution of the data given the uncertainties and their covariances can be determined. Often a single calculation or measurement of a correction is used across multiple otherwise disparate data sets (different collimation, FM target, etc.). When computing results in such a case where these data sets are used or presented, the correction is only varied once per computation (as opposed to once per data set per computation). This procedure avoids under-estimating the uncertainty.

Several sets of analysis code exist to process Alpha-Gamma data. Andrew Yue developed a large number of tools in the Igor interactive software environment which exist as multiple separate .pxp files on a backup drive and on at least one other HDD at the NIST NCNR. I independently developed analysis tools in Python 3.x which exist on the Alpha-Gamma Elog.

From the data, triplets are formed as described in Sec. 6.1.1. These are used to determine the absolute flux of neutrons in the beam while simultaneously measuring the response of the upstream Flux Monitor. For each triplet, an individual Flux Monitor efficiency ϵ is measured for the NG-6m beam. Combined with systematic corrections, both experimental and those necessary to record the efficiency in terms of an idealized beam incident upon an idealized target, data are collected to produce the highly precise Flux Monitor efficiency ϵ_0.

6.2 DAQ Equipment

6.2.1 CAMAC

As mentioned previously, TTL pulses from SCA threshold-mode detectors are counted in CAMAC 3610 hex scalers and timing from a 3655 Timing Generator manufactured by Kinetic Systems. Similar to NIM, CAMAC comprises a standard by which communication and control systems for an experiment and its sensors can be designed [57]. Instrument signals and external communication is located on the front of each module, while power and an internal data transfer system (sometimes called the Dataway) connect along the back. These can accommodate fairly complex DAQ hardware in a small form factor.

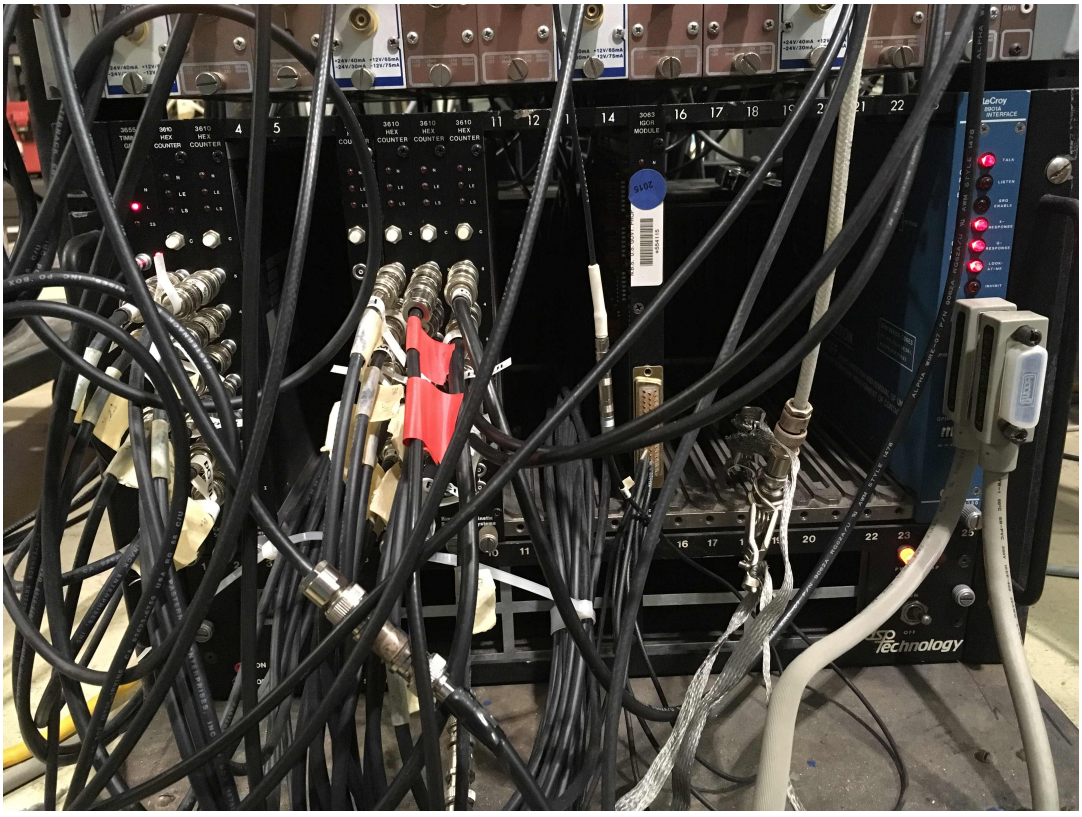

Figure 6.3: The CAMAC electronics mediate control and data flow for the experiment.

The IGOR module controls the lithium flag which blocks the beam for beam-on/-off background subtraction, and collects signals indicating the state of the apparatus and its

environment. It also reads the resistance on the thermocouple connected to the Be filter cryostat. Changes in the gamma background and electrical noise result from changes in the neighboring experiments. Since the experiment is precise enough to measure the absolute efficiency of the FM to $< 0.1\%$, changes in background during a 20 minute data period in excess of this value invalidate that portion of the dataset. It is impractical to use shielding and isolation sufficient to reduce the effects of background below our sensitivity, so on-line background measurement and monitoring of changes in background are implemented instead. This is done using TTL signals from NG-6 end station, NG-6U, and NG-6m which monitor their respective shutter states.

6.2.2 DAQ Computer

A GPIB cable carries most of the data signals from the CAMAC crate to the data acquisition computer. The National Instruments PXIe crate reads a second set of data from the gamma detectors, the AG alpha detector, and the "A channel" of the FM, although these signals are similar in content to other data streams. The control software is written in LabWindows CVI, a C-based IDE with built-in UI and measurement libraries (see Fig. 6.4).

Since the computer timing (which dictates how long each 1-minute data cycle lasts) may deviate from real time due to processor loads or the occasional error, the CAMAC timing module records the real length of each data cycle. The typical length of a data cycle is 59.995s according to CAMAC, although occasional excursions to ~ 60.025 are not rare. This can be compared to the NIM pulser rate to measure the difference between the CAMAC timing module and any other setup which accepts tail-pulse signals from BNC.

6.2.3 Data Files

Data files are produced as tab-separated columns whose rows correspond to a single 1 minute data set. Tab 2 of the data acquisition UI "Data Summary Plots" describes the contents

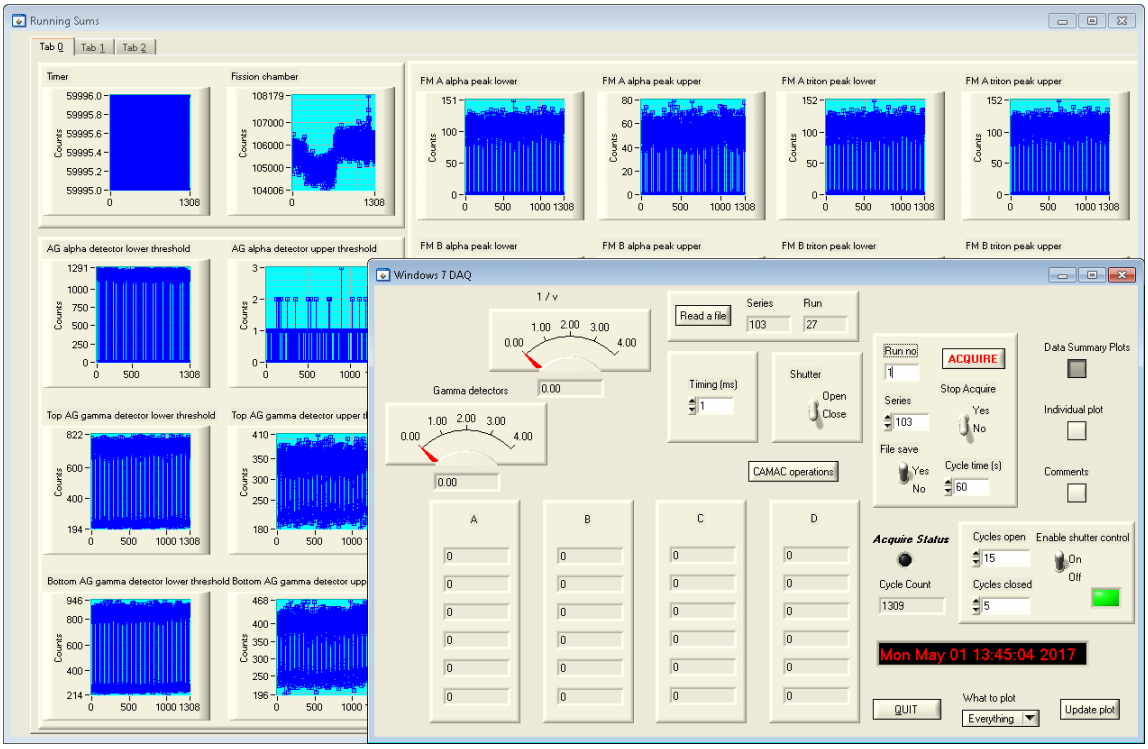

Figure 6.4: An image of the DAQ interface. Timing, labeling and comments are controlled from here. Real-time graphs plot the data after each cycle. During data taking, the A, B, C, D columns would be filled with the sums of each plot.

of each column from 0 to 39. Less-used data columns are repurposed for measurement of other quantities of interest, such as counting data from other detectors for calibration or regions of interest in the energy spectrum of incoming particles.

Without getting into too much detail, several of the data columns benefit from explanation. "Time" in column 28 is the time since January 1st of the current calendar year, in seconds, at the time of recording. "Shutter Status" (col 29) is recorded as 2 if the lithium flag permits beam to pass (the "beam-on" condition), and 1 if it is blocking the beam ("beam-off"). With the additional operation of NG-6U, the NG-6 Shutter Status indicator varies between 0, 30, 90, and 120. If a cycle contains a change in the state of one of these shutters, the value recorded will be between the given values. Since this is likely accompanied with a change in the background in excess of 0.1% of our signal, the cycle must be discarded. The rest of the columns are fairly self-explanatory. It should be noted that the

original data sets may have columns swapped due to temporary fixes, most notably the lower-/upper-threshold of FM channel C.

Critical to analysis of the data is knowledge of the systematic conditions of the apparatus, and therefore what ancillary data are associated with a given data series. Some of this vital information is recorded by hand in the newest comment files written in the DAQ software while beginning data taking. Other data sets are collected in different ways, via other experiments, or using different software, and therefore are not as easily recorded. For consistency, the Comments should contain sufficient information to identify what hardware is used in a particular data series: which rig, targets, target holders, and collimators, as well as which vacuum chamber (until kinematic knowledge of the rig orientation can be achieved in other ways). All data taken using the Alpha-Gamma apparatus are stored on a recovery drive as well as on analysis computers used by NIST guest researchers and staff. As of this writing, there is not currently an online repository for the data.

Chapter 7

Corrections and Systematics

The efficiency of the flux monitor depends on the neutron energy and other properties of the neutron beam phase space unique to each beamline. Therefore the corrections applied to the data are not only designed to account for systematic corrections to the Alpha-Gamma, ^{239}Pu counting, and FM signals, but also to refer the determined efficiency of the FM ϵ_{FM} to a standard point in neutron beam phase space. This reference neutron beam and target is a parallel beam of neutrons with a speed of v_0 =2200 m/s incident upon the center of an infinitely-thin ideal target. The efficiency of the flux monitor under these conditions is denoted $\epsilon_0\,(0,0)$ (abbreviated to ϵ_0). The rest of this chapter lists the size and sign of these corrections and explains their physical origin in detail.

7.1 Dead time and Pulse Pileup

The charges and currents produced in the detectors by incoming particles are processed by the electronics to measure count rates by threshold counting as described in Sec. 4.3.1. During the time necessary to process an incoming signal, a second particle can interact with the detection medium and induce more current. If the electronics have not fully processed the previous pulse, the second particle may not be detected, or its energy may be erroneously summed with that of the first particle. Both effects lead to a loss in count rate, and require a correction.

Pulse pileup occurs when the energy from a second particle is summed with the energy from the first particle before the energy analysis of the first event has been processed. This electronics-dependent phenomenon represents a loss of signal if the energy from a particle that would otherwise have produced a signal is pushed above the upper level threshold of the SCA used for counting analysis. Since this phenomenon happens before the signal encounters the SCA electronics, this form of signal loss depends only on the properties of the upstream items in the counting chain: detector, pre-amplifier, and amplifier. The rise time of the preamplifiers is extremely short (Canberra 2006 rise time $<$ 20ns, HPGe preamp $<$ 2.5ns), so pulse pileup happens primarily in the spectroscopy amplifiers. Both the gamma detector and charged particle detector spectroscopy amplifier adjustable shaping times are set to 1 μs which results in distortion when particles arrive with a short enough difference in time Δt.

Further downstream in the electronics chain (Fig. 7.1), the SCA inputs accept pulse widths as narrow as 0.2 μs, and output a NIM-standard 5V square pulse 500 ns wide. If two pulses from the spectroscopy amplifier arrive within this timespan, the second pulse would not be issued due to the width of the first pulse and the processing required to issue that pulse. This also produces dead time. However since the rise time of the spectroscopy amplifier is much longer than the SCA output width, the setup experiences pulse pileup first, which results in the conversion of two pulses into a single higher energy pulse. The 3610 Hex Scalers accept frequencies up to 50 MHz, which is well under our rate limit imposed by pulse pileup in the upstream spectroscopy amplifiers.

7.1.1 Signal Loss in the Si Detectors

Signal loss occurs when the relative time between incoming pulses distorts the pulse shape produced by the spectroscopy amplifier and from dead time due to electronics processing

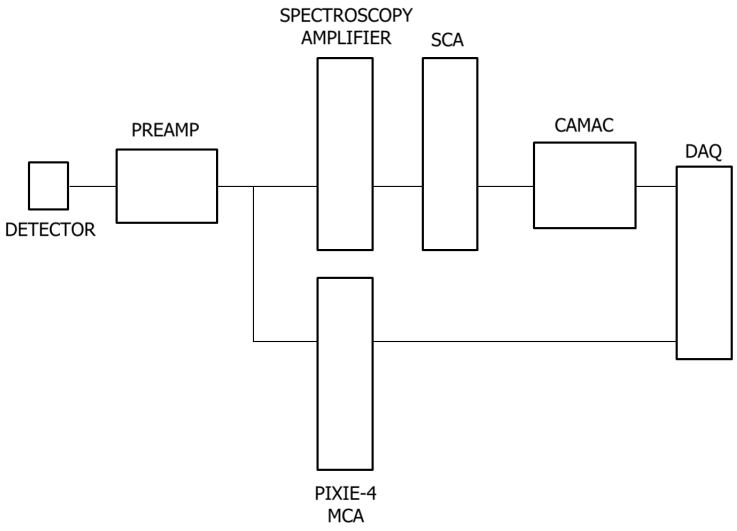

Figure 7.1: Electronics diagram for a single channel of the Alpha-Gamma and Flux Monitor detectors.

in the SCA and other components. While the pulse width seems to imply that pileup will be the primary culprit, a method which encapsulates both loss mechanisms will ensure that nothing is missed. We use a modified two-source method to determine the dead time at a given rate in the signal region, and then the rate in the signal region during a measurement is used to determine the dead time using the non-paralyzable model for the dead time [58]:

$$\rho = \frac{R}{1 - R\tau} \tag{7.1}$$

where R is the measured rate, ρ is the real rate, and τ is the dead time coefficient. The non-paralyzable model is valid when the time during which the electronics cannot detect a second pulse is not extended if a second pulse arrives (see Fig. 7.2).

A high activity ^{240}Pu source can be used with the solid angle counting stack to determine the dead time of the system. Since the source activity ρ remains roughly unchanged over short timescales, a difference in count rate R is proportional to the difference in solid angle at two distinct stack heights. Therefore for true count rates and measured solid angles $\rho_1,\ \rho_2,\ \Omega_1,\ \Omega_2$,

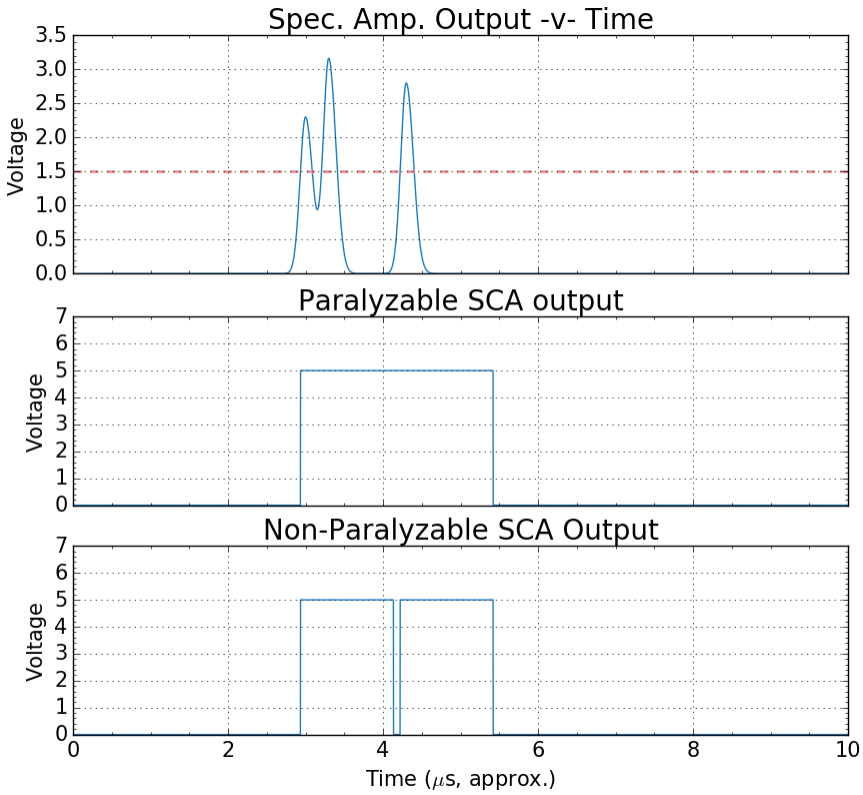

Figure 7.2: A descriptive model of dead time in the paralyzable (middle) and non-paralyzable (bottom) models with the same dead time coefficient τ. A non-paralyzable dead time is not extended when a pulse arrives, resulting in two out of three incident particles counted. A paralyzable dead time is extended if a second (or third, etc.) pulse arrives; this can sometimes be a longer, artificially applied dead time as determined for a particular application.

$$\frac{\Omega_1}{\Omega_2} = \frac{\rho_1}{\rho_2} \tag{7.2}$$

Plugging in (7.1) for $\rho_{1,2}$,

$$\frac{\rho_1}{\rho_2} = \frac{1-\tau R_2}{1-\tau R_1} \tag{7.3}$$

and solving for τ, letting $Q = \frac{\rho_1}{\rho_2}\frac{R_2}{R_1}$

$$\begin{aligned} 1-\tau R_2 &= Q\,(1-\tau R_1) \\ \tau\,(QR_1 - R_2) &= Q-1 \end{aligned}$$

$$\tau = \frac{Q-1}{QR_1 - R_2} \tag{7.4}$$

The uncertainty $\mathrm{d}\tau$ is calculated by variation of the measurable parameters R_1, R_2, and $\frac{\rho_1}{\rho_2} = \frac{\Omega_1}{\Omega_2}$ by their standard deviations under Poisson statistics. Added in quadrature, this gives

$$\mathrm{d}\tau = \sqrt{\left(\frac{d\tau}{dR_1}\right)^2 + \left(\frac{d\tau}{dR_2}\right)^2 + \left(\frac{d\tau}{d\frac{\Omega_1}{\Omega_2}}\right)^2} \tag{7.5}$$

As with the ^{239}Pu source used in this experiment, a thin polyimide film suspended $\sim$ 2mm above the deposit prevents sputtering of the ^{240}Pu [59]. The attenuation of the forward-emitted alpha particles is small due to the longer range of higher energy charged particles in matter [60] [61] [62]. Alpha particles backscattered off the Si substrate are emitted into 4π with a continuous energy spectrum from 0 MeV to the peak energy of 5.16817 MeV [63]. This produces a roughly uniform background across the spectrum. Although lower energy alpha particles are more strongly attenuated by the material between the substrate and the detector, the flat region of the spectrum between the noise tail and the beginning of the ^{239}Pu decay alpha peak is high enough in energy for this to be a negligible effect. Measuring the count rate per channel in this region using an SCA in threshold mode just as in the rest of the experiment, the contribution to the background can be determined and subtracted from the peaks. Since the backscattered portion is similarly emitted into 4π, and the modified two-source depends only on the observed rates and not the overall spectrum, it should be sufficient to ignore both of these corrections. Backscatter subtraction is included and represents a -0.4% correction to the measured rate. However the background without a source of charged particles must be measured at each stacking height, since this likely does not fall off as $1/r^2$ like the rest of the rates.

Using this method, the dead time was determined to be 2.205 $\pm$0.050 μs. Plugging in the

charged-particle count rate during thin ^{10}B target measurements in Alpha-Gamma results in a sufficient approximation of the dead time. This approaches congruence when the signal is much larger than the total background. Since the Alpha-Gamma alpha detector lower level threshold is set between the ^{7}Li and alpha peaks, and the upper level threshold is set very high, signal pileup does not result in a loss of counts. Therefore the signal count rate is a good quantity to use to determine the dead time in the system provided the signal is doubled due to the unmeasured ^{7}Li peak. Since the electronics which perform timing can be different between the Alpha-Gamma apparatus and the low solid angle counting stack, the pulser rate is used as a transfer calibration. The pulser rate remains fixed, so the difference in the measured pulser rate between Alpha-Gamma and the counting stack is proportional to the difference in the timing.

7.1.2 Signal Loss in the HPGe Detectors

Signal loss from dead time and pulse pileup is small but significant in both thick and thin target configurations. The rate of gammas incident upon the detectors is $\sim$ 1000 Hz in the thick target, with $\sim$ 300 Hz coming from the 478 keV signal. Since there is no effective way to precisely modulate the particle intensity as there is with the Si detector electronics, a pulser method of dead time correction is implemented.

In the pulser method [64], a periodic or random pulser with a well known rate is added to the preamp signal to interfere with the data signal. Setting the pulser voltage high enough that it lies above the energy regime of the bulk of the spectrum, the difference between the measured pulser rate and its known rate yields the dead time. A random pulser self-interferes just like the data signal; this means that the total gamma rate into the detector can be used to describe the parameters of the dead time in the system. Since a periodic pulser does not self-interfere, the total gamma rate is artificially inflated. Instead

the periodic pulser only measures the dead time for the data set when it is used.

All iterations of the Alpha-Gamma experiment calculated the dead time using the 25 Hz periodic pulser by measuring the loss of pulser counts in the high-count-rate thick target configuration of the experiment and applying a linear approximation to calculate the dead time of the low-count-rate thin target measurement. SCA windows must be set precisely the same distance away from the pulser peak as the windows around the 478 keV gamma peak are set. In this case if an incoming gamma ray is capable of boosting the apparent energy of a 478 keV signal outside of the measurement region, it is similarly capable of boosting a pulser signal outside of its own signal region. Since the pulser peak is narrower than the 478 keV peak, there can be very small differences for very low energy gammas which would merely move a lower-end 478 keV to the higher-end 478 keV region, but this is negligible.

The extrapolation from the dead time test data to dead time in the experiment is done by plotting the pulser count rate as a function of the background-subtracted 478 keV gamma signal. The data are fit to a line with the $X = 0$ signal condition fixed to an assumed 25 Hz rate (see Fig. 7.4). While there is additional dead time due to the pulser which is not present during live data taking, the effect is less significant at higher gamma rates from higher neutron flux through (and therefore higher total absorption in) the thick ^{10}B target). But the pulser rate is slightly higher than 25 Hz, and the measured rate with 0 background-subtracted counts in the signal region is slightly less than 25 Hz. In addition, according to the Tracor-Northern MCA, the proportion of the full spectrum detected within the 478 keV region is different for the thick versus the thin ^{10}B target state. This motivates an improved scheme for dead time measurement. The current values for the dead time correction, in terms of the measured gamma rate, are given in 7.1. The lines describing the dead time correction are:

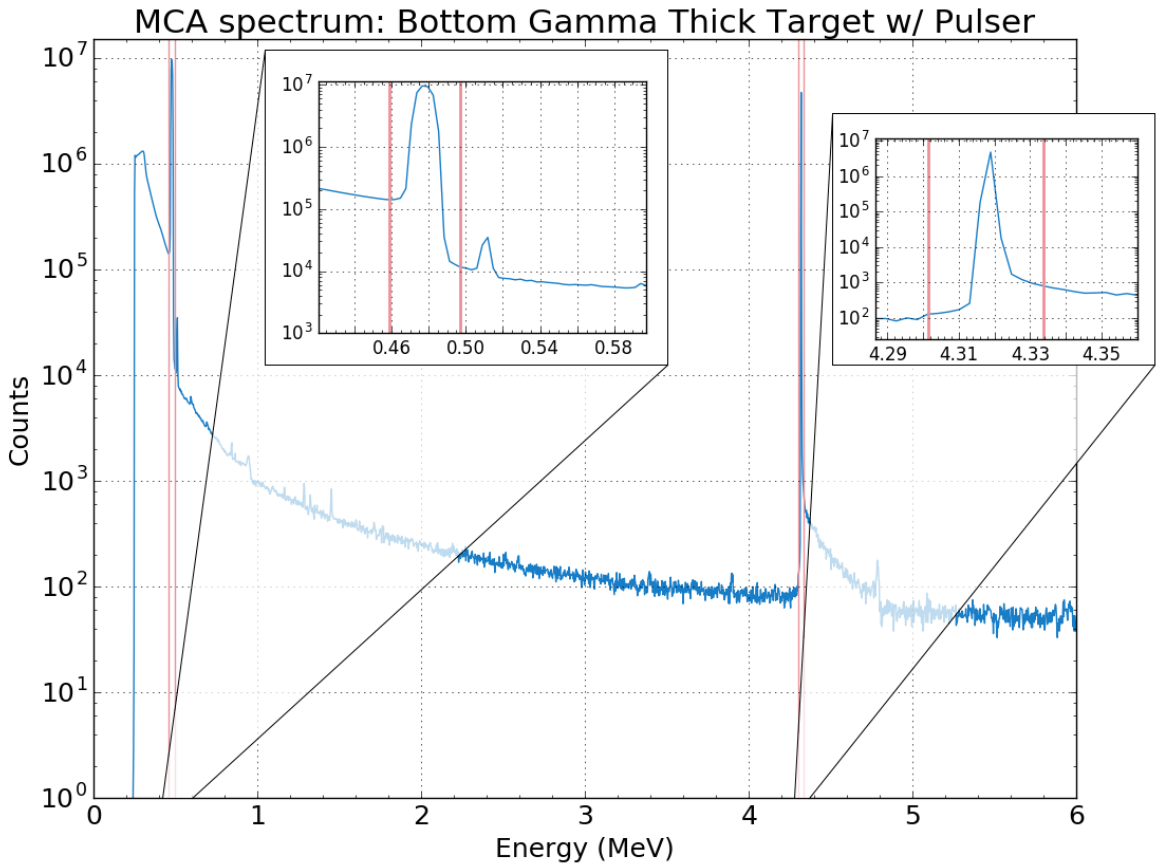

Figure 7.3: A Tracor-Northern MCA spectrum of the bottom gamma detector with the pulser. Vertical lines indicate thresholds defining signal windows. These are set at the same distance from the edges of the pulser peak as they are from the edges of the 478 keV signal peak. Note how the signal pileup pushes pulser counts above the upper level threshold. The 478 keV + pulser peak sum is visible at channel ~ 1650

$$1 + r_\gamma \times \tau_{(T/B)}/1500 \tag{7.6}$$

where, for the top detector, $\tau_T = -0.000599 \pm 0.0000087$, and $\tau_B = -0.000709 \pm 0.000017$ for the bottom detector.

An additional data stream will be added to the Alpha-Gamma system which measures the pulser rate for each data run. The pulser will be fed into the test inputs of both top and bottom HPGe gamma detectors, and the measured pulser rate will be recorded live. A

Table 7.1: Gamma detector pulser measurements for dead time calculations.

Top γ		
478 keV rate (cpm)	Pulser rate (cpm)	Pulser rate error (cpm)
25550.7	1458.16	0.60
17038.0	1490.51	0.16
25678.5	1484.82	0.15
11956.1	1493.02	0.16
16900.2	1489.58	0.61
25546.0	1483.48	0.76
25550.9	1483.51	0.52
17024.6	1489.04	0.37
0.0	1500.206	0.007

Bottom γ		
478 keV rate (cpm)	Pulser rate (cpm)	Pulser rate error (cpm)
29435.4	1481.07	0.79
29413.9	1480.28	0.72
19619.7	1488.37	0.41
19444.0	1487.65	0.60
19407.6	1488.85	0.45
17131.65	1487.79	0.08
0.0	1500.206	0.007

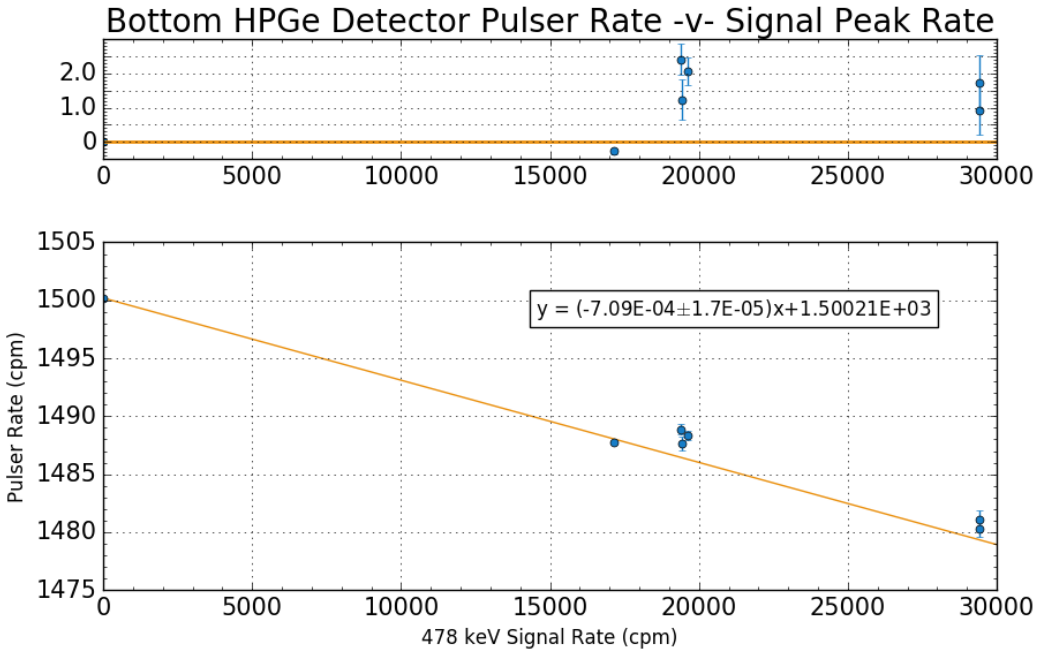

Figure 7.4: The pulser rate plotted as a function of the background-subtracted 478 keV gamma peak. The residuals are shown at top.

third Single channel analyzer (SCA) will read the true pulser rate during the measurement. No extrapolation will be necessary, and this method is accurate without knowledge of the incoming number of gamma rays or the shape of the spectrum.

The multiplicative correction applied to the data for the effect of dead time depends on the mean signal rate in each channel. Since data are combined multiplicatively to calculate the Flux Monitor efficiency (see Eqn. (2.11)), the dead times can be similarly combined into a single number. The dead time correction ranges from 0.9892 ± 0.0001 for the highest signal rate, to 0.99496 ± 0.00006 for the least. The correction applied to the most recent data (15mm/10.5mm collimation, 30μg-H3 target, warm beryllium filter cryostat) is 0.99375 ± 0.00007.

7.2 Charged Particle Dynamics

Charged particles have a non-zero probability of transmitting through matter. During their transit they ionize the target material and lose energy mainly to electrons [61] [62]. The rate of energy loss is both target-dependent and initial energy-dependent, where both a lighter target in Z or a higher-energy alpha induce a lower rate of energy loss per distance traveled. The source used in the Alpha-Gamma experiment is comprised primarily of ^{239}Pu, which emits ∼5.156 MeV α particles. Small ^{240}Pu and ^{241}Am impurities emit higher energy alphas as well; since the energy scale of decay particles in both isotopes of Pu is about the same, contributions from both decays are measured.

The most important component of the low solid angle counting stack is the nickel-coated diamond-turned copper aperture. The diameter is measured by a coordinate measuring machine to be $D_{\text{ap}} = (25.76519 \pm 0.00024)$ mm. The feature which defines this aperture is the inner 90° edge, which is ground flat. The source-facing bevel is designed to reduce scattering from decay alphas, leaving a thin ~ 0.5 mm cylindrical edge on the inner diameter. While the transmission distance through the aperture is small, there is a region close to the 90° edge where this is possible. Transmitted alphas deposit a majority of their energy near the end of their range (see Fig. 7.5), which contributes non-uniformly to the background. For this reason, the transmitted portion of the alpha flux is simulated using MCNPx. This results in an effective aperture diameter of $D_{\text{ap eff}} = (25.76694 \pm 0.00058)$ mm which is slightly wider than measured, as expected. The source to aperture distance of the counting stack is measured using the metrology microscope to be $z = 87.4176 \pm 0.0018$ mm. The diameter of the ^{239}Pu spot was measured to be $D_{source} = 0.906 \pm 0.008$ mm.

Alpha particles are emitted isotropically from the ^{239}Pu source. They lose energy as they traverse the silicon substrate upon which the source is deposited. Rutherford backscattering is an elastic effect [65]. Since the particles are incident upon Si atoms with both an arbitrary

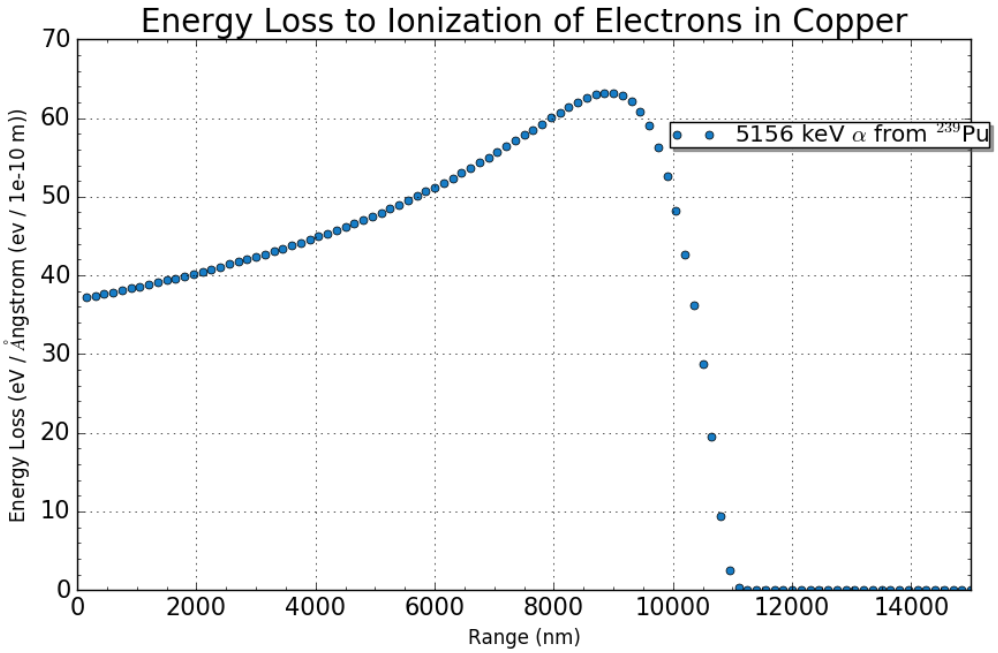

Figure 7.5: A SRIM calculation of the energy loss due to ionization of 5.156 MeV alpha particles during transit through copper. A small portion (not shown here) is lost to the creation of phonons as well, but only at the end of the stopping length of the particle.

angle and energy, the backscattered alphas are similarly scattered with an arbitrary angle and energy. The contribution to the measured rate therefore contains a flat background at all energies up to peak energy due to Rutherford backscattering. The backscattered alphas incident upon the aperture will transmit just like those at peak energy, but through a smaller region and with a flatter spectrum upon exit (like the spectra used in proton therapy [62]).

The charged particles counted to measure the absolute activity exclude the backscattered fraction so that the contribution to the activity measured comes only from the alpha particles emitted forward with their full energy. The flat region in the Pu counting spectrum (see Fig. 4.15) corresponds to alphas of $\sim 1-2$ MeV. Considering all of these factors, the solid angle of the counting stack is measured to be $\Omega_{stack} = 0.0053404 \pm 0.0000008$ as a fraction of 4π. This yielded an absolute source rate of $2190.7 \pm 0.7 \mathrm{s}^{-1}$. The full methodology

applied to the measurement and calculation of the activity is described in A. Yue's thesis, Appendix B [51].

7.3 Corrections to the Alpha-Gamma Alpha Counting Data

In order to accurately measure the absolute number of neutrons in the beam, proper accounting of a number of nonideal experimental constraints is required. The solid angle subtended by the AG Si detector for the NG-6m neutron beam differs from the ^{239}Pu measured solid angle. There is a small difference in penetration depth through the solid angle defining aperture for the ~ 5 MeV ^{239}Pu decay alphas and the $\sim 1.5 - 1.9$ MeV neutron absorption alphas.

7.3.1 Alpha-Gamma Neutron Beam Spot Size

The ^{239}Pu source used to measure the solid angle subtended by the AG Si detector is a uniform spot between 1 and 3 mm in diameter depending on the source chosen. The NG-6m neutron beam casts an elliptical spot onto the inclined Alpha-Gamma target surface. The thin ^{10}B target is nonuniform across its surface, whereas the thick target is sufficient to absorb the whole beam which means its absorption is uniform. Correcting this effect requires measurement of the difference between the solid angle presented by the AG target center as determined by ^{239}Pu counting and the neutron beam, the variation in thickness of ^{10}B across the thin target, and the beam intensity profile.

The aperture masking the Alpha-Gamma Si detector is measured by a coordinate measuring machine to be 27.598 ± 0.006mm in diameter. The distance between the target holder and the Si detector is determined using the ^{239}Pu source, whose absolute activity is measured in a previous step. Since the proportion of total decay alphas detected in the Si detector is equal to the proportion of 4π subtended by the Si detector, and the aperture

Table 7.2: Corrections to the measured efficiency for the solid angle source calibration of the Alpha-Gamma alpha detector.

C1 and Year	$\Xi(0,0) / \int \rho(x,y)$
7, 8, 10 2010 - 2011	0.0071544 ± 0.0000020
10, 2012	0.00716685 ± 0.0000025
10, 2014-2015	0.00710283 ± 0.0000036

diameter is well known, the separation from the target center is the distance required to achieve that solid angle.

The difference in the solid angle subtended by the detector for the target center as measured using the ^{239}Pu source and as seen by the emitted alpha particles from neutron absorption in ^{10}B is calculated using the known aperture geometry during the determination of the precise distance between the source and the Si detector. The mask material (6061-T6 Aluminum) is entered into an MCNPx simulation. Due to the greater penetration depth of 5.156 MeV alpha particles, the effective diameter of the aluminum aperture for ^{239}Pu is $D_{AG,Pu} = 27.603 \pm 0.006$ mm. Comparing the measured rate of the ^{239}Pu source in the low solid angle counting stack and the rate in the Alpha Gamma apparatus yields the source to aperture distance z_{AG}, which can be used to correct for the solid angle subtended by the neutron beam in the Alpha-Gamma geometry. The magnitude of the correction changes in the event that some facet of the target holder / detector geometry changes. The most common cause for such a change is a detector failure. Replacement of the charged particle detector in Alpha-Gamma disturbs the precise distance between the target center and the aperture. As a multiplicative correction to the data, the solid angle source calibration is reported in Table 7.2. This is used to correct the measured ^{10}B alpha rate r_{AG} to the absolute number of alphas emitted into 4π.

The neutron beam intensity profile is measured by a dysprosium activation method. ^{164}Dy has a neutron capture cross section of $\sim$ 7500 barns at the NG-6m beam wavelength

of 0.496 nm [66]. When a neutron is captured via this channel, it enters one of two unstable energy states: the short-lived metastable state ^{165m}Dy with a 1.257 minute half life, or the ground state of ^{165}Dy with a beta decay half life of 2.334 hours. ^{165m}Dy is most likely to decay by an isomeric transition (IT) to ^{165}Dy, which then decays by beta emission to ^{165}Ho. By exposing a disk of dysprosium held in the Alpha-Gamma target holder to the neutron beam, a beta intensity map can be produced which is proportional to the neutron beam intensity.

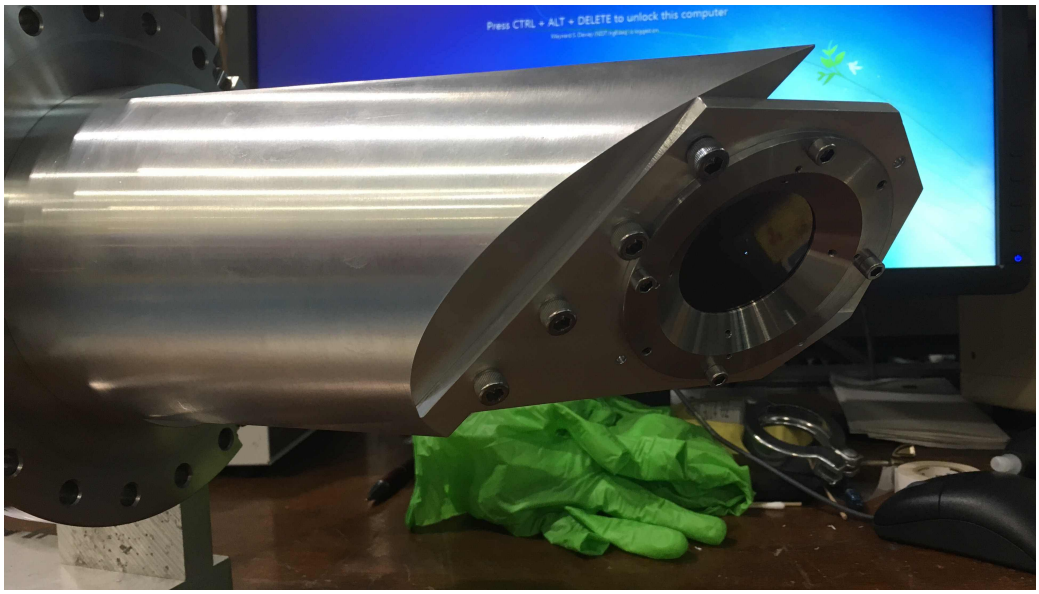

Figure 7.6: The dysprosium disk is held at the Alpha-Gamma target center by the same fixtures which hold the ^{10}B thin target. The center hole is faintly visible. Some portion of the side of the center hole is irradiated, which will not affect the calculations.

The dysprosium disk has the same transverse dimensions as the thin ^{10}B target and is thick enough to be self-supporting. A 1 mm diameter hole located precisely at the center of the disk produces a region of low intensity which can be used to find the target center in calculation. As the disk is exposed to neutrons, it builds up activity until the decay rate of ^{165}Dy is proportional to the neutron capture rate. Then the neutron beam is shut and the short-lived ^{165m}Dy state decays.

A Fuji Imaging Plate stores energy from beta decay using a proprietary set of phosphor

compounds. A specially-designed scanner (most recently the Typhoon 7000 by General Electric) induces fluorescence in the phosphor imaging plate directly proportional to the energy stored. This is recorded optically as the plate is scanned to produce a neutron intensity map of the beam at the location and orientation of the thin target. Slight smearing of the image can occur due to the width of the scanning laser or the scintillation time of the imaging plate. With the newer instruments, this effect is negligible.

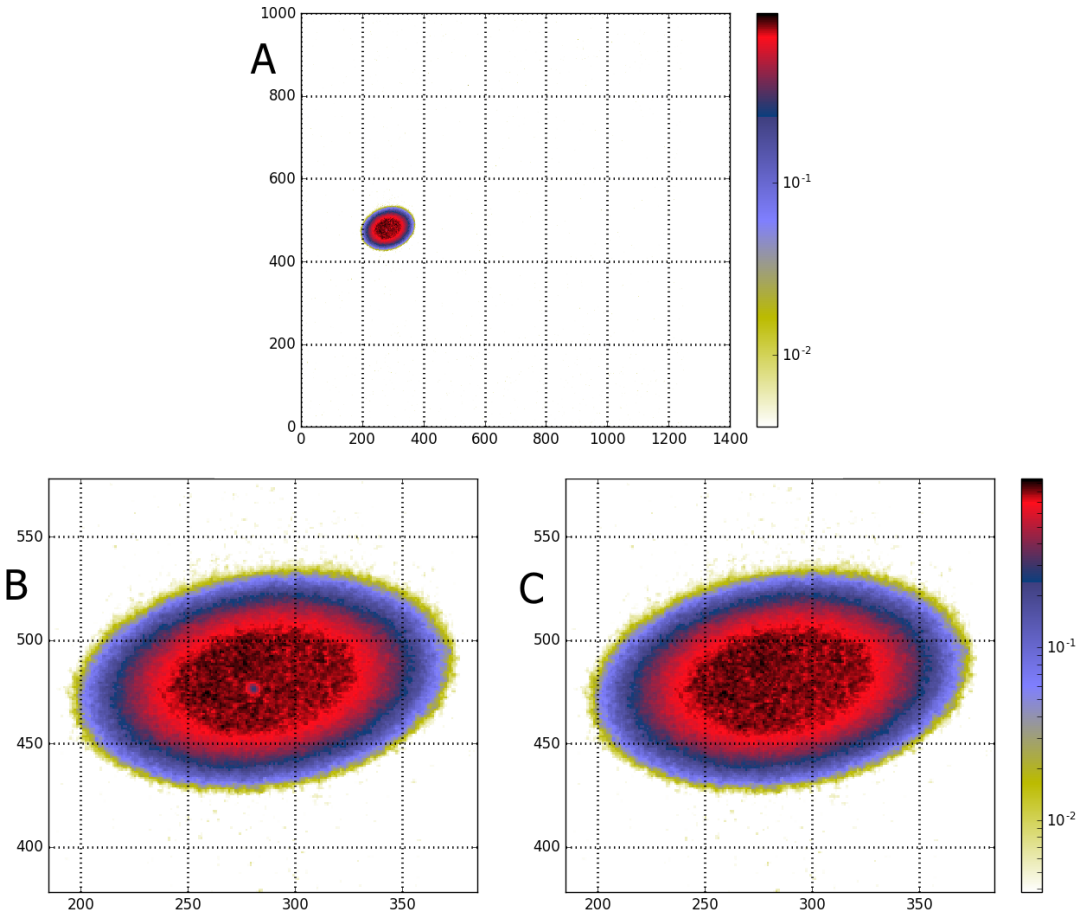

Figure 7.7: Various stages of image plate data processing of a 30-H3 Dy beam image at C1= 15 mm, C2= 10.5 mm . A: the raw output. B: zooming in on the beam spot. C: background removal and filling the center hole. Axes are pixels. Each pixel is 0.2×0.2 mm on the detector surface. Note that the off-axis target center position is clearly visible in Image B as the hole.

Neutron beam images must be processed to fill the hole in the Dy disk and to remove

background. This has been done in several ways, most recently in Python 3.4 using the NumPy stack (see Fig. 7.7). The hole is filled by sampling the surrounding region of the image, determining its average value and standard deviation, and applying a random value to each of the hole center pixels. Background is removed by sampling the image sufficiently far from the beam region, averaging, and applying a uniform subtraction rather than a random one. Before calculating the solid angle, the target to detector distance must be determined.

Since the Dy disk is a totally-absorbing material, and the thin ^{10}B is not, information about the ^{10}B deposit thickness must be incorporated into the solid angle calculation. The deposit areal density is given by:

$$\rho(x,y) = \bar{\rho}\frac{1-(1-0.995)\left(\frac{\left(x^2+y^2\right)^{1/2}}{19}\right)^2}{1-\frac{0.005}{2}} \tag{7.7}$$

The beam spot may not be centered with respect to the deposit profile, so these two effects must be convolved in the calculation of the average solid angle $\bar{\Omega}$

$$\bar{\Omega} = \int\int \Omega(x,y)\,\Xi(x,y)\,dxdy \tag{7.8}$$

$$\Xi(x,y) = \frac{I(x,y)\,\rho(x,y)}{\int\int I(x',y')\,\rho(x',y')\,dx'dy'} \tag{7.9}$$

where $I(x,y)$ and $\Omega(x,y)$ are the beam intensity and solid angle at a given point on the target surface. $\Xi(x,y)$ expresses the number of charged particle events produced at a given point as a fraction of the total number of events (or, put another way, the intensity at a given point on the target surface as a fraction of the total intensity). The solid angle at each point is calculated using the expression described in J. Richardson's thesis, Appendix

Table 7.3: The corrections to the measurement of the FM efficiency ϵ_0 can change over time. Effects which require re-measurement include changes in collimation and target holder fixtures, but also more dramatic occurrences (such as the August 2011 Virginia earthquake).

Year	Config (C2, $\rho\,(\mu)/\mathrm{cm}^2$)	Correction
2010	(7, 40-τ_n)	0.99215 ± 0.00004
2010	(8, 40-τ_n)	0.98968 ± 0.00004
2010-2011	(10, 40-τ_n / 30-H5 / 20)	0.98589 ± 0.00005
2012	(10, 20)	0.98587 ± 0.00005
2014-2015	(10, 30-H5 / 30-H3)	0.985998 ± 0.000009

C [54] with additional terms in the expansion computed by A. Yue. The uncertainty is determined by taking several sets of beam images and calculating the standard deviation, divided by the square root of the number of images. When multiple images are not available, an upper-limit is derived by taking the maximum spread in values from similar calculations (all of those with 15 mm and 10.5 mm collimation, for instance). To correct the average solid angle to the infinitely-narrow beam, the multiplicative correction to the FM efficiency for the AG target solid angle is $\Omega\,(0,0)\,/\bar{\Omega}$ (s).

7.3.2 Alpha Particle Backscatter

Alpha particles from the ^{10}B neutron reaction have a small probability of backscatter off of the surface of the silicon charged particle detector. The effect on the charged particle counting during other phases of the experiment is subsumed into the measurement technique and therefore safely ignored. But to determine the total number of neutron events entering the $^{10}\mathrm{B}(\mathrm{n},\alpha)^7\mathrm{Li}$ channel, the fraction of charged particles which are not detected must be known. This is simulated using TRIM [67]. Since alphas can partially deposit their energy, they may still be detected above threshold in the SCAs. Given the input energy E_i and the simulated outgoing energy E_t (part of TRIM's backscatter output), the energy deposited

by each backscattered ion is calculated as $\Delta E = E_i - E_f$. If this is above threshold the particle is not included in the correction as a loss.

Only 93.7% of the incoming alpha particles are associated with an emitted gamma. 6.3% of the alphas have more energy, and therefore a higher likelihood of being counted. This is taken into account when determining the number of alphas counted. The multiplicative correction to the measured FM efficiency from this effect is 0.999979 $\pm$0.000005.

7.3.3 Neutron Production from Thermal Neutron Capture

There exists a small cross section for charged-particle-induced MeV neutron production [68] in neutron-absorbing materials such as the ^{6}LiF-loaded polyethylene flag used in the modulation of the NG-6m beam. When the flag is out, neutrons pass uninhibited through the apparatus. When the flag is in, the full beam is absorbed, mainly by ^{6}Li. If there is some MeV neutron production due to absorption on ^{6}Li, it can generate a beam-dependent change in the background of the Flux Monitor which would not be seen in other auxiliary measurements.

The reaction rate for fast neutron production in a totally-absorbing target of ^{6}LiF is 10^{-4} per incident thermal neutron. Both the $^{10}\mathrm{B}(\mathrm{n},\alpha)^7\mathrm{Li}$ and the $^6\mathrm{Li}(\mathrm{n},t)\alpha$ cross sections for the fast neutrons emitted from this system (tens of keV - MeV) are $\sim 10^{-3}$ - $\sim 10^{-5}$ that of the $\sim$ 0.5nm neutrons comprising beamline NG-6m [36]. This amounts to a charged particle detection rate in the Alpha-Gamma and FM alpha detectors of $10^{-7} - 10^{-9}$ of the beam-on detection rate if all of the neutrons produced are forward-emitted (a worst-case scenario since they are instead emitted isotropically). Since a majority of these neutrons are emitted at MeV energies, the enhancement due to this effect is closer to a 10^{-9} correction, and therefore negligible.

During the thick target measurement the full beam is absorbed in ^{10}B and does not reach

the beamstop which makes this effect a concern. Only about 5% of the fast neutrons are absorbed in the thick target, and the α_0/α_1 branching ratio shifts from 0.0705 to between 0.4 and 3 at incident neutron energies above 0.5 MeV [69]. This means that any neutrons absorbed are about 1/4 as likely to produce a 478 keV gamma ray. Since any fast neutrons produced due to interaction in the ^{6}LiF are emitted into 4π, the effect is suppressed by $1/r^2$. The fractional solid angle subtended by the target for the lithium flag is $\sim$ 1.5E-4. The effect is therefore suppressed by a factor of 2E-9. During the thin target measurement, when the neutron beam is not absorbed by the upstream ^{6}LiF polyethylene flag, it is absorbed downstream by the same material. Therefore any addition to the background in the HPGe detectors due to direct deposit of energy from fast neutrons produced by this effect is present in both beam states. Neutrons will not deposit energy precisely within the 478 keV region of interest as they would if they were absorbed in either of the target deposits. The contribution to the background is instead spread across a broad spectrum which is small as compared to the rest of the backgrounds in the HPGe detectors.

7.4 Corrections to the Alpha-Gamma Gamma Counting Data

Exposure of the thin ^{10}B Si substrate to the neutron beam induces a gamma background that is not present in thick target data. The same Si substrate attenuates 478 keV gammas from $^{10}\mathrm{B}(n,\alpha)^{7\mathrm{m}}\mathrm{Li}$ in thin target data only. Gamma rays are attenuated in transit to both the top and the bottom gamma detectors due to the penetration of neutrons into the $^{10}\mathrm{B}_4\mathrm{C}$ disk before absorption.

7.4.1 Gamma Production in Si Substrate

By design only a small fraction ($\sim$ %1) of the neutron beam is absorbed in the thin ^{10}B target. The remaining neutrons propagate through the silicon substrate, which will produce

a gamma background via neutron absorption. The Si(n, γ) cross section for the NG-6m beam energy of $\sim$ 3.33 meV is a paltry $\sim$ 0.5 b. However the background is only present during the thin target measurement (there is no Si backing for the self-supporting thick $^{10}B_4C$ target). The gamma ray cascade from neutron capture on natural silicon consists mostly of higher-energy gammas [70], but these can partially deposit energy into the HPGe crystal by Compton scattering, and therefore represent a beam-dependent background. This effect is investigated by observing the signal in our region of interest with a blank (no target deposit) silicon wafer of identical thickness to the one used as a target substrate. Since the gamma production is flux-dependent, the Si blank count rate is compared to the ^{10}B thin target count rate using the upstream Flux Monitor as a proportional counter; it is excellent in this capacity even if its efficiency is not well known. The quantity measured for this comparison is therefore $\gamma/FM_{\alpha,t}$.

Since the Si gammas are emitted from nearly the same locations as the ^{10}B gammas, and the areal density is directly proportional to that of the neutron beam, the measurement of this effect is first-order independent of beam size, shape and intensity. This means that data from all collimation states and all ^{6}Li targets can be combined. The most recent thin target measurement is used for comparison. Since the effect is small, the Si measurement is not book-ended by ^{10}B thin target measurements. There is therefore a small drift in the HPGe gamma detector gain which remains unaccounted for. Data are combined using an arithmetic mean weighted by the inverse of the square of the uncertainty.

Improved precision of the measurement can be achieved by book-ending the silicon blank measurements, and modeling the Si gamma fraction for different beam shapes (different C2 collimations). The probability of Compton scatter, either within or into the detector, may have some beam shape dependence. However the probability of 478 keV gamma detection from ^{10}B will have roughly the same proportional dependence as the probability of Compton

Table 7.4: Silicon Blank Contributions to the 478 keV Spectrum (% of combined total)

Data Set	% Top HPGe signal[1]	% Bottom HPGe signal[1]
S061.0010 / 11	$0.01155190 \pm 0.00025945$	$0.01241693 \pm 0.00025522$
S062.0006 / 07	$0.01202485 \pm 0.00019759$	$0.01239455 \pm 0.00019501$
S062.0013 / 14	$0.01195212 \pm 0.00028530$	$0.01219437 \pm 0.00028600$
S065.0003 / 04	$0.01224607 \pm 0.00048167$	$0.01313261 \pm 0.00047710$
S069.0003 / 04	$0.01115423 \pm 0.00048248$	N/A
S076.0015 / 16	$0.01206642 \pm 0.00020456$	N/A
S103.0036 / 104.0001	$0.01120409 \pm 0.00038372$	$0.01235865 \pm 0.00037120$
Mean	$0.01185877 \pm 0.00010423$	$0.01240795 \pm 0.00012354$
Correction	$0.98814123 \pm 0.00010423$	$0.98759205 \pm 0.00012354$

[1] Extra significant figures are included for comparison to future calculations of the silicon gamma contribution.

scatter within the detector (neglecting secondary Compton scatters). Therefore the only systematic effect will be from gammas which scatter off of the apparatus (vacuum system, lead shielding etc.) into the detector.

7.4.2 Gamma Attenuation in the Thin Target Substrate

Gamma rays from neutron absorption in the thin ^{10}B target which are emitted towards the top HPGe gamma detector will pass through the 0.4 mm silicon substrate, whereas those absorbed by the thick ^{10}B target will not ($^{10}B_4C$ attenuation is discussed later). In order for the gamma detector efficiency measurement with the thin ^{10}B to be meaningful, a correction must be applied to mitigate this effect. Modeling the attenuation using a beam simulation and XCOM [71] shows about 1% of the beam is scattered in the Si backing. In order to measure the effect to sufficient precision, 0.4 mm thick silicon wafers are stacked behind the thick ^{10}B target, and the difference in the FM-normalized rate in the top gamma detector $\left(\frac{r_\gamma(thick)}{r_{FM}}\right)$ is observed. Measurements were performed with 0, 3, and 5 silicon wafers (see Fig. 7.8). Since the attenuation is small, a linear extrapolation to 0 wafer backings is

sufficient. This amounts to a correction factor of 1.01297 ± 0.00079 to the top gamma detector data.

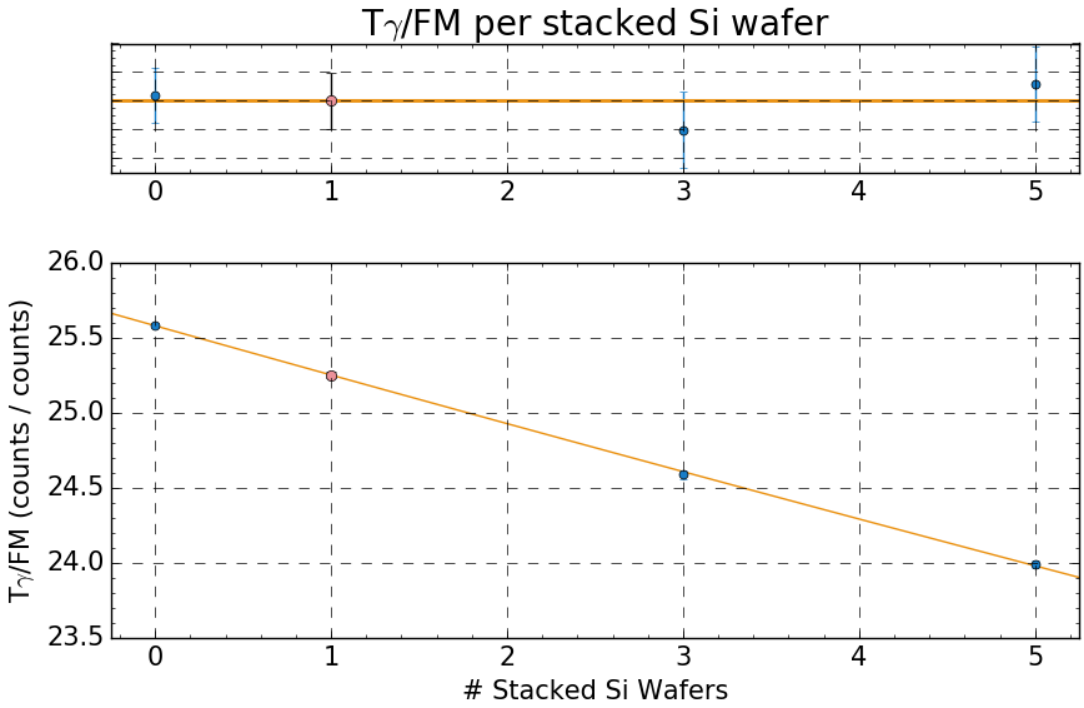

Figure 7.8: The Top HPGe detector thick target rate per Flux Monitor rate as a function of the number of Si substrates stacked behind the thick target. The thin target data are corrected to an effective "no Si substrate" value at $x = 0$ based on the fit. The lighter colored pink data point at $x = 1$ and its error bars are calculated from the fitted curve.

7.4.3 Gamma Attenuation in the Thick Target

The $^{10}B_4C$ comprising the thick target scatters gamma rays produced from neutron absorption on ^{10}B, causing gamma rate signal loss. Since neutrons are absorbed in the first few micrometers of the target, the magnitude of the scattering is greater for the top gamma detector. The variation in neutron penetration depth results in a range of different path lengths through the target for gamma rays detected in the HPGe detectors. An MCNP simulation described the average penetration depth prior to absorption and recorded the final location of each neutron. The average path length of a gamma ray through the $^{10}B_4C$

before detection can be calculated from this: for the ~ 0.31 mm thick target the average path length was 0.036 mm to the bottom gamma detector, and 0.547 mm to the top gamma detector. It is unsurprising that the path length to the top gamma detector is thicker than the target since the target holder is set at an angle to both the beam and the axis of the gamma detectors. While this geometry is not easily changed to interpose more $^{10}B_4C$ between the absorption site and the bottom detector, it is easy enough to do so for the top detector using one or both of the thick targets.

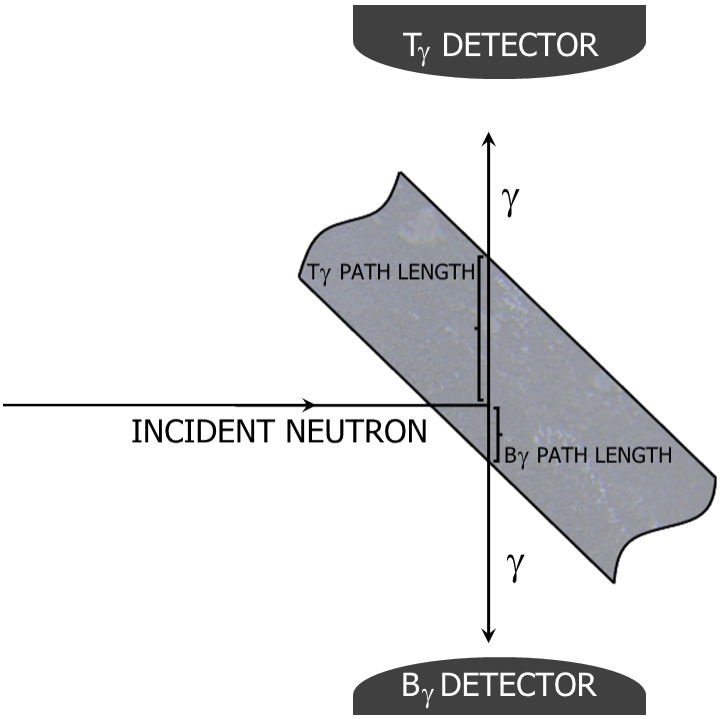

Figure 7.9: A qualitative model of the neutron absorption and subsequent propagation of 478 keV gamma rays through the thick $^{10}B_4C$ target.

Recall that two totally absorbing thick targets were produced with two different thicknesses: 0.31 mm (labeled 0.32 mm) and 0.56 mm. By placing the targets alone or in combination into the AG target holder, three different thicknesses of $^{10}B_4C$ target can be created. The thickness of each target was measured at multiple points by NIST metrologist John Stoup (test results labeled Test No. 683/xxxxxx-13). For the calculation the thickness was chosen to be the arithmetic mean of the measurements with an uncertainty of 1/2 the

difference of the smallest and the largest measurement (thus incorporating all measured values). This results in the thicknesses listed in Table 7.5.

Table 7.5: Measured thickness of the $^{10}B_4C$ totally-absorbing black targets. Each target was measured in 27 different locations. They can be used individually, or stacked to form a third target thickness.

Target Thicknesses (mm)
0.314 ± 0.0047
0.563 ± 0.0050
0.877 ± 0.0068

The thick target gamma rate is then measured as a fraction of the upstream FM rate, and plotted as a function of target thickness(see Fig. 7.10). The correction factor is then written as the fractional difference between the "0 target thickness" loss-rate, and the loss-rate for the thickness traversed as determined using MCNP. This results in a multiplicative correction to the data of 0.98943 ± 0.00044 for the top HPGe detector, and 0.99934 ± 0.00003 for the bottom detector.

7.4.4 Neutron Loss in the Thick Target

The assertion that measurement using the thick target measures the absolute flux of neutrons in the neutron beam requires quantification of any neutron interaction that does not result in absorption by ^{10}B. Note that this is not required of the thin ^{10}B target because its purpose is only to determine the efficiency of the gamma detectors to detect neutron absorption via the $^{10}B(n,\alpha)^7Li$ channel. Most of neutron loss in the thick target is caused by neutron capture on ^{10}B via the $^{10}B(n,\gamma)^{11}B$ reaction. The next most important loss comes from neutron scattering effects.

All effects which induce scattering further into the target are diminished since neutrons are highly likely to be absorbed by adjacent ^{10}B rather than escape the experiment undetected. In large part for this reason the effects should be measured. $^{10}B_4C$ is a ceramic, and

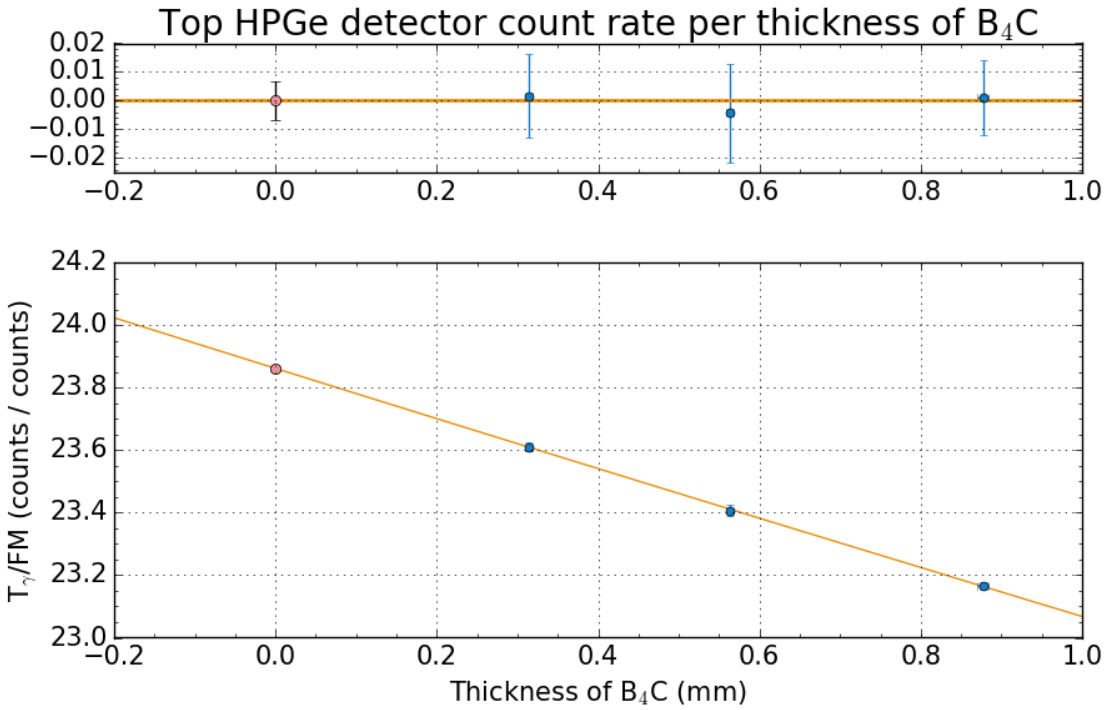

Figure 7.10: The fractional thick target rate as a function of target thickness. The data are corrected to an effective "0 target thickness" at $x = 0$. Uncertainty in the thickness measurement is occluded by the data points.

therefore likely to form crystallites throughout the disk which Bragg scatter. The effect was measured using powder diffraction techniques and the thicker thick target on the SPINS instrument at the NCNR. A single peak corresponding to the (101) peak was measured, into which a negligible 2×10^{-7} fraction of the neutron beam was scattered (see Fig. 7.11). The loss factor is further reduced due to the scattering angle, which is likely to result in scatter further into the target.

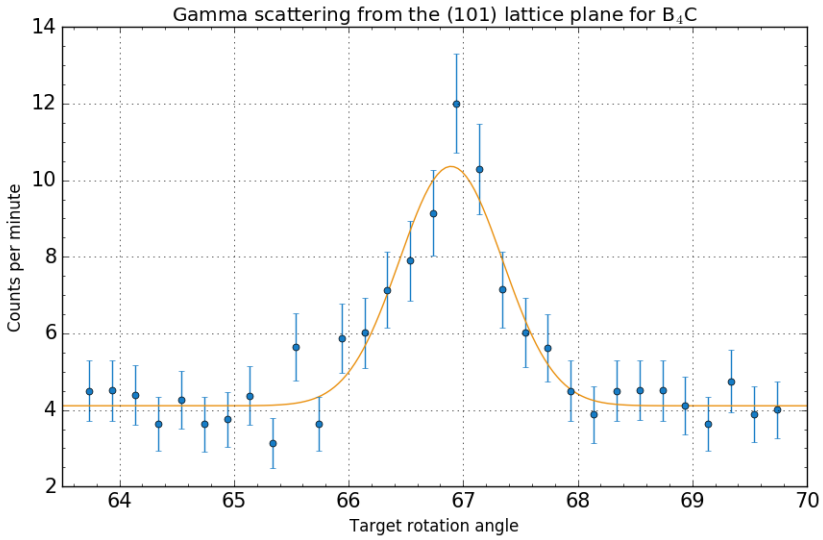

Figure 7.11: The measured Bragg scattering from the (101) lattice plane of $^{10}B_4C$ in the thick ^{10}B target.

Incoherent scattering from the thick target occurs primarily due to the ^{10}B, whereas both incoherent scattering and absorption from the rest of the isotopes present in the material do not contribute significantly (see Table 7.6). Since much of the scattering will occur at some small depth into the target, the loss rate of neutrons due to this effect is difficult to calculate. An MCNP simulation is used. 0.006% of the incident neutrons are lost due to incoherent scattering, which results in a multiplicative correction to the measured FM efficiency of 0.9999405 ± 0.0000003.

Backscatter from the surface of the thick target can result in direct neutron loss. Two techniques were used to assess this loss. A dysprosium disk is placed near the Alpha-Gamma

Table 7.6: Incoherent scattering and absorption cross sections for the atoms comprising the thick target. The relative concentration is given in terms of the number density. The absorption cross section is given for $\lambda = .496$ nm neutrons.

Isotope	Rel. Concentration	σ_{inc} (b)	σ_{abs} (b)
^{10}B	0.784	3	10578±25
^{11}B	0.016	0.21	0.15
^{12}C	0.198	0	0.00974
^{13}C	0.0022	0.034	0.00378

Si charged particle detector. Any backscattered neutrons have a chance of scattering into the Dy disk, which is then analyzed using the same dysprosium imaging technique as in Sec. 7.3.1. The thick target (with the Dy disk in place) was exposed to the beam for 1 hour, and the Dy disk to the imaging plate for 15m. No counts were measured above background. The second technique relied on a difference measurement between the upstream Flux Monitor and the Alpha-Gamma Si detector. A thin ^{10}B target was placed in both the AG and FM target holders. The higher reaction rate of ^{10}B over ^{6}Li helped to accumulate higher statistics from the FM. The 0.31 mm thick target was then placed behind the AG target holder. The presence of the Si substrate blocks charged particles coming from the thick target. If any scattering effects resulted in neutron scatter towards the thin ^{10}B target, a higher $r_{\alpha(thin)}/r_{FM}$ relative count rate would be observed with respect to the same setup without the thick target. The observed fractional count rate of $(-4 \pm 6) \times 10^{-4}$ is consistent with zero. While it is true that neutrons could be scattered all the way up to the FM, the relative solid angle for FM versus AG capture is small.

Neutrons absorbed via the $^{10}\mathrm{B}(\mathrm{n},\gamma)^{11}\mathrm{B}$ reaction emit gamma rays of much higher energy ($\sim 4-10$ MeV) than the 478 keV signal gamma. While these can Compton scatter just like the Si capture gammas, they are present in equal fraction during the thin target data taking; therefore, Compton scattered radiative capture gammas which deposit energy within the 478 keV window are naturally incorporated into the gamma detector calibration. What is

not accounted for is the neutron loss due to this channel. The correction is easily calculated using the measured cross section for the $^{10}\mathrm{B}(\mathrm{n},\gamma)^{11}\mathrm{B}$ [72], [73], [74]. Taking a weighted mean of the cross section and comparing it to the $^{10}\mathrm{B}(\mathrm{n},\gamma)^{7}\mathrm{Li}$ cross section, it is seen that radiative capture absorbs $0.00010 \pm 0.000004\%$ of the neutrons. This results in a multiplicative correction to the measured Flux Monitor efficiency of 0.99990 ± 0.000004.

7.5 Corrections to the Flux Monitor Data

We refer the neutron detection efficiency of the flux monitor to a standardized neutron beam phase space incident upon a standardized target: an infinitely thin thermal (2200 m/s) neutron beam normally incident upon the center of an infinitely thin, perfectly uniform target of $^{6}\mathrm{Li}$. This choice of reference condition requires a number of corrections both for geometry and for target characteristics.

7.5.1 Flux Monitor Neutron Beam Spot Size and Alignment

Misalignment of the FM manifests as a deviation in the transverse position of the target center from the beam center, and as a tilt of the target normal away from the incident beam. A shift in the target center position is instead parameterized as a shift off-axis of the incident neutron beam. Several systematic corrections arise from this shift: the solid angle subtended by the FM detectors for a wide, off-axis neutron beam is smaller than an infinitely thin on-axis beam, and the $^{6}\mathrm{Li}$ target areal density variations over its profile means that incident neutrons which are off-center are less likely to be absorbed and subsequently emit charged particles than those that are on-center. Recall from Eqn. (2.14) the terms within the integral: since the beam is monochromatic with only a very small $\lambda/2$ contribution, $\phi\,(x,y)$ is a function of the beam intensity $I\,(x,y)$ only, and not the convolution of intensity and wavelength.

The extended-beam solid angle $\Omega(x,y)$ is corrected to the solid angle for an infinitely thin beam incident upon the center of the target, $\Omega(0,0)$ by the same Dy imaging methodology described in Sec. 7.3.1. As discussed earlier, this correction is necessary to parameterize the efficiency in the same way that it is written for the in-beam neutron lifetime experiment. It is also a prudent choice for expression in terms of a generally-portable efficiency. For the C1/C2 = 15/10.5 mm configuration, the average solid angle is $\bar{\Omega}_{FM} = 0.00419865$ and the correction $\Omega_{FM}(0,0)/\bar{\Omega}_{FM} = 1.00077 \pm 0.00002$.

In addition to the correction for the average solid angle $\bar{\Omega}_{FM}$, the difference between $\rho(beam)$, the mean density of the target deposit over the beam profile, and $\rho(0,0)$ must be accounted for. Recall Eqns. (7.8) and (7.9): the calculation reports an average solid angle and a correction in terms of $\rho(x,y)$ as well as a correction to $\Omega(0,0)$. This handles the change in solid angle from the extended beam to the point-like beam, but not the change in areal density. The ideal beam is incident entirely upon the center of the target. For the same number of neutrons, the reaction rate is lower for the extended beam than the ideal beam. To first order, the change in reaction rate is linear in ρ. The correction to the measured Flux Monitor efficiency ϵ_{FM} to calculate ϵ_0 is then $\rho(0,0)/\int\int \rho(x,y)\,\phi(x,y)$. The term is alignment- and collimation-dependent (See Table 7.7).

Table 7.7: The correction for each collimation where C1 = 15mm and C2 is as given.

C1 and Year	$\rho(0,0)/\int\int \rho(x,y)\,\phi(x,y)$
7, 2010	1.00011 ± 0.00001
8, 2010	1.00015 ± 0.00001
7, 8, 10, 2010-2012	1.000218 ± 0.00001
10, 2014-2015	1.000234 ± 0.00001

Tilt of the FM such that the beam is not normal to the ^{6}Li target surface causes incident neutrons to travel through more of the ^{6}LiF target deposit, increasing the apparent areal density and therefore the likelihood of neutron detection. This effect artificially inflates the

count rate in the FM and produces an erroneously high efficiency. Direct measurement of the tilt angle is necessary to correct for this effect.

The tilt is measured using the theodolite during apparatus alignment. The positions of the FM cross-hairs described in Sec. 4.1 are measured using the vertical and horizontal displacements with respect to the theodolite-determined beamline, and the distance from the theodolite to one set of cross-hairs. The distance to the other set is constrained by the geometry of the FM cross-hair device. The line drawn between the two cross-hairs is used to describe the vector through the FM with respect to the beam. The correction is simply the longitudinal component of the vector (see Table 7.8). Uncertainty is determined by repeatedly lifting and re-seating the FM to observe changes in cross-hair positions. Vacuum pressure causes a negligible shift in the angle of about 0.0322°.

Table 7.8: FM tilt angles and corrections for previous and future measurements. The correction given is multiplicative.

Vacuum Cylinder and Rig #	Tilt Angle (deg)	ϵ_{FM} Correction
Long, Rig #1	0.37736	0.999978 ±0.000002
Short, Rig #2	1.05138	0.999832 ±0.000002
New Kinematic System		
Rig #2	0.000000	1.0000000 ±0.0000002[1]

[1] Note improved uncertainty. This is due only to apparatus flexure under vacuum.

7.5.2 Neutron Scattering in the Si Substrate

Two effects result from the presence of the Si substrate upon which the ^{6}Li target is deposited. Neutrons in the beam are attenuated by scatter and absorption, reducing the observed neutron rate for downstream Alpha-Gamma apparatus. An experiment was performed at the IRMM to quantify the effect during the 1990-2000 in-beam neutron lifetime effort [1]. The beam-to-FM geometry used was identical to that of Alpha-Gamma, with

the absorption deposit (^{10}B in this case) facing the incoming beam. Approximately half of the scattered neutrons are reflected back through the deposit, which can enhance the observed neutron rate in the Flux Monitor. Those scattered at an angle with respect to the initial trajectory see a greater thickness of absorber and therefore an increased likelihood of absorption. The relevant parameters for this effect are the probability of scattering from a single wafer ϵ_{sca}, and the signal enhancement $f(i)$ experienced as a result of neutron scatter back through the target. The rate in the Flux Monitor is then:

$$r_{\alpha,\mathrm{FM}} = a\left(1 + \frac{f(i)}{2} i\epsilon_{sca}\right) \tag{7.10}$$

where a is a fitting parameter, and $f(i)$ is calculated using a Monte Carlo program and the geometry for each set of stacked wafers. The experiment found that ϵ_{sca} was much larger than expected from only incoherent and Bragg scattering from perfect crystal Si. While the mechanism is not well-understood, a plausible explanation is that neutrons are scattering off of the polished deposition surface, which may have experienced mechanical stress, or a polycrystalline SiO_2 layer, which would induce greater Bragg scattering.

At the Indiana University Center for the Exploration of Energy and Matter (CEEM) Low Energy Neutron Source (LENS) SANS we performed neutron scattering on silicon wafers whose surfaces we had dissolved using a solution of hydrofluoric acid buffered with nitric acid. Perfect silicon crystal does not etch isotropically for most acids. HF acid is capable of dissolving the otherwise inert silicon oxide layer in all orientations. HNO_3 readily oxidizes silicon. Together, they quickly remove the first several nm of the silicon crystal surface. Scanning Electron Microscopy (SEM) and Atomic Force Microscopy (AFM) showed that the dissolved surface was smooth to within the limits of the instruments ($\sim$ 1 nm). The reaction was more vigorous than we had anticipated, but the AFM and SEM images showed that it did not affect wafer smoothness. For 15 etched wafers measured perfect crystal silicon total

cross section disagreed with that measured by Freund [53] by a factor of 15, and was higher than the powdered silicon cross section at all measured energies. The measured neutron total cross section for natural silicon according to ENDF/B-VI EXFOR [75] is multi-modal. Unfortunately most of it is unpublished, so it is difficult to know why the modality might occur. It is therefore necessary to directly measure the effect of the silicon wafer substrate on the calibration.

In order to quantify the effect of the silicon substrate on the Alpha-Gamma calibration setup, a second experiment similar to the IRMM experiment was performed in situ. Two ^{10}B targets of $\sim 100\mu\text{g/cm}^2$ were used, one in the FM, and one in AG. The neutron loss per Si wafer η_{si} downstream is the sum of losses due to scatter and absorption in Si:

$$\eta_{si} = \epsilon_{sca} + \epsilon_{abs} \tag{7.11}$$

where $\epsilon_{abs} = 0.0009$ is the neutron absorption probability in silicon [36]. The ratio of the observed count rates $r_{\alpha,\text{FM}}/r_{\alpha,\text{AG}}\,(i)$ as a function of the number of Si wafers (including the substrate wafer) behind the FM target is then:

$$r_{\alpha,\text{FM}}/r_{\alpha,\text{AG}}\,(i) = a\left(\frac{1+\frac{f(i)}{2}i\epsilon_{sca}}{1-i\,(\epsilon_{sca}+\epsilon_{abs})}\right) \tag{7.12}$$

To fit Eqn. (7.12), $f\,(i)$ is first fit to a 2nd-order polynomial, which allows for extrapolation to the 0-wafer case. The measured $r_{\alpha,\text{FM}}/r_{\alpha,\text{AG}}\,(i)$ and the fit to Eqn. (7.12) are shown in Fig. 7.12. From the fit $\epsilon_{sca} = (14.4 \pm 3.3) \times 10^{-6}$. The correction for the enhancement of the Flux Monitor signal due to the Si substrate is calculated by the ratio of Eqn. (7.10) for $i = 0/i = 1$: $r_{\alpha,FM}\,(i=0)\,/r_{\alpha,FM}\,(i=1)$. The uncertainty in a is excluded due to the form the correction takes which cancels the depenence in a. The multiplicative correction for the enhancement of the neutron signal due to the presence of the silicon substrate is then

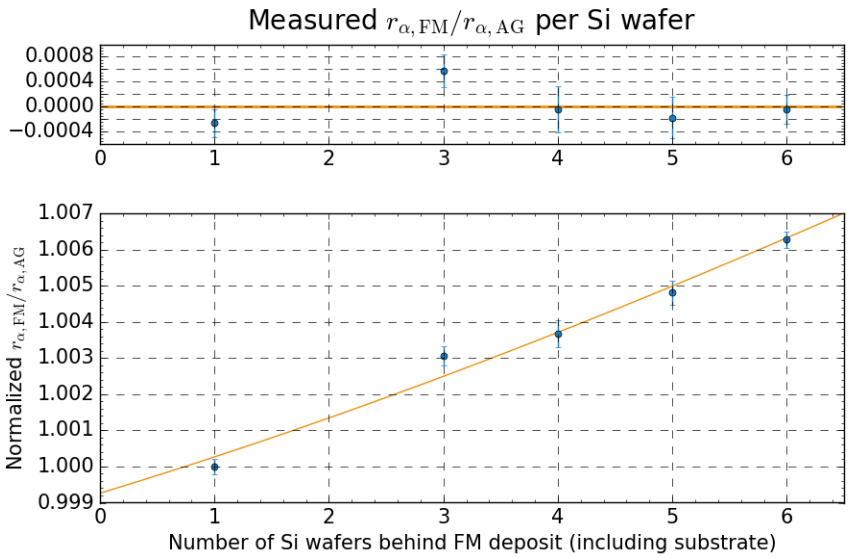

Figure 7.12: The measured FM alpha rate divided by the AG alpha rate for silicon wafers identical to the silicon substrate stacked behind the FM target. Data are normalized to the fractional rate with only the target substrate and no additional backings in the beam. The top graph shows the residuals. The fit line is to the known form of the equation. ϵ_{sca} and the fitting parameter a are allowed to vary. a divides out of the expressions for the corrections.

0.999953 ± 0.000011. The total neutron attenuation is $\epsilon_{sca} + \epsilon_{abs} = (9.54 \pm 0.03) \times 10^{-4}$ for a correction of 0.999045 ± 0.000003 to ϵ_{FM}.

7.5.3 Wavelength correction

The wavelength correction is fairly straightforward; in order to convert from the NG-6m wavelength $\lambda = 0.496$ nm ($v = 798$ m/s) to the thermal neutron standard wavelength $\lambda_0 = 1.798197$ nm ($v_0 = 2200$ m/s), the multiplicative correction is $\frac{\lambda_0}{\lambda} = 0.36246 \pm .00009$. Since the monochromatic beam energy is firmly in the $1/v$ region of neutron cross-sections, and the Flux Monitor efficiency ϵ_{FM} is linearly proportional to the cross-section (see Eqns. (2.14),

(2.15)), this amounts to the replacement of σ using the expression:

$$\begin{aligned} \sigma v &= \sigma_0 v_0 \\ \sigma v &\propto \sigma/\lambda \\ \sigma/\lambda &= \sigma_0/\lambda_0 \\ \sigma\tfrac{\lambda_0}{\lambda} &= \sigma_0 \end{aligned} \tag{7.13}$$

Such that the measured efficiency $\epsilon_{FM} \propto \sigma$ can be corrected to the ideal efficiency $\epsilon_0 \propto \sigma_0$ The wavelength of the monochromatic neutron beam as well as the fraction of $\lambda/2$ contamination are measured as described in Sec. 4.2. Neutrons with the shorter $\lambda/2$ wavelength are approximately half as likely to be detected in the Flux Monitor, but no less likely to be detected in the thick ^{10}B target. The quantity measured is the relative fraction of $\frac{\lambda/2}{\lambda}$ neutrons in the beam. The multiplicative correction is the factor which increases the measured Flux Monitor count rate r_{FM} to match what it would have been if there were no $\lambda/2$ component. Let r_0 be the desired "purely λ" FM count rate, and the correction c be the factor which converts $r_{FM} \rightarrow r_0$. Let the fraction of the full beam with wavelength λ and $\lambda/2$ be N_λ and N_{λ_2} respectively:

$$\begin{aligned} N_\lambda + N_{\lambda_2} &= 1 \\ r_0 &\propto \sigma\left(N_\lambda + N_{\lambda_2}\right) \\ r_{FM} &\propto \sigma\left(N_\lambda + \tfrac{1}{2}N_{\lambda_2}\right) \\ r_0 &= c \times r_{FM} \\ \left(1 + \tfrac{N_{\lambda_2}}{N_\lambda}\right) &= c\left(1 + \tfrac{1}{2}\tfrac{N_{\lambda_2}}{N_\lambda}\right) \\ c &= \frac{1+\frac{N_{\lambda_2}}{N_\lambda}}{1+\frac{1}{2}\frac{N_{\lambda_2}}{N_\lambda}} \end{aligned} \tag{7.14}$$

The high level of covariance between the numerator and denominator warrants use of the Poisson variance method discussed earlier in this chapter and in Chapter 6. The data points in all data sets are varied under Poisson statistics, and the correction recalculated

until it converges on a mean and standard deviation. The multiplicative correction to the measured ϵ_{FM} is $1.00039026 \pm 2.3 \times 10^{-7}$.

7.5.4 Flux Monitor Self-Shielding and Absorbed Neutrons

As the neutron beam passes through the Flux Monitor, ^{6}Li and Si absorb $\sim 1\%$ of the neutrons. To first order this is calculated from the areal density measured using neutron-induced charged particle counting and IDMS, the ENDF-VII cross section for thermal neutrons, and the measured neutron wavelength:

$$\phi_{abs} = 1 - e^{-\frac{N_A}{A}\rho(0,0)\sigma_0\frac{\lambda_{NG-6m}}{\lambda_0}} \tag{7.15}$$

The correction is target-dependent, and the interdependence with the self-shielding correction (below) requires special treatment. A nominal value of $1 - \phi_{abs} = 0.99261 \pm 0.00001$ is applied to the efficiency for ^{6}Li target 30-H3, and 0.99260 ± 0.00001 for 30-H5.

The absorption of an infinitely-thin deposit is slightly greater than that of an extended deposit. Rewriting Eqn. (7.15) in terms of the thickness $t\,(0,0)$ and volume density $\xi\,(0,0)$, Taylor expand and take the limit as $t \to 0$:

$$\lim_{t\to 0}\phi_{abs} = \phi_{ideal} = \lim_{t\to 0} 1 - \left(1 - \left(\frac{N_A}{A}t\,(0,0)\,\xi\,(0,0)\,\sigma_0\frac{\lambda_{NG-6m}}{\lambda_0}\right) + \frac{\left(\frac{N_A}{A}t(0,0)\xi(0,0)\sigma_0\frac{\lambda_{NG-6m}}{\lambda_0}\right)^2}{2!} - \ldots\right)$$

$$\phi_{ideal} \simeq +\frac{N_A}{A}t\,(0,0)\,\xi\,(0,0)\,\sigma_0\frac{\lambda_{NG-6m}}{\lambda_0} + \mathcal{O}\left(t^2\right)$$

and finally, recombining $t\,(0,0)$ and $\xi\,(0,0)$ into the areal density ρ,

$$\phi_{ideal} \simeq \frac{N_A}{A}\rho\,(0,0)\,\sigma_0\frac{\lambda_{NG-6m}}{\lambda_0} + \mathcal{O}\left(t^2\right) \tag{7.16}$$

The correction for an infinitely-thin deposit is then $\phi_{ideal}/\phi_{abs} = 1.003712$ and $1.003720 \pm$

0.000005 for the 30-H3 and 30-H5 targets respectively. Using the measured ϵ_0 and Eqn. (2.15), a value for $\rho(0,0)\sigma_0$ can be calculated which differs from the initial prediction used in the above expressions. Recalculating the corrections produces a new result for ϵ_0. Repeating the process rapidly produces convergent results for the absorbed fraction ϕ_{abs} and the self-shielding correction ϕ_{ideal}/ϕ_{abs}.

Table 7.9: Absorbed fraction correction

Target Deposit and Rig #	ϕ_{abs}
30-H3, Rig #2	0.99259 ±0.00001
30-H5, Rig #2	0.99260 ±0.00001

Table 7.10: Self-shielding correction.

Target Deposit and Rig #	ϕ_{ideal}/ϕ_{abs}
30-H3, Rig #2	1.003720 ±0.000005
30-H5, Rig #2	1.003722 ±0.000005

Chapter 8

Results and Conclusions

Through the course of this work we have calibrated the efficiency of two new Flux Monitor configurations for the NIST in-beam neutron lifetime experiment to high precision. These two new configurations will be used with the in-beam neutron lifetime experiment to test systematic effects associated with deposit thickness, small changes in solid angle subtended by the FM charged particle detectors for the beam spot center, and establish a baseline efficiency for testing possible changes in the Flux Monitor efficiency over the course of the experiment.

The improvements we have made to the Alpha-Gamma apparatus and Flux Monitor Mounting configurations enable data accumulation of FM Rig configurations in parallel with the in-beam neutron lifetime experiment. The original motivation for the manufacture of a large number of ^{10}B targets and the limited number of ^{6}Li targets was that the ^{10}B targets, which would have proportionally higher count rates due to the larger ^{10}B thermal neutron cross section, would serve as the primary in-beam neutron lifetime Flux Monitor targets. It was discovered that the areal density of ^{10}B experienced a slow decrease over time, and the targets were therefore deemed unusable. With systems in place to run the Alpha-Gamma experiment in parallel, the ^{10}B targets can be used in the in-beam neutron lifetime FM Rigs as long as they are book-ended with Alpha-Gamma calibrations. This is essentially the same way that the Alpha-Gamma HPGe detectors are kept in calibration in spite of the slow drift

in efficiency over time. This would allow higher neutron counting statistical accumulation with the same beam intensity and enable tests of possible systematics associated with the choice to use ^{6}Li in the Flux Monitor.

8.1 Results

Two Flux Monitor configurations were calibrated: 30-H5 using Rig #2 (Fig. 8.1), and 30-H3 using Rig #2(Fig. 8.2). Both configurations achieve the sub-0.1% goal of the experiment (see Table 8.1) and will be used in the in-beam neutron lifetime experiment currently taking place at the NCNR. Rig #1 was not available at the time. The fractional uncertainty associated with each calibration is dominated by the solid angle calibration of the Alpha-Gamma charged particle detector. An unfortunate failure of the Alpha-Gamma charged particle detector means that these data are limited by this uncertainty because replacement of the detector requires remeasurement of the solid angle.

Table 8.1: The efficiency ϵ_0 for both target configurations measured from 2014-2016

Configuration	ϵ_0
30-H5 Rig #2	(2.2649 ± 0.0021)E-5
30-H3 Rig #2	(2.2638 ± 0.0020)E-5

The efficiency for each triplet is calculated using the product of the measured detector rates as in Eqn (2.11) multiplied by the corrections determined in Chapter 7:

$$\epsilon_0 = \frac{r_{FM}}{r_\gamma(thick)} \frac{r_\gamma(thin)}{r_\alpha(thin)} \prod^{i} \Omega_i^{AG} \sqrt{c_i^T \times c_i^B} \tag{8.1}$$

where c_i^T and c_i^B are the corrections for the top and bottom HPGe detectors respectively. These are often the same value. The data are then fit to a constant. Covariances between the data emerge either due to the fact that a correction is applied to multiple data sets, or that data sets with different corrections are computing the same quantity. In order to

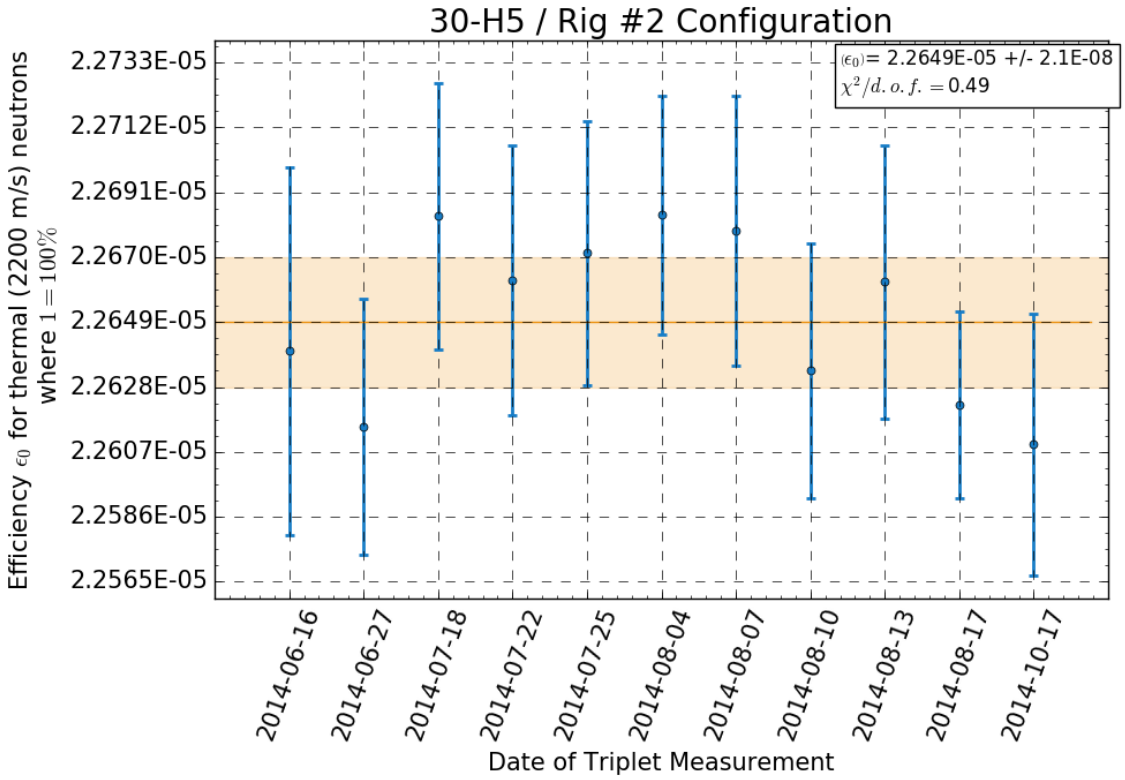

Figure 8.1: The measured Flux Monitor efficiency for 30-H5 in Rig #2 plotted against the date of each individual measurement.

encapsulate these covariances, each value entered into the calculation of ϵ_0, both from count rates during the triplets and from the corrections, is varied by its uncertainty under Poisson statistics and the efficiency recalculated. This is done many times. The standard deviation of these values is the standard deviation of ϵ_0 due to the uncertainty in the measurements. The relative uncertainties for each configuration are listed in Table 8.2.

The χ^2 per degree of freedom is consistently less than 1. This suggests that some of our uncertainties are overestimated. The most likely candidates will have error calculations which propagate through nonlinear functions. In some cases, conservative estimates were made for uncertainties which may also have been unnecessary.

Table 8.2: Systematic effects present in the measurement of the Flux Monitor efficiency ϵ_0 for each target configuration. The relative uncertainties are listed from largest to smallest.

Source of uncertainty (fractional)	30-H5 Rig #2	30-H3 Rig #2	Section
α-source Ω-calibration of AG α-detector	5.3×10^{-4}	5.3×10^{-4}	7.3.1
γ attenuation in thin ^{10}B target Si substrate	3.9×10^{-4}	3.9×10^{-4}	7.4.2
γ attenuation in B_4C (thick) target	2.4×10^{-4}	2.4×10^{-4}	7.4.3
Neutron beam wavelength	2.4×10^{-4}	2.4×10^{-4}	4.2.1
γ production in thin ^{10}B target Si substrate	8.1×10^{-5}	8.1×10^{-5}	7.4.1
Neutron absorption by ^{6}Li	6.9×10^{-5}	6.9×10^{-5}	7.5.4
Detector dead time	6.9×10^{-5}	6.9×10^{-5}	7.1
FM signal enh.: n backscatter in Si substrate	1.1×10^{-5}	1.1×10^{-5}	7.5.2
^{6}Li $\rho\,(x, y)$ diff. betw. I_{beam}& deposit center	1.0×10^{-5}	1.0×10^{-5}	7.5.1
AG α-detector beam spot to target center	9.1×10^{-6}	9.1×10^{-6}	7.3.1
Self-shielding of ^{6}Li deposit	5.3×10^{-6}	5.3×10^{-6}	7.5.4
FM solid angle beam spot to target center	3.8×10^{-6}	3.8×10^{-6}	7.5.1
Diff. in backscatter for ^{239}Pu α and ^{10}B α	3.8×10^{-6}	3.8×10^{-6}	7.3.2
Neutrons absorbed via ^{10}B(n,γ)^{11}B in B_4C	3.6×10^{-6}	3.6×10^{-6}	7.4.4
Neutron loss in FM Si substrate	3.3×10^{-6}	3.3×10^{-6}	7.5.2
FM misalignment w.r.t. beam	2.0×10^{-6}	2.0×10^{-6}	7.5.1
Neutron scattering from B_4C	3.4×10^{-7}	3.4×10^{-7}	7.4.4
$\lambda/2$ contamination of the beam	2.3×10^{-7}	2.3×10^{-7}	7.5.3
Neutron counting statistics	5.5×10^{-4}	4.5×10^{-4}	
Total	9.3×10^{-4}	8.7×10^{-4}	

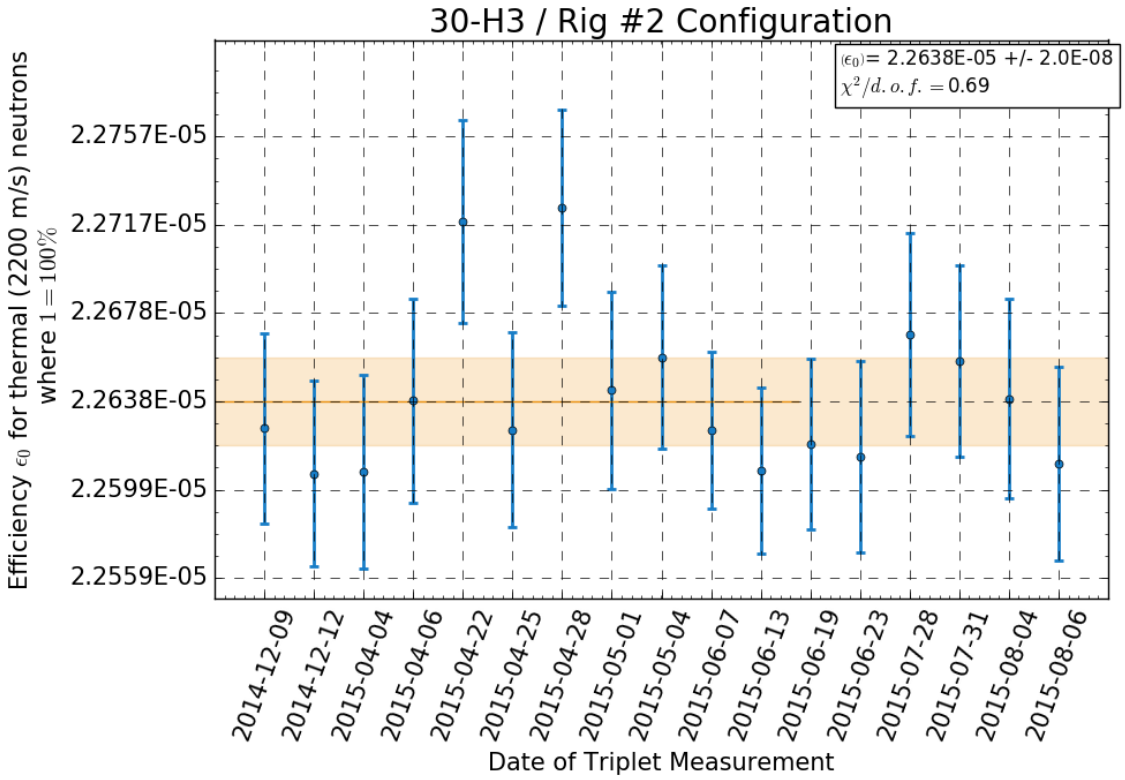

Figure 8.2: The measured Flux Monitor efficiency for 30-H3 in Rig #2 plotted against the date of each individual measurement.

8.2 Conclusions

The Alpha-Gamma experiment continues to exceed its design goals. We have provided two new Flux Monitor configurations for use with the in-beam neutron lifetime experiment and elsewhere. The efficiencies ϵ_0 associated with the Rig #2 30-H5 and 30-H3 configurations were $\epsilon_0^{\text{30-H5}}$ =2.2649×10^{-5} and $\epsilon_0^{\text{30-H53}}$ =2.2638×10^{-5} with relative uncertainties of 0.0093% and 0.0087% respectively. These additional Flux Monitors will help assess previously inaccessible systematics in the in-beam neutron lifetime experiment.

The largest source of uncertainty remained the measurement of the Alpha-Gamma solid angle using the ^{239}Pu source. Metrology has been performed to improve the uncertainty of the dimensions, but the available sources are very low activity. The remaining source

would require about 10 days each of solid angle stack counting and Alpha-Gamma counting to produce comparable statistics. Significant improvement could be achieved by producing new α sources of higher activity. The second largest source of uncertainty came from the measurement of 478 keV gamma attenuation in the thin target substrate. This direct measurement can only be improved by collecting more data. Now that the thick ^{10}B target metrology has been performed to higher precision than previously reported, the third largest source of uncertainty can also be reduced by continuing the attenuation measurement. Both of these will improve the uncertainty on previously reported data.

8.3 Alpha-Gamma Extensions

Absolute flux measurements using Alpha-Gamma or the calibrated Flux Monitor and NG-6m can be used to calibrate other neutron detectors and to measure neutron cross sections for isotopes of interest such as those used as nuclear physics standards. Recall Eqns. (2.14) and (2.11)

$$\epsilon_0 = \frac{2N_A\sigma_0}{4\pi A}\iint \Omega\left(x,y\right)\rho\left(x,y\right)\phi\left(x,y\right)dxdy$$

$$\epsilon = \frac{r_{FM}}{r_\gamma(thick)}\frac{r_\gamma(thin)}{r_\alpha(thin)}\Omega_{AG}$$

and replace σ_0 with σ to convert $\epsilon_0 \rightarrow \epsilon$, the neutron cross section at the NG-6m wavelength of $\lambda = 0.496$ nm for the material of interest. Instead of using Alpha-Gamma to solve for the Flux Monitor efficiency ϵ, set these equations equal and solve for the cross section σ, remembering to let (2.14) be written in terms of a fractional solid angle (the factor of $\frac{1}{4\pi}$ is dropped):

$$\sigma = \frac{r_{FM}}{r_\gamma(thick)}\frac{r_\gamma(thin)}{r_\alpha(thin)}\Omega_{AG}\frac{A}{2N_A}\frac{1}{\iint \Omega_{FM}\left(x,y\right)\rho\left(x,y\right)\phi\left(x,y\right)dxdy} \tag{8.2}$$

It is then a matter of producing a target deposit with a sufficiently well defined $\rho(x, y)$. This can be done for both the ^{6}Li and ^{10}B targets for which areal density characterization has been performed. The issues mentioned in Sec. 3.2 motivate further study of the ^{6}LiF targets by IDMS before moving forward with the cross section measurement. It is also a good opportunity to improve the neutron induced charged particle counting relationships between the ^{6}LiF targets.

Measurement of the ^{235}U(n, f) cross section at $\lambda = 0.496$ nm (3.3 meV) is an excellent test of the Alpha-Gamma technique. This cross section has been validated in countless experiments as well as through its use in the nuclear power industry. The challenge lies in the characterization of the target. One solution to this problem is to use a target which has a well controlled ^{234}U doping. Since the half life of ^{234}U is much shorter than ^{235}U, if the activity of the ^{234}U can be measured as a function of position on the target, the areal density of both isotopes can be determined. Fortunately, ^{234}U also has a much smaller (n, f) cross section, so the measurement of ^{235}U(n, f) is not greatly perturbed by its presence. The measurement of the ^{234}U activity would proceed just like other low solid angle measurements, except with a much smaller solid angle and with automated position control to produce good resolution. This would serve to measure both the profile and the density as a function of position.

A new diffractometer / reflectometer instrument at NCNR called CANDOR is under development which will use a polychromatic beam of neutrons and a set of collimators to perform rapid neutron reflectometry of samples. High spatial resolution ^{6}LiF doped zinc sulfide scintillating neutron detectors are necessary to realize this goal. One of the major challenges in constructing these detectors is balancing the ratios of ^{6}LiF, ZnS, and the binding agent. A bad ratio of compounds reduces the neutron detection efficiency. Bad mixing will also reduce the efficiency. The Flux Monitor has been used to calibrate a

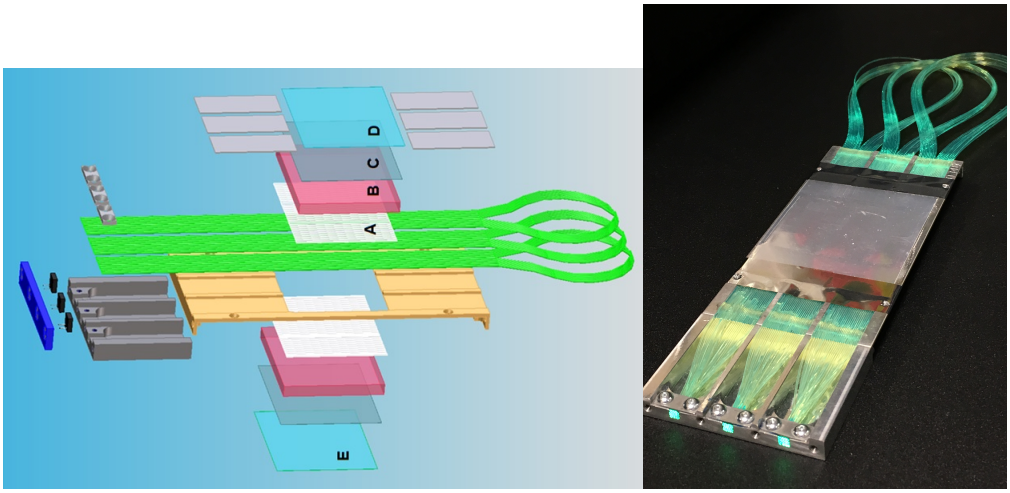

Figure 8.3: Left: a schematic of the CANDOR detectors exploded to show the layers. The green wavelength shifting fibers convert blue light to green light and guide them to solid state Si photomultiplier diodes. A: the scintillator primer. B: the bulk ^{6}LiF + ZnS scintillator. C: no longer used; formerly the reflector primer. D: polished aluminum reflector. E: plastic reflector. Right: a photograph of the CANDOR detectors.

prototype CANDOR ^{6}LiF doped zinc sulfide neutron detector yielding a neutron detection efficiency of $\epsilon_{CANDOR} = 89.5 \pm 1.4\%$, noting that an air gap of ~ 10 cm was present. Tighter collimation was necessary (C1 and C2 diameters were both 4mm) in order to reduce the beam spot size on the CANDOR detector so that the beam did not illuminate multiple detection regions. In order to reduce the number of corrections necessary, no target was present in the Alpha-Gamma apparatus. We also calibrated a ^{3}He tube for use in later CANDOR calibrations yielding $\epsilon_{^3He} = 90.5 \pm 1.2\%$. This was accomplished in 5 days, and was highly statistics-limited due to the tight collimation.

We are currently preparing to remeasure the absolute activity of the national standard neutron source NBS-1, a 1 Curie RaBe photoneutron source used as a calibration standard at NIST. NBS-1 was characterized over 50 years ago to an uncertainty of 1% [76]. Sources are measured against NBS-1 using a large manganese sulfate solution in water (the "Big Bath", Fig. 8.4) . The intense gamma radiation emitted from NBS-1 induces neutron production in beryllium. Neutrons moderate in the water and are captured on ^{55}Mn which

becomes the radioactive isotope ^{56}Mn with a 2.5789 hour half life. The activity in the bath is brought to saturation while the bath is sampled by a NaI detector far away from the intense gamma background. The count rate due to ^{56}Mn in the NaI detector is recorded during the rise in activity to saturation, during the saturated phase, and during the decay back to the background activity level. All three phases can be used to determine the neutron rate absorbed by the bath.

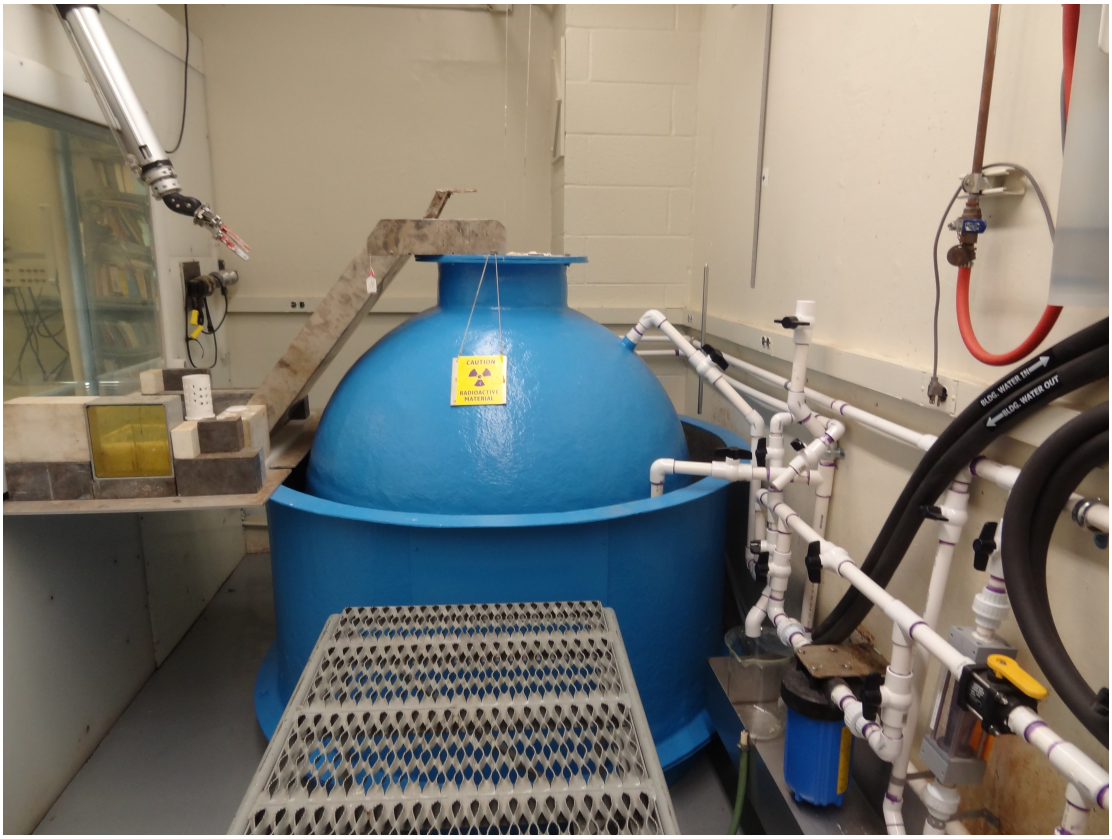

Figure 8.4: The manganese sulfate solution resides within the large blue sphere. The white piping samples the solution and carries it to NaI detector (outside the image). The arm on the left is necessary to manipulate NBS-1 safely.

A second $MnSO_4$ bath (the "Mini Bath") will be calibrated using an Alpha-Gamma calibrated Flux Monitor and the NG-6m neutron beam Fig. 8.5. NBS-1 does not fit inside of the Mini Bath. Instead a transfer source will be calibrated. BIPM-1 is a 0.5 Curie photoneutron source previously owned by the Bureau International des Poids et Mesures.

It is a good candidate because, in addition to fitting inside the Mini Bath, it produces a neutron field with similar characteristics to NBS-1. Since the backgrounds associated with the NCNR neutron guide hall may be different from those near the Big Bath, both the Mini Bath calibration and the measurement of BIPM-1 will take place in the guide hall.

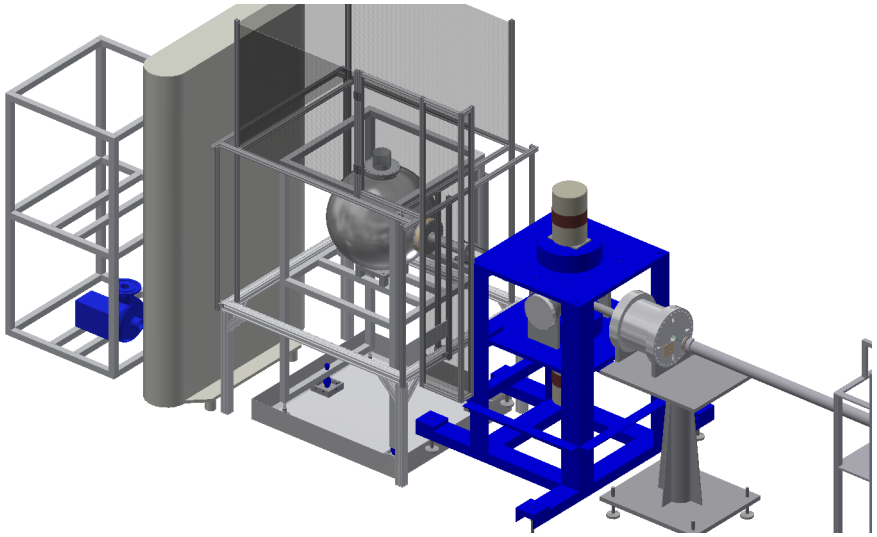

Figure 8.5: A schematic drawing of the Mini Bath on the NG-6m beamline. It is situated behind the Alpha-Gamma apparatus. The Flux Monitor is used to measure the absolute flux of neutrons during the measurement of the neutron detection efficiency of the Mini Bath.

Once BIPM-1 is calibrated, it will be used to remeasure the activity of NBS-1. This proceeds in exactly the same way that NBS-1 would be used to measure the activity of another source. We expect to achieve 0.25% absolute precision on the uncertainty.

Bibliography

[1] J. S. Nico, M. S. Dewey, D. M. Gilliam, F. E. Wietfeldt, X. Fei, W. M. Snow, G. L. Greene, J. Pauwels, R. Eykens, A. Lamberty, J. Van Gestel, and R. D. Scott, "Measurement of the neutron lifetime by counting trapped protons in a cold neutron beam," *Physical Review C - Nuclear Physics*, vol. 71, no. 5, p. 055502, 2005.

[2] N. Severijns, M. Beck, and O. Naviliat-Cuncic, "Tests of the standard electroweak model in nuclear beta decay," *Reviews of Modern Physics*, vol. 78, no. 3, pp. 991–1040, 2006.

[3] J. D. Bowman, L. J. Broussard, S. M. Clayton, M. S. Dewey, N. Fomin, K. B. Grammer, G. L. Greene, P. R. Huffman, A. T. Holley, G. L. Jones, C.-Y. Liu, M. Makela, M. P. Mendenhall, C. L. Morris, J. Mulholland, K. M. Nollett, R. W. Pattie, S. Penttil, and D. J. Salvat, "Determination of the free neutron lifetime," *arXiv:1410.5311v1*, pp. 2–9, 2014.

[4] A. T. Yue, M. S. Dewey, D. M. Gilliam, G. L. Greene, A. B. Laptev, J. S. Nico, W. M. Snow, and F. E. Wietfeldt, "Improved determination of the neutron lifetime," *Physical Review Letters*, vol. 111, no. 22, p. 222501, 2013.

[5] D. Dubbers and M. G. Schmidt, "The neutron and its role in cosmology and particle physics," *Reviews of Modern Physics*, vol. 83, pp. 1111–1171, oct 2011.

[6] F. E. Wietfeldt and G. L. Greene, "Colloquium: The neutron lifetime," *Reviews of Modern Physics*, vol. 83, no. 4, 2011.

[7] A. Serebrov, V. Varlamov, A. Kharitonov, A. Fomin, Y. Pokotilovski, P. Geltenbort, J. Butterworth, I. Krasnoschekova, M. Lasakov, R. Tal'daev, A. Vassiljev, and O. Zherebtsov, "Measurement of the neutron lifetime using a gravitational trap and a low-temperature Fomblin coating," *Physics Letters B*, vol. 605, no. 1-2, pp. 72–78, 2005.

[8] A. Pichlmaier, V. Varlamov, K. Schreckenbach, and P. Geltenbort, "Neutron lifetime measurement with the UCN trap-in-trap MAMBO II," *Physics Letters, Section B: Nuclear, Elementary Particle and High-Energy Physics*, vol. 693, no. 3, pp. 221–226, 2010.

[9] D. J. Salvat, E. R. Adamek, D. Barlow, J. D. Bowman, L. J. Broussard, N. B. Callahan, S. M. Clayton, C. Cude-Woods, S. Currie, E. B. Dees, W. Fox, P. Geltenbort, K. P. Hickerson, a. T. Holley, C.-Y. Liu, M. Makela, J. Medina, D. J. Morley, C. L. Morris, S. I. Penttilä, J. Ramsey, A. Saunders, S. J. Seestrom, E. I. Sharapov, S. K. L. Sjue, B. A. Slaughter, J. Vanderwerp, B. Vorndick, P. L. Walstrom, Z. Wang, T. L. Womack, and A. R. Young, "Storage of ultracold neutrons in the magneto-gravitational trap of the UCNτ experiment," *Physical Review C - Nuclear Physics*, vol. 89, no. 5, pp. 1–6, 2014.

[10] C. L. Morris, E. R. Adamek, L. J. Broussard, N. B. Callahan, S. M. Clayton, C. Cude-Woods, S. A. Currie, X. Ding, W. Fox, K. P. Hickerson, M. A. Hoffbauer, A. T. Holley, A. Komives, C.-Y. Liu, M. Makela, R. W. Pattie, J. Ramsey, D. J. Salvat, A. Saunders, S. J. Seestrom, E. I. Sharapov, S. K. Sjue, Z. Tang, J. Vanderwerp, B. Vogelaar, P. L. Walstrom, Z. Wang, W. Wei, J. W. Wexler, T. L. Womack, A. R. Young, and B. A.

Zeck, "A new method for measuring the neutron lifetime using an in situ neutron detector," *Review of Scientific Instruments*, vol. 88, no. 5, p. 053508, 2017.

[11] P. R. Huffman, C. R. Brome, J. S. Butterworth, K. J. Coakley, M. S. Dewey, S. N. Dzhosyuk, R. Golub, G. L. Greene, K. Habicht, S. K. Lamoreaux, C. E. Mattoni, D. N. McKinsey, F. E. Wietfeldt, and J. M. Doyle, "Magnetic trapping of neutrons," *Nature*, vol. 403, no. 6765, pp. 62–4, 2000.

[12] K. A. Olive *et al.*, "Review of Particle Physics," *Chin. Phys.*, vol. C38, p. 090001, 2014.

[13] A. Steyerl, J. M. Pendlebury, C. Kaufman, S. S. Malik, and A. M. Desai, "Quasielastic scattering in the interaction of ultracold neutrons with a liquid wall and application in a reanalysis of the Mambo I neutron-lifetime experiment," *Physical Review C*, vol. 85, no. 6, p. 065503, 2012.

[14] S. Arzumanov, L. Bondarenko, S. Chernyavsky, P. Geltenbort, V. Morozov, V. V. Nesvizhevsky, Y. Panin, and A. Strepetov, "A measurement of the neutron lifetime using the method of storage of ultracold neutrons and detection of inelastically up-scattered neutrons," *Physics Letters, Section B: Nuclear, Elementary Particle and High-Energy Physics*, vol. 745, pp. 79–89, 2015.

[15] V. V. Nesvizhevsky, A. P. Serebrov, R. Tal'daev, and A. Kharitonov, "Measurement of the neutron lifetime in a gravitational trap and analysis of experimental errors," *Journal of Experimental Theoretical Physics*, vol. 75, no. September, 1992.

[16] R. W. Pattie Jr., N. B. Callahan, E. R. Adamek, L. J. Broussard, S. M. Clayton, E. B. Dees, X. Ding, E. M. Engel, D. E. Fellers, W. Fox, K. P. Hickerson, M. A. Hoffbauer, A. Komives, S. W. T. Macdonald, M. Makela, C. L. Morris, J. D. Ortiz, J. Ramsey, A. Saunders, S. J. Seestrom, E. I. Sharapov, S. K. Sjue, Z. Tang, J. Vanderwerp, B. Vogelaar, Z. Wang, W. Wei, H. L. Weaver, J. W. Wexler, T. L. Womack, A. R. Young,

B. A. Zeck, L. Alamos, T. Universities, O. Ridge, O. Ridge, W. Point, M. Academy, and W. Point, "Measurement of the neutron lifetime using an asymmetric magneto - gravitational trap and in situ detection," in *eprint arxiv.org/abs/1707.01817*, 2017.

[17] E. Fermi, "Versuch einer Theorie der Beta-Strahlen," *Zeitschrift für Physik*, vol. 88, no. 3-4, pp. 161–177, 1934.

[18] G. Gamow and E. Teller, "Selection Rules for the β-Disintegration," *Physical Review*, vol. 49, no. 12, pp. 895–899, 1936.

[19] J. Jackson, S. Treiman, and H. Wyld, "Coulomb corrections in allowed beta transitions," *Nuclear Physics*, vol. 4, pp. 206–212, 1957.

[20] M. Kobayashi and T. Maskawa, "CP-Violation in the Renormalizable Theory of Weak Interaction\n," *Progress of Theoretical Physics*, vol. 49, no. 2, pp. 652–657, 1973.

[21] J. C. Hardy and I. S. Towner, "Superallowed $0^+ \rightarrow 0^+$ nuclear," *Physical Review C*, vol. 91, no. 2, pp. 1–27, 2015.

[22] W. J. Marciano and A. Sirlin, "Improved calculation of electroweak radiative corrections and the value of vud," *Physical Review Letters*, vol. 96, no. 3, pp. 1–4, 2006.

[23] J. C. Hardy and I. S. Towner, "CKM unitarity normalization tests, present and future," *Annalen der Physik*, vol. 525, no. 7, pp. 443–451, 2013.

[24] M. P. Mendenhall, R. W. Pattie, Y. Bagdasarova, D. B. Berguno, L. J. Broussard, R. Carr, S. Currie, X. Ding, B. W. Filippone, A. García, P. Geltenbort, K. P. Hickerson, J. Hoagland, A. T. Holley, R. Hong, T. M. Ito, A. Knecht, C.-Y. Liu, J. L. Liu, M. Makela, R. R. Mammei, J. W. Martin, D. Melconian, S. D. Moore, C. L. Morris, A. Pérez Galván, R. Picker, M. L. Pitt, B. Plaster, J. C. Ramsey, R. Rios, A. Saunders, S. J. Seestrom, E. I. Sharapov, W. E. Sondheim, E. Tatar, R. B. Vogelaar, B. Vorndick,

C. Wrede, A. R. Young, and B. A. Zeck, "Precision measurement of the neutron β-decay asymmetry," *Physical Review C - Nuclear Physics*, vol. 87, no. 3, pp. 5–10, 2013.

[25] D. Mund, B. M arkisch, M. Deissenroth, J. Krempel, M. Schumann, H. Abele, A. Petoukhov, and T. Soldner, "Determination of the weak axial vector coupling $\lambda = gA/gV$ from a measurement of the β-asymmetry parameter A in neutron beta decay," *Physical Review Letters*, vol. 110, no. 17, pp. 1–5, 2013.

[26] G. Darius, W. Byron, C. DeAngelis, M. Hassan, F. Wietfeldt, B. Collett, G. Jones, M. Dewey, M. Mendenhall, J. Nico, H. Park, A. Komives, and E. Stephenson, "Measurement of the Electron-Antineutrino Angular Correlation in Neutron β Decay," *Physical Review Letters*, vol. 119, no. 4, p. 042502, 2017.

[27] F. Iocco, G. Mangano, G. Miele, O. Pisanti, and P. D. Serpico, "Primordial nucleosynthesis: From precision cosmology to fundamental physics," *Physics Reports*, vol. 472, no. 1-6, pp. 1–76, 2009.

[28] R. H. Cyburt, B. D. Fields, K. A. Olive, and T. H. Yeh, "Big bang nucleosynthesis: Present status," *Reviews of Modern Physics*, vol. 88, no. 1, pp. 1–22, 2016.

[29] C. Patrignani and Particle Data Group, "Review of particle physics," *Chinese Physics C*, vol. 40, no. 10, p. 100001, 2016.

[30] C. H. Westcott, "The Specification of Neutron Flux and Nuclear Cross-Sections in Reactor Calculations," *J. Nuclear Energy*, vol. 2, pp. 59–75, 1955.

[31] A. Beer, "Bestimmung der Absorption des rothen Lichts in farbigen Flüssigkeiten," *Annalen der Physik und Chemie*, vol. 162, no. 5, pp. 78–88, 1852.

[32] C. J. Christensen, A. Nielsen, A. Bahnsen, W. K. Brown, and B. M. Rustad, "Free-neutron beta-decay half-life," *Physical Review D*, vol. 5, no. 7, pp. 1628–1640, 1972.

[33] A. Deruytter and P. Pelfer, "Precise determination of the branching ratio and Q-value of the ^{10}B(n, α)^{7}Li reaction and of the Q-value of the ^{6}Li(n, α)^{3}H reaction," *Journal of Nuclear Energy*, vol. 21, no. 11, pp. 833–845, 1967.

[34] M. L. Stelts, R. E. Chrien, M. Goldhaber, and M. J. Kenny, "Angular Distributions of the ^{6}Li(n, t)^{4}He and ^{10}B(n, a)^{7}Li reactions at 2 and 24 keV," *Physical Review C - Nuclear Physics*, vol. 19, no. 4, pp. 1159–1167, 1979.

[35] J. Kelley, E. Kwan, J. Purcell, C. Sheu, and H. Weller, "Energy levels of light nuclei A=11," *Nuclear Physics A*, vol. 880, pp. 88–195, 2012.

[36] M. B. Chadwick, M. Herman, P. Obložinský, M. E. Dunn, Y. Danon, A. C. Kahler, D. L. Smith, B. Pritychenko, G. Arbanas, R. Arcilla, R. Brewer, D. A. Brown, R. Capote, A. D. Carlson, Y. S. Cho, H. Derrien, K. Guber, G. M. Hale, S. Hoblit, S. Holloway, T. D. Johnson, T. Kawano, B. C. Kiedrowski, H. Kim, S. Kunieda, N. M. Larson, L. Leal, J. P. Lestone, R. C. Little, E. A. McCutchan, R. E. MacFarlane, M. MacInnes, C. M. Mattoon, R. D. McKnight, S. F. Mughabghab, G. P. A. Nobre, G. Palmiotti, A. Palumbo, M. T. Pigni, V. G. Pronyaev, R. O. Sayer, A. A. Sonzogni, N. C. Summers, P. Talou, I. J. Thompson, A. Trkov, R. L. Vogt, S. C. van der Marck, A. Wallner, M. C. White, D. Wiarda, and P. G. Young, "ENDF/B-VII.1 nuclear data for science and technology: Cross sections, covariances, fission product yields and decay data," *Nuclear Data Sheets*, vol. 112, no. 12, pp. 2887–2996, 2011.

[37] D. Tilley, C. Cheves, J. Godwin, G. Hale, H. Hofmann, J. Kelley, C. Sheu, and H. Weller, "Energy levels of light nuclei A=5, 6, 7," *Nuclear Physics A*, vol. 708, no. 1-2, pp. 3–163, 2002.

[38] J. Pauwels, R. D. Scott, R. Eykens, P. Robouch, J. Van Gestel, J. Verdonck, D. M. Gilliam, and G. L. Greene, "Improvements in the preparation and areal characterisation of ^{10}B and ^{6}LiF reference deposits," *Nuclear Instruments and Methods in Physics Research Section A: Accelerators, Spectrometers, Detectors and Associated Equipment*, vol. 362, no. 1, pp. 104–111, 1995.

[39] B. Denecke, R. Eykens, J. Pauwels, P. Robouch, D. M. Gilliam, P. Hodge, J. M. R. Hutchinson, and J. S. Nico, "Characterization of actinide targets by low solid-angle alpha particle counting," *Nuclear Instruments and Methods in Physics Research, Section A: Accelerators, Spectrometers, Detectors and Associated Equipment*, vol. 438, no. 1, pp. 124–130, 1999.

[40] J. Pauwels, R. Eykens, A. Lamberty, J. V. Gestel, H. Tagziria, R. D. Scott, J. Byrne, P. G. Dawber, and D. M. Gilliam, "The preparation and characterisation of ^{6}LiF and ^{10}B reference deposits for the measurement of the neutron lifetime," *Nuclear Instruments and Methods in Physics Research Section A: Accelerators, Spectrometers, Detectors and Associated Equipment*, vol. 303, pp. 133–140, 1991.

[41] R. D. Scott, J. Pauwels, R. Eykens, and D. M. Gilliam, "The characterisation of ^{10}B and ^{6}LiF reference deposits by the measurement of neutron induced charged particle reactions," *Nuclear Instruments and Methods in Physics Research Section A: Accelerators, Spectrometers, Detectors and Associated Equipment*, vol. 314, pp. 163–170, 1992.

[42] R. D. Scott, P. D'hondt, R. Eykens, P. Robouch, D. Reher, G. Sibbens, J. Pauwels, and D. M. Gilliam, "The characterization of ^{10}B and ^{6}LiF reference deposits by measurement of neutron-induced charged particle reactions — a second campaign," *Nuclear*

Instruments and Methods in Physics Research Section A: Accelerators, Spectrometers, Detectors and Associated Equipment, vol. 362, no. 1, pp. 151–159, 1995.

[43] P. De Bièvre and G. Debus, "Precision mass spectrometric isotope dilution analysis," *Nuclear Instruments and Methods*, vol. 32, no. 2, pp. 224–228, 1965.

[44] A. Lamberty and P. De Bièvre, "Isotope dilution mass spectrometry of ^{10}B and ^{6}LiF reference deposits used for the determination of the neutron lifetime," *International Journal of Mass Spectrometry and Ion Processes*, vol. 108, no. 2-3, pp. 189–198, 1991.

[45] H. Qi, P. Taylor, M. Berglund, and P. De Bièvre, "Calibrated measurements of the isotopic composition and atomic weight of the natural Li isotopic reference material IRMM-016," *International Journal of Mass Spectrometry and Ion Processes*, vol. 171, no. 1-3, pp. 263–268, 1997.

[46] A. Lamberty, A. Verbruggen, F. Hendrickx, and P. De Bièvre, "A CBNM ^{6}Li spike isotopic reference material CBNM-IRM-615," *International Journal of Mass Spectrometry and Ion Processes*, vol. 113, no. 3, pp. 223–232, 1992.

[47] E. Michiels and P. De Bièvre, "Absolute isotopic composition and the atomic weight of a natural sample of lithium," 1983.

[48] G. Flesch, A. Anderson, and H. Svec, "A secondary isotopic standard for ^{6}Li/^{7}Li determinations," *International Journal of Mass Spectrometry and Ion Physics*, vol. 12, no. 3, pp. 265–272, 1973.

[49] H. P. Qi, M. Berglund, P. D. P. Taylor, F. Hendrickx, A. Verbruggen, and P. De Bièvre, "Preparation and characterisation of synthetic mixtures of lithium isotopes," *Fresenius Journal Of Analytical Chemistry*, vol. 361, no. 8, pp. 767–773, 1998.

[50] S. Duta, M. Berglund, and P. Taylor, "Updated certified values of the lithium isotopic reference materials IRMM-016, IRMM-015 and IRMM-615," *Rapid Communications in Mass Spectrometry*, vol. 23, pp. 937–938, mar 2009.

[51] A. T. Yue, *Progress Toward a Redetermination of the Neutron Lifetime Through the Absolute Determination of Neutron Flux*. PhD thesis, University of Tennessee, Knoxville, 2011.

[52] W. R. Leo, *Techniques for Nuclear and Particle Physics Experiments: A How-to Approach*. Germany: Springer-Verlag, 1 ed., 1987.

[53] A. K. Freund, "Cross-sections of materials used as neutron monochromators and filters," *Nuclear Instruments and Methods In Physics Research*, vol. 213, no. 2-3, pp. 495–501, 1983.

[54] J. Richardson, *Accurate Determination of Thermal Neutron Flux: A Critical Step in the Measurement of the Neutron Lifetime*. Phd thesis, Harvard University, 1993.

[55] R. Graziani and P. Veronese, "How to Compute a Mean? The Chisini Approach and Its Applications," *The American Statistician*, vol. 63, no. 1, pp. 33–36, 2009.

[56] A. Lann and R. Falk, "Tell Me the Method, I'll Give You the Mean," *The American Statistician*, vol. 60, no. 4, pp. 322–327, 2006.

[57] L. Costrell and H. Meyer, "CAMAC - system design made easy," *NatureNature*, vol. 275, pp. 781–782, 1978.

[58] C. Michotte and M. Nonis, "Experimental comparison of different dead-time correction techniques in single-channel counting experiments," *Nuclear Instruments and Methods in Physics Research, Section A: Accelerators, Spectrometers, Detectors and Associated Equipment*, vol. 608, no. 1, pp. 163–168, 2009.

[59] D. M. Gilliam, A. T. Yue, and M. S. Dewey, "The use of polyimide foils to prevent contamination from self-sputtering of ^{252}Cf deposits in high-accuracy fission counting," *Nuclear Instruments and Methods in Physics Research, Section A: Accelerators, Spectrometers, Detectors and Associated Equipment*, vol. 590, no. 1-3, pp. 181–184, 2008.

[60] W. H. Bragg and R. Kleeman, "XXXIX. On the α particles of radium, and their loss of range in passing through various atoms and molecules," *Philosophical Magazine Series 6*, vol. 10, no. 57, pp. 318–340, 1905.

[61] W. H. Bragg, "On the Ionization of Various Gases by the Particles of Radium," *Proceedings of the Physical Society of London*, vol. 20, no. 1, pp. 523–550, 1906.

[62] A. Brown and H. Suit, "The centenary of the discovery of the Bragg peak," *Radiotherapy and Oncology*, vol. 73, no. 3, pp. 265–268, 2004.

[63] E. Browne and J. K. Tuli, "Nuclear Data Sheets for A = 236," *Nuclear Data Sheets*, vol. 107, no. 10, pp. 2649–2714, 2006.

[64] P. C. Johns and M. J. Yaffe, "Correction of pulse-height spectra for peak pileup effects using periodic and random pulse generators," *Nuclear Instruments and Methods in Physics Research Section A: Accelerators, Spectrometers, Detectors and Associated Equipment*, vol. 255, no. 3, pp. 559–581, 1987.

[65] E. Rutherford, "The scattering of α and β particles by matter and the structure of the atom," *Philosophical Magazine Series 6*, vol. 21, pp. 669–688, 1911.

[66] A. K. Jain, A. Ghosh, and B. Singh, "Nuclear Data Sheets for A = 165," *Nuclear Data Sheets*, vol. 107, no. 5, pp. 1075–1346, 2006.

[67] J. F. Ziegler, M. D. Ziegler, and J. P. Biersack, "SRIM - The stopping and range of ions in matter (2010)," *Nuclear Instruments and Methods in Physics Research B*, vol. 268, pp. 1818–1823, June 2010.

[68] M. A. Lone, D. C. Santry, and W. M. Inglis, "MeV Nuetron Production from Thermal Neutron Capture in Li and B Compounds.," *Nuclear instruments and methods*, vol. 174, no. 3, pp. 521–529, 1980.

[69] R. Bevilacqua, F.-J. Hambsch, R. Bencardino, G. Giorginis, M. Vidali, L. Lamia, and I. Ruskov, "10B and 6Li Nuclear Data Measurements for Incident Neutron Energies up to 3 MeV," *Nuclear Data Sheets*, vol. 119, pp. 104–106, 2014.

[70] M. Shamsuzzoha Basunia, "Nuclear Data Sheets for A = 29," *Nuclear Data Sheets*, vol. 113, no. 4, pp. 909–972, 2012.

[71] M. J. Berger, J. H. Hubbell, S. M. Seltzer, J. Chang, J. S. Coursey, R. Sukumar, D. S. Zucker, and K. Olsen, "Xcom: Photon cross section database (version 1.5)," 2010.

[72] P. J. J. Kok, J. B. M. de Haas, K. Abrahams, H. POstma, and W. J. Huiskamp, "Investigation of Excited States of ^{11}B and ^{7}Li by Means of Thermal Neutron Capture of ^{10} B Nuclei," *Z. Phys. A*, vol. 324, p. 271, 1986.

[73] R. B. Firestone and Z. Revay, "Thermal neutron radiative cross sections for ^{6,7}Li, ^{9}Be, ^{10,11}B, ^{12,13}C, and ^{14,15}N," *Physical Review C*, vol. 93, no. 5, p. 054306, 2016.

[74] G. A. Bartholomew and P. J. Campion, "Neutron capture gamma rays from lithium, boron, and nitrogen," *Canadian Journal of Physics*, vol. 35, no. 12, pp. 1347–1360, 1957.

[75] V. Mclane, M. Kellett, O. Schwerer, and S. Maev, "Nuclear Reaction Data Center Network: Past, Present, and Future," *Journal of Nuclear Science and Technology*, vol. 39, no. sup2, pp. 1458–1463, 2002.

[76] R. Noyce, E. Mosburg, S. Garfinkel, and R. Caswell, "Absolute calibration of the national bureau of standards photoneutron source - iii. absorption in a heavy water solution of manganous sulphate," *Journal of Nuclear Energy. Parts A/B. Reactor Science and Technology*, vol. 17, no. 7, pp. 313 – 319, 1963.

Eamon Anderson | Indiana University

Curriculum Vitae August 14, 2017

Profile

My research interests have focused on precision measurement of absolute quantities and measurements of fundamental physics using neutrons. I will continue to build on my experience with neutron measurement, especially as it pertains to absolute measurements of quantities of interest to the physics and engineering communities, such as neutron cross sections, and neutron imaging and analysis of manufactured and biological materials. My accomplishments include the design of a cryogenic bellows-style liquid helium pump and the development of experiments to measure absolutely the ^{235}U fission cross section and the ^{6}Li total cross section, as well as an experiment to remeasure the absolute activity of the national standard neutron source NBS-1, which is maintained at the National Institute of Standards and Technology (NIST).

Education

2005-May 2009	B.A., Physics, Grinnell College, Grinnell IA
2009-August 2017	PhD, Nuclear Physics, Indiana University, Bloomington IN
	2013-2017: Research Assistant, National Institute of Standards and Technology, Gaithersburg MD
	2009-2013: Research Assistant, IU Physics Department, Bloomington IN
	2009-2010: Teaching Assistant, IU Physics Department, Bloomington IN

Skills and Experience

Precision measurement	principles of absolute measurement of physical systems (neutrons, metrology)
	neutron wavelength measurement using Laue diffraction
	neutron standards calibration (radiological sources, cross-sections, etc.)
Other experimental	neutron-induced fission measurements
	cryogenic pump design
Electronics	low-noise analog systems
Programming and computational	Python 3.X
	AutoCAD (Autodesk Inventor) proficiency
Writing	Bi-annual progress reporting for federal funding agencies
Teaching	Introductory physics lab for non-majors

Publications and Proceedings

Refereed Journal Articles:

1. W. M. Snow, E. Anderson, L. Barron-Palos, C. D. Bass, T. D. Bass, B. E. Crawford, C. Crawford, J. M. Dawkins, D. Esposito, J. Fry, H. Gardiner, K. F. Gan, C. Haddock,

B. R. Heckel, A. T. Holley, J. C. Horton, C. Huffer, J. Lieffers, D. Luo, M. Maldonado-Velazquez, D. M. Markoff, A. M. Micherdzinska, H. P. Mumm, J. S. Nico, M. Sarsour, S. Santra, E. I. Sharapov, H. E. Swanson, S. B. Walbridge, and V. Zhumabekova, **A slow neutron polarimeter for the measurement of parity-odd neutron rotary power**, Rev. Sci. Inst. **86**, 055101 (2015). [Link]

2. W. M. Snow, E. Anderson, L. Barrón-Palos, C. D. Bass, T. D. Bass, B. E. Crawford, J. Fry, K. Gan, B. R. Heckel, D. Luo, R. C. Malone, D. M. Markoff, A. M. Micherdzinska, H. P. Mumm, J. S. Nico, A. K. Opper, S. Penn, S. Santra, M. Sarsour, E. I. Sharapov, H. E. Swanson, S. Van Sciver, S. B. Walbridge, V. Zhumabekova, **Parity violating neutron spin rotation in ^{4}He and H**, Il Nuovo Cimento C **35** 04, 57-62 (2012). [Link]

Published Proceedings:

3. W. M. Snow, E. Anderson, L. Barron Palos, C. D. Bass, B. E. Crawford, C. Crawford, D. Esposito, W. Fox, J. Fry, H. Gardiner, C. Haddock, B. R. Heckel, A. T. Holley, J. Lieffers, M. Maldonado-Velazquez, R. Malone, D. Markoff, H. P. Mumm, J. S. Nico, D. Olek, C. Paudel, S. Penn, P. C. Rout, S. Santra, M. G. Sarsour, A. Sprow, H. E. Swanson, J. Vanderwerp, and S. van Sciver, **Searches for Possible Exotic Spin-Dependent Interactions of Slow Neutrons with Matter using Neutron Spin Rotation**, Journal of the Physical Society of Japan Conference Proceedings **8**, 062003 (2015). [Link]

In-Preparation Journal Articles:

4. E.S. Anderson, D.S. Hussey, H. Miao, G. Yuan, D.A. Pushin, D. Sarenac, M.G. Huber, D.L. Jacobson, J.M. LaManna, W.M. Snow, and H. Wen **Demonstration of a monochromatic far-field neutron interferometer for microstructural analysis**, for J. Appl. Phys.

5. C. Haddock, E. Anderson, W. M. Snow, *et. al.* (NSR Collaboration), **A New Upper Bound on Spin-dependent Interactions of the Neutron from Light Spin 1 Boson Exchange from Neutron Spin Rotation**, for Phys Rev. D (2017).

6. A. T. Yue, E. S. Anderson, M. S. Dewey, D. M. Gilliam, G. L. Greene, A. B. Laptv, J. S. Nico, **Absolute neutron rate measurement of a monochromatic neutron beam**

7. A. T. Yue, E. S. Anderson, M. S. Dewey, D. M. Gilliam, G. L. Greene, A. B. Laptv, J. S. Nico, **Direct measurement of the ^{6}Li(n,t)^{4}He cross section at $E_n = 3.3$ meV**

8. D.S. Hussey, E. Anderson, H. Miao, J.M. LaManna, D.L. Jacobson, L. Anovitz, H. Wen, **Multi-scale imaging of 3D microstructure of Westerly granite specimen**

Invited Talks:

9. "Absolute neutron flux with Alpha-Gamma: the neutron lifetime and further applications," Nuclear Physics Seminar at University of Tennessee (Knoxville TN, USA, Sept. 12, 2016)

10. "A primer on mean values: what we do right, wrong, and how to calculate the one you want," NIST Neutron Phys. Group Seminar (Gaithersburg MD, March 3, 2015)

Contributed Talks:

11. E. Anderson for the Alpha-Gamma collaboration, "Precision neutron flux measurements and applications using the Alpha Gamma device", APS April Meeting (Salt Lake City, Utah 2016) [Link]

12. E. Anderson for the Alpha-Gamma collaboration, "Precision neutron flux measurements and applications using the Alpha Gamma device", APS April Meeting (Baltimore, Maryland 2015) [Link]

13. E. Anderson for the Neutron Spin Rotation collaboration, "Probing the Hadronic Weak Interaction using Polarized Slow Neutron Spin Rotation in L4He", APS April Meeting (Savannah, Georgia 2014), [Link]

14. E. Anderson for the Neutron Spin Rotation collaboration, "Apparatus Improvements for the Neutron Spin Rotation Device", APS DNP Fall Meeting (Newport News, Virginia 2013) [Link]

Research

My focus as a graduate student has been fundamental physics using neutrons. Since 2009, I have mainly been working under W. Mike Snow at Indiana University on three projects.

Graduate Student, 2009-present:
Alpha-Gamma (2013-present, NIST Center for Neutron Research (NCNR)), with Andrew Yue, Scott Dewey, David Gilliam and Pieter Mumm:

The **Alpha-Gamma experiment**, operating on NCNR neutron beamline NG6m, is the first experiment designed to measure the absolute neutron fluence rate in a monochromatic neutron beam to **sub-.1% precision** independent of quantities such as neutron cross-sections. I have used this apparatus to calibrate the absolute efficiency of the ^{6}Li fluence rate monitor for the upcoming NIST in-beam Neutron Beam Lifetime experiment (BL2) which will start to take neutron data in Fall 2016. Neutrons incident on a thick enriched $^{10}B_4C$ target emit 478 keV photons with 93.7% probability, which are counted in a pair of HPGe gamma detectors. The efficiency of the gamma detectors is determined using a cross-calibration procedure which is ultimately tied to careful metrology of the absolute activity of a ^{239}Pu alpha source. The energy of the neutron beam is measured using diffraction from a perfect silicon crystal.

I have been **responsible for primary data taking and analysis** on this experiment since 2014. I have updated and improved the apparatus and analysis code, and have measured additional systematic effects which will be needed to justify our ultimate claims for the absolute accuracy of the technique. While writing a new set of analysis procedures in the Python 3.5 coding language, I discovered and corrected subtle inconsistencies in the calculation of the detector counting ratios which are used for the cross-calibration procedure.

The Alpha-Gamma apparatus can be used with any source with neutron energies corresponding to the "1/v" region of the detection material's neutron cross section. I have collaborated with my NIST colleagues to expand the scope of the Alpha-Gamma experiment to include direct measurements of neutron cross-sections of nuclei such as ^{6}Li and ^{235}U, which are widely used in other neutron fluence rate detectors, as well as isotopes with

poorly-measured cross-sections such as ^{175}Lu and ^{176}Lu. Absolute neutron cross-sections are needed in various areas of defense, nuclear energy and industry as standards for nuclear reactions, moderation, neutron detection, or neutron analysis (such as SANS or neutron imaging) of devices which employ these materials. Cross-sections of lutetium isotopes are interesting to investigations of stellar nucleosynthesis and planetary genesis.

I have also aided with the ongoing recalibration of the national standard neutron source NBS-1. NIST serves the United States nuclear research and industrial community by measuring the absolute activity of neutron sources from vendors using a 4π neutron detection apparatus called the Manganese Bath. NBS-1, a Ra-Be photo-neutron source, calibrates this system prior to a measurement, but, due in part to the current uncertainties on the absolute activity of NBS-1, the technique is limited to a typical relative uncertainty of $\sim 2.5\%$. Measurement of NBS-1 using a transfer calibration procedure similar to that employed in the Alpha-Gamma experiment itself will enable an absolute measurement with significantly improved uncertainty.

For the NBS-1 measurement, I have worked primarily on the incorporation of a smaller Mn bath (called the 'Minibath') for use with Alpha-Gamma. In this case, the previously-calibrated fluence monitor for BL2 will perform the absolute neutron fluence measurement for calibration of the Minibath. Many of the systematic measurements relevant to Alpha-Gamma are applicable to this measurement as well.

My results for the absolute efficiencies of the neutron lifetime beam monitors will be presented in my PhD thesis and included as an essential component of the eventual scientific paper for the neutron lifetime measurement. An Alpha-Gamma apparatus paper and a ^{6}Li cross-section measurement paper are currently under revision for publication.

NIST in-beam Neutron Lifetime Experiment (BL2), (2013-present, NIST Center for Neutron Research (NCNR)), with Jeff Nico, Scott Dewey, Andrew Yue, Jonathan Mulholland, Kyle Grammar, Christina DeAngelis and off-site collaborators:

The NIST neutron lifetime effort, BL2, serves as the only in-beam neutron lifetime experiment informing the accepted value of 880.3 $\pm$1.1 s. The free neutron beta decay is the most fundamental form of the nuclear weak interaction and contributes to our understanding of Big Bang nucleosynthesis and CKM unitarity. In the BL2 experiment, a beam of neutrons passes through a pseudo-penning trap defining a fiducial proton trapping volume. When a neutron decays, the decay proton is counted. Based on the neutron fluence rate and dimensions of the volume, the neutron lifetime can be determined.

My primary contribution to this experiment was the completion of the Alpha-Gamma experiment and measurement of the absolute efficiency of the neutron fluence rate monitor. I **designed and built the proton detector translation stage** for semi-automated mapping of the proton detection region. Since the proton detector is held at 30 kV, it is time-consuming to perform a small translation in the position of the detector. This is necessary for systematic effect measurement, so accelerating this process is important for beam time optimization. I also participated in investigations of detector failure via voltage breakdown by characterizing surface defects and debris using a metrology microscope.

Neutron Spin Rotation (2009-2013, Center for Exploration of Energy and Matter (CEEM, formerly Indiana University Cyclotron Facility, or IUCF)), with Mike Snow, Jason Fry, Walt Fox (mechanical engineer), John Vanderwerp, and off-site collaborators (including Jeff Nico):

Neutron Spin Rotation (NSR) is designed to **measure the vector-axial weak coupling of the long-range weak interaction** in polarized neutrons using liquid helium. Vertically-polarized neutrons pass through a ~ 80 cm volume of liquid helium (LHe) and the rotation angle is analyzed upon exit. Rotation results from the difference in optical potential for forward- and backward-polarized neutrons with respect to the direction of motion. The expected size of the rotation angle is a fraction of a microradian. The measurement suppresses parity-conserving effects via careful design of the apparatus.

My primary contribution to the experiment was to **enable faster mobility of liquid helium by designing a bellows-style pump** to replace the centrifugal pump used in the previous experiment. Part of the parity-conserving cancellation is achieved by dividing the LHe chamber in to four quadrants and filling the 1^{st} and 3^{rd}, then emptying those and filling the 2^{nd} and 4^{th}. Neutron source fluctuations mean that the experiment is sensitive to the speed with which the transfer can take place. That speed therefore also limits the total volume that can be used. I designed, built, and tested a pump using edge-welded bellows in water and liquid nitrogen. This work informed the final design of the pump, which is now under construction using titanium bellows. This will result in a reduced fill time by a factor of 5 in the ultimate experiment.

I also commissioned and maintained components of the experimental apparatus, including the construction of new μ-metal magnetic shielding, tests of a new LHe reliquification system, and analysis of the electronic noise of the current-mode neutron detector. This apparatus is now in operation at the LANSCE neutron source at Lost Alamos, where it will be used in an experiment in Fall 2016 to search for possible exotic spin-dependent interactions of the neutrons with matter. This work is described in the scientific papers cited in my CV.